# Multidimensional MOF Mixed Matrix Membranes for Efficient Gas Separation

by

**Hyunhee Lee**

Submitted to the Department of Chemical Engineering
in partial fulfillment of the requirements for the degree of

Doctor of Philosophy

at the

MASSACHUSETTS INSTITUTE OF TECHNOLOGY

September 2023



Author .....
Hyunhee Lee
Department of Chemical Engineering
August 7, 2023

Certified by .....
Zachary P. Smith, Ph.D.
Joseph R. Mares Career Development Professor of Chemical Engineering
Thesis Supervisor

Accepted by .....
Patrick S. Doyle
Robert T. Haslam Professor of Chemical Engineering
Graduate Officer

# Multidimensional MOF Mixed Matrix Membranes for Efficient Gas Separation

by

Hyunhee Lee

Submitted to the Department of Chemical Engineering
on August 7, 2023, in partial fulfillment of the
requirements for the degree of
Doctor of Philosophy

## Abstract

Membrane separations are crucial in the chemical industry, with polymeric materials traditionally used due to their cost and mechanical benefits. However, they face challenges in permeability–selectivity trade-off, and in stability. Metal–organic frameworks (MOFs) offer potential solutions with their customizable properties but are difficult to manufacture. Mixed-matrix membranes (MMMs), which incorporate MOFs into polymers, mitigate some issues, yet high MOF loading can lead to aggregation and voids. This thesis investigates the promising potential of MMMs for efficient and improved gas separation, leveraging unique morphologies and understanding the dynamics of MOF–polymer interactions. First, the novel branch-shaped ZIF-8 (BZ) was developed and incorporated into polymer matrix, which successfully established a percolated network at loadings as low as 20 wt%, showing permeability boost. Also, it showed suppressed polymer chain dynamics and a smaller diffusion cut-off than traditional ZIF-8, which resulted in an enhanced membrane stability and superior performance in $H_2$-based separations. BZ was studied further by investigating temperature-dependent properties of MMMs. BZ and control ZIF-8 (CZ) MMMs exhibited unique gas transport behaviour in relation to temperature shifts, with BZ MMM demonstrating more significant temperature dependence for $H_2$-based separations. As temperature decreases, the $H_2/CH_4$ permselectivity of BZ MMMs drastically increases, with minor changes in $H_2$ permeability. Conversely, at higher temperatures, separation performance aligns with that of CZ MMM, showing continuous yet broad control over the gas performance. To understand the origin of this selectivity difference, facet-specific gas transport in polymer nanocomposites was studied with the hypothesis of BZ consist of facet 100, which characterize less thermally stable polymorph, cubes. A key finding is the interaction between 100 facet and polyimides, which enhances hydrogen-based and ethylene/ethane separation, particularly at subambient temperatures, which is consistent with the trend observed for BZ MMMs. In conclusion, this thesis addresses the enhancement of MMMs through innovative morphological approaches, where percolated network enhances permeability and 100 facet termination may restrict the MOF–polymer interphase confinement,

leading to high selectivity for small gas pairs, which is very difficult to achieve at the same time. The temperature effects and facet-termination effects on gas transport in MMMs can also offer substantial contributions to the development and optimization of mixed matrix membranes for efficient gas separations.

Thesis Supervisor: Zachary P. Smith, Ph.D.
Title: Joseph R. Mares Career Development Professor of Chemical Engineering

# Acknowledgments

Reflecting on my Ph.D. journey at MIT, I recognize the myriad of experiences and friendships that have enriched this transformative period of my life, which has felt both fleeting and eternal at times.

Firstly, my deepest gratitude goes to my advisor, Prof. Zachary Smith. Your steadfast support in the Smith lab was invaluable. Your genuine concern for my well-being, in and outside the lab, and your guidance made my research endeavors fruitful. Your patience and guidance during every challenging phase were instrumental. I couldn't have wished for a better mentor.

I'm equally indebted to my thesis committee - Professor Michael Strano and Professor Mircea Dincă. Their incisive questions, feedback, and unwavering support throughout our meetings have greatly contributed to my academic progression.

A special shoutout to my lab mates - past and present: Albert, Qihui, Sharon, Lucas, Francesco, Katherine, Patrick, Andy, TJ, Moonjoo, Justin, Fatimah, Shaofei, Kayla, Aristotle, Wan-Ni, Jing Ying, Pablo, Simar, Phillippe, Sam, Taehoon, and Erin. The camaraderie in the lab was uplifting, making even the challenging days bearable. Our shared outings - from bowling to hot pot nights - remain etched in my memory. A note for newer members: I wish we had more time together. TJ, your presence was akin to a safety net, even though our projects weren't shared. Jing Ying, you've been an anchor throughout. Justin and Moonjoo, as postdocs, your support was unparalleled. To the Inorganic Subgroup, Small Office, Better-Me-Group, and my internal collaborators - the laughs, challenges, and successes we shared will always be treasured.

Within the department, my bond with the '9-hour per week group' was a lifeline, especially during the intense first year. Practice school comrades made our time in Houston, Dubai, and notably Budapest, memorable. A hearty cheer to the Korean ChemE community for their unwavering companionship.

Outside academia, the west coast swing community was a sanctuary, letting me dance away lab stresses and enjoy the company of wonderful people.

My dearest friend, Seoyoung Min, your support over the past 15 years has been a beacon of hope. Our shared memories are treasures I cherish.

To my family, your unwavering support and invaluable life lessons fueled my perseverance. The foundation you provided has been my strength.

Lastly, to my beloved husband, Soon: our shared journey through the highs and lows of grad school has only strengthened our bond. Your consistent encouragement, culinary treats, and shared memories have made this journey special. I'm fortunate to have you by my side, and I look forward to our shared future. Your love and support have not only propelled me forward academically but have also enriched my life in countless ways.

# Contents

# List of Figures

# List of Tables

# Chapter 1

# Introduction

### 1.0.1 Background

Separation and purification processes play a crucial role in various industries, accounting for approximately half of the energy consumed in the United States.[23] The conventional methods used for these processes, such as distillations, are known to be energy-intensive. However, utilizing membrane modules offers distinct advantages over traditional thermal separation methods. These advantages include improved energy efficiency, environmental friendliness, and a smaller footprint.[24]

Regarding membrane materials, polymers have been widely used due to their affordability and ease of processing. Nevertheless, they exhibit a trade-off between permeability and selectivity, known as the upper bound. This inherent limitation has prompted membrane scientists to explore alternative materials, both inorganic and inorganic-organic hybrids. One such material of significant interest is metal-organic frameworks (MOFs), which are porous crystalline solids formed by coordinating organic ligands with metal ions. MOFs have garnered attention due to their diverse range of structures and chemical properties.

However, incorporating MOFs into membranes presents challenges because processing crystalline powders into films is difficult. As a result, MOFs are often combined with polymers to create mixed-matrix membranes (MMMs). Increasing the loading of MOFs in MMMs leads to the formation of interconnected particles and continuous

channels within the membrane, known as the percolation threshold. This loading threshold is critical for achieving a substantial effect with MOFs.[25]

Nevertheless, in practical laboratory conditions, MOFs loaded above the theoretical percolation threshold tend to agglomerate and create interphase defects, such as sieve-in-cage structures, which compromise the selectivity of the membrane towards gas molecules. This lack of compatibility between MOFs and polymers hinders the effective utilization of MOFs in MMMs.

The primary objective of this thesis research is to investigate the gas transport behavior of multidimensional MOFs (MDMs) with a branched morphology. The MDMs introduced in this study demonstrate the ability to form a percolation network within MMMs without the formation of defects, even at lower threshold loadings. This research explores the structural impact of MDMs on the gas transport behavior of MMMs and aims to uncover the fundamental mechanisms governing gas transport within MDMs. By conducting these comprehensive investigations, this thesis aims to shed light on the utilization of branch-shaped ZIF-8 in MMMs, exploring phenomena such as percolation, selectivity cut-off changes, quantitative energetics, and the influence of facet terminations. These findings will contribute to the broader understanding of membrane performance and aid in the development of advanced MMMs for various separation applications.

### 1.0.2 Goals and Outline

This thesis encompasses three primary research tracks that collectively contribute to the understanding of utilizing nanostructured branch-shaped ZIF-8 (BZ) in mixed-matrix membranes (MMMs). The first track focuses on achieving the formation of interconnected networks at lower loadings and demonstrating the percolation of BZ within MMMs.

In the second chapter, unexpected changes in selectivity cut-off observed in the multidimensional MOFs (MDMs) MMMs are explored, comparing them to typical ZIF-8 MMMs. This investigation involves a thorough analysis of the mobility characteristics of both the MOF and polymer phases.

The third part of the thesis delves even deeper into the study by quantitatively examining the energetics of permeation, diffusion, and sorption in MDM MMMs and control ZIF-8 MMMs. This analysis provides valuable insights into the quantitative aspects of gas transport in these membranes.

Lastly, the fourth part of the thesis investigates the possible origins of the selectivity differences observed in the MDM MMMs. This is accomplished by studying MMMs incorporating cubic and rhombic dodecahedron ZIF-8, which exhibit two distinct representative facet terminations, namely {100} and {110}, respectively.

ZIF-8 (Figure 1-1a) was adopted as the filler MOF for this study, because it has a small aperture size (3.4–4.1 Å) perfect for gas separation membrane[26] and good thermal and chemical stability.[27] The basic polymer studied in this project is 6FDA-DAM shown in Figure 1-1b, one of the most permeable glassy polyimide with high thermal and chemical stability and mechanical properties, and has "polymer–sieve matching" for other ZIF-8/polymer MMMs.[28, 29]

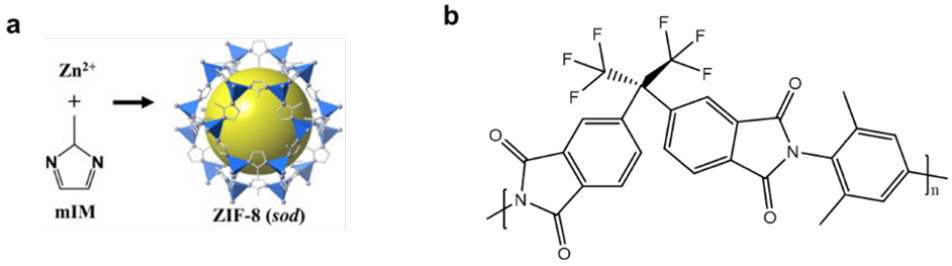


Figure 1-1: (a) Structure of ZIF-8 (Zn: polyhedral, N: sphere, C: line) and (b) 6FDA-DAM polyimide

## Chapter 2: Network-Nanostructured ZIF-8 to Enable Percolation for Enhanced Gas Transport

As addressed in the introduction, Mixed-matrix membranes (MMMs) have attracted significant attention as a promising approach to address the limitations associated with polymer-specific issues by incorporating nanoporous inorganic materials into polymer matrices. However, achieving the percolation threshold is crucial to fully harness the exceptional performance of inorganic phases. The conventional use of

sphere-like nanofillers often requires high loadings, which can lead to agglomeration and the formation of non-selective defects. To overcome these challenges, a unique morphology of branch-shaped ZIF-8 (BZ) nanoparticles has been synthesized by employing triethylamine as a structure directing modulator. This distinctive morphology automatically interconnects and readily forms percolated networks within the polymer matrix at as low as 20 wt%. A comparative analysis has been conducted between MMMs incorporating multidimensional MOFs (MDMs) with the morphology of one-dimensional nanoscopic branches connected to hierarchical three-dimensional networks (BZ) and traditional MOFs with a roughly spherical zero-dimensional morphology (rhombic dodecahedral ZIF-8, RDZ).

To understand the behavior of these MMMs, various MMM models have been employed to fit experimental data. The results revealed significant filler-filler interactions in BZ-based MMMs, deviating substantially from the assumptions of the Maxwell model, which assumes no interaction between fillers. To investigate the percolation threshold more directly, a novel acid treatment method has been successfully employed. In this method, the MOF phases in MMMs are dissolved with acetic acid, and the presence of percolation networks is determined by the transition of gas transport to the Knudsen transport regime. This transition occurs when the channels connecting the top and bottom of the membrane range from 5 to tens of nanometers, which is the width of BZ determined by microscopic images. This dramatic change has only been observed in BZ MMMs from a loading of 20 wt%, aligning with the theoretical percolation threshold estimated based on the unique BZ morphology.

The unexpected gas transport properties of BZ MMMs compared to CZ MMMs was also investigated, with a focus on the reduced cut-off size, which represents the effective pore or gate size within BZ MMMs. The observed reduction in the cut-off size from gas transport analysis can be attributed to the suppression of ZIF-8 ligand motion in polymer-ZIF composites for BZ MMMs. This gate-opening suppression behavior has been studied three different perspectives (MOF phase, polymer phase, and both phases).

First, this phenomenon is absent in the pure MOF phase characterized by pressure-

decay Fickian diffusion measurement. No difference in cut-off observed in pure MOF particles of BZ versus CZ implies that the presence of the polymer matrix influences the effective pore size and cut-off size of BZ MMMs. BET isotherms reveal similar gate-opening behavior between the pure MOF phase and MMMs, as the phase transition is absent in BZ only incorporated into a polymer matrix, whereas CZ shows the transition both as pure MOF phase and MMM state. Mechanical property analyses indicate that the BZ morphology stabilizes the polymer chains, resulting in higher mechanical moduli and glass transition temperatures. This prevents plasticization even under elevated pressures and mixed-gas conditions. In summary, the unexpected reduced cut-off size of BZ MMMs stem from the suppression of ZIF-8 ligand motion in polymer-ZIF composites and the enhanced mechanical properties of the BZ morphology.

## Chapter 3. Leveraging MOF–Polymer Confinement to Boost Hydrogen Separation Efficiency at Low Temperatures

This study builds upon the findings of the previous chapter by investigating the energetics of permeation, diffusion, and sorption in BZ MMMs and CZ MMMs. The primary objectives of this investigation were twofold: (1) to quantitatively assess the MOF-polymer interaction in BZ MMMs (above the percolation threshold loading, 30 wt%) compared to CZ MMMs (at the same loading, 30 wt%), and (2) to determine if there exists a temperature-dependent switch for gate-opening behavior.

To achieve these objectives, temperature studies were conducted using a same-volume variable-pressure gas permeation system and a dual-volume high-pressure sorption system. The temperature range spanned five different points: 7 °C (the lowest achievable temperature with the system), 20 °C, 35 °C, 50 °C, and 65 °C (the highest achievable temperature with the system). This wide temperature range was selected to provide a comprehensive understanding of the transport energetics in both membranes. The obtained data allowed for the quantification of key transport energetics, including the activation energy for permeation, sorption, and diffusion. By comparing these parameters between BZ MMMs and CZ MMMs at different

temperatures, an extensive analysis of the MOF-polymer interaction and the potential for gate-opening control across different temperature regimes was achieved.

### 1.0.3 Chapter 4.Facet-Specific Gas Transport Properties of Metal-Organic Framework in Polymer Nanocomposite

Both chapter 2 and 3 highlighted the exclusive occurrence of gate opening behavior suppression in BZ MMMs (BZ mixed matrix membranes). The current chapter aims to investigate the underlying factors contributing to this confinement of ligand motion. One aspect that has been overlooked is the potential influence of the polymer matrix, constrained by the finely dispersed MOF network, on enhancing the diffusion-driven selectivity of the polymer phase within the composite. Furthermore, the particle size effect cannot be disregarded, as significant Ostwald ripening has been observed exclusively in the membrane casting process of CZ MMMs. With the main hypothesis that BZ crystals are predominantly terminated with metastable {100} facets while CZ crystals are terminated with the more thermodynamically stable and commonly observed {110} facets, and to minimize the effect of the role of the polymer matrix in enhancing diffusion-driven selectivity and different sizes, similarly sized cubic ZIF-8 crystals terminated with {110} facets and rhombic dodecahedron ZIF-8 (RDZ) crystals were compared in MMM settings.

Collaborating with the DFT calculation group at Texas Tech, simulations and analyses were performed to explore the interaction between the {100} and {110} facets with 6FDA-DAM segments/monomer and their respective effects on gas transport. The study findings revealed that the presence of {100} facets resulted in significantly smaller effective pore sizes, indicating stronger confinement compared to the {100} facets. This observation was consistent with preliminary data from DFT calculations. Importantly, the role of the polymer matrix in enhancing diffusion-driven selectivity and the particle size effect were deliberately excluded from the study to focus solely on the comparison of {100} and {110} facets.

In summary, the study aimed to investigate the confinement of ligand motion

in BZ MMMs and CZ MMMs by specifically examining the influence of {100} and {110} facets. The study design carefully excluded the effects of the polymer matrix and particle size, allowing for a focused analysis of the role of facet orientation on gas transport properties. The findings suggested that the presence of {100} facets led to stronger confinement, as evidenced by smaller effective pore sizes, reinforcing the initial DFT calculations.

# Chapter 2

# Network-Nanostructured ZIF-8 to Enable Percolation for Enhanced Gas Transport

This chapter, with some modifications, was published in Advanced Functional Materials in 2022 [30].

## 2.1 Abstract

Membrane-based separations offer energy-efficient solutions for various applications, but commercial polymer membranes show limited performance and stability. Mixed-matrix membranes (MMMs), incorporating nanoporous inorganic materials in polymer matrices, have been of great interest to circumvent these polymer-specific issues. However, reaching the percolation threshold is crucial to leverage high-performing inorganic phases fully, yet the traditional sphere-like nanofillers require high loadings that easily result in agglomerations and non-selective defects. Here, a unique morphology of branch-shaped ZIF-8 (BZ) nanoparticles has been synthesized where its unique morphology automatically interconnects, readily forming percolated networks within the polymer matrix at loadings as low as 20 wt%. Because of the high surface-area-to-volume ratios of BZ, strong polymer–particle interactions suppress polymer

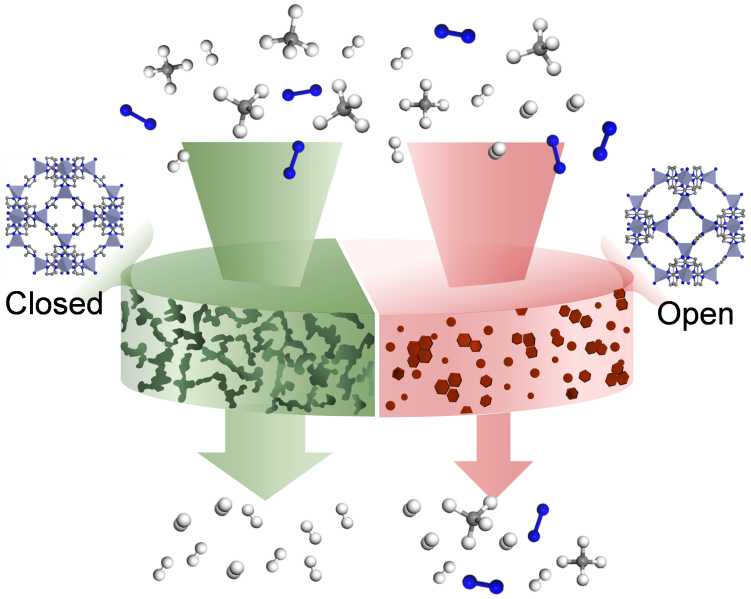


Figure 2-1: Branch-shaped ZIF-8 (BZ) has been synthesized for the first time. Compared to the typical sphere-like ZIF-8 nanoparticles, BZ readily forms percolated networks when incorporated into mixed-matrix membranes. Moreover, strong BZ–polymer interactions confine MOF ligand rotation and reduce polymer chain mobility resulting in more selective hydrogen-based separations and exceptional plasticization resistance.

chain dynamics and the rotation of the ZIF-8 ligand. This interphase confinement results in enhanced membrane stability and a smaller diffusion cut-off than traditional ZIF-8. With pre-connected diffusion pathways and confined ZIF pores, BZ MMMs significantly outperformed MMMs with sphere-like ZIF-8 for $H_2$-based separations. Overall, the findings provide a novel approach to enhancing filler effects in MMMs even at low loadings without any alignment, which could enable the development of advanced membranes in fields where percolation is desired, including separations, sensors, conductors, and batteries.

## 2.2 Introduction

Membrane separations are of great interest in the chemical industry due to their energy efficiency and small footprint. They are promising alternatives to distillation, absorption, and adsorption for commercial applications, including water purification, biogas upgrading, helium recovery, and air separation.[31] Many emerging applications still have unresolved issues related to separations, including hydrogen generation, carbon capture, and organic solvent recovery.[32] Today, separations are responsible for up to 15% of US energy consumption and more than 100 million tons of $CO_2$ emissions every year.[23] The transition to a low-energy and carbon-neutral economy requires new solutions for separations, especially for small-molecule separations, where today's commercial solutions are ineffective.[33]

To date, polymeric materials have been exclusively adopted for commercial membrane-based gas separation. Because of their low capital costs, mechanical resistance, and good processability, polymeric materials are easily formed into large-scale modules.[34] Unfortunately, polymer membranes face several challenges, including their inherent trade-off relationship between permeability and selectivity for de-mixing and stability issues such as plasticization.[17, 18, 35] The trade-off is often depicted by Robeson upper bound plots, highlighting limitations in state-of-the-art separation performance. Polymers also show decreased performance due to plasticization when in contact with strongly sorbing diluents such as carbon dioxide and higher hydrocarbons. Polymer chains swell and become more mobile during plasticization, reducing diffusion activation energies for molecular diluents, significantly deteriorating selectivity. Although polymer plasticization can be suppressed with crosslinking in some cases, this method often involves additional processing steps and sacrifices permeability.[36]

One method to overcome these polymer-specific challenges involves adopting inorganic materials such as zeolites, carbon molecular sieves (CMS), and metal–organic frameworks (MOFs) as membrane materials.[37, 38, 39] Of particular interest, MOFs, which consist of metal ions (or clusters) connected by organic ligands in periodic porous lattices, are advantageous because of their rigid crystalline structure with

tunable yet uniform pore size and affinity to specific gas molecules, resulting in superior performance and stability.[40, 41] However, pure polycrystalline MOF films are challenging to manufacture, complicating the prospects and increasing the costs of using pure MOFs as membrane materials.[42]

In response, researchers have focused on incorporating MOF particles into polymers as mixed-matrix membranes (MMMs).[43, 44, 45] MMMs can overcome the processing challenge of MOFs and the performance trade-off characteristic of polymers. Still in most cases, polymers constitute the continuous phase of MMMs, adding significant mass transfer resistance and deteriorating the benefit of the MOF phase.[46] High MOF loading can mitigate this issue by providing a continuous percolation network of MOF fillers, as Su and coworkers showed.[47, 48] However, the high-loading approach often results in unwanted aggregation and non-selective interfacial voids due to the lack of compatibility between the polymer and MOF.[42, 46]

One of the approaches to enhance the compatibility between two phases is to control the morphology of the MOF material. In our previous work, we observed that interconnected branched HKUST-1 showed exceptional MOF–polymer compatibility compared to its bulk counterpart using cross-sectional imaging and gas transport studies.[49] We have expanded this approach here to form branched ZIF-8 (BZ) under a similar fast-nucleation approach using an amine-based modulator. Unlike HKUST-1, which has a limiting pore aperture of 10 Å, the ZIF-8 lattice has a smaller crystallographic pore aperture of 3.4 Å, making it great interest for gas separations.

Here, the gas transport behavior of BZ MMMs compared to rhombic dodecahedral control ZIF-8 (CZ) MMMs was explored. The gas permeation study suggested the limiting pore size of BZ to be smaller than that of CZ and other previously reported ZIF-8 samples in the literature,[16, 15] leading to a proposed mechanism of confined ligand flexibility in BZ. Additionally, a strong polymer confinement effect of BZ restrains plasticization, which benefits practical membrane-based operations by stability enhancement. Finally, we focused on this BZ formulation as an ideal system to investigate if the percolation threshold could be traversed at lower loadings than CZ particles. Indeed, percolation could be modeled and observed through post-MMM

MOF etching experiments. With fast transport through these percolation networks, BZ provides a simple pathway to take full advantage of the MOF phase.

## 2.3 Materials and Methods

### 2.3.1 Materials

Methanol (HPLC, $\geq$ 99.9%), N,N-dimethylformamide (DMF, HPLC, $\geq$ 99.9%), zinc nitrate hexahydrate (purum p.a., crystallized, $\geq$ 99.0%), 2-methylimidazole (99%), triethylamine ($\geq$ 99%), acetic acid (ACS reagent, $\geq$ 99.7%) were purchased from Sigma-Aldrich and used as received. The $H_2$ (HY UHP300, 99.999%), $CH_4$ (ME UHP300, 99.99%), $N_2$ (NI UHP300, 99.999%), $O_2$ (OX UHP300, 99.994%), $CO_2$ (CD UHP300, 99.999%) gas cylinders were purchased from Airgas. Acetic-d3 acid-d for NMR (99.5 atom%) was purchased from Acros Organics. Chloroform-D (D, 99.8%) was purchased from Cambridge Isotope Laboratories, Inc.

### 2.3.2 Synthesis of ZIF-8 Particles

To synthesize the branched ZIF-8 nanoparticles and control ZIF-8 nanoparticles, the zinc precursor solution and organic ligand solution were prepared separately. First, branched ZIF-8 was synthesized as follows. For the zinc precursor solution, zinc nitrate hexahydrate (0.5 g, 1.68 mmol) was dissolved in methanol (20 mL). For the ligand solution, 2-methylimidazole (0.5 g, 6.09 mmol) was dissolved in methanol (20 mL). The two solutions were mixed by pouring the organic ligand solution into the zinc precursor solution, followed by the immediate dropwise addition of triethylamine (TEA, 200 $\mu$L, 1.43 mmol) while stirring (600 rpm) at room temperature. TEA expedites ligand deprotonation due to its high pKa (10.76) leading to fast nucleation, which results in smaller and randomly connected particle formation. The reaction was quenched by centrifuge after 1 h. The nanoparticles were washed three times with fresh methanol using a centrifuge to remove unreacted species. After every centrifugation step (11000 rpm, 90 min), the supernatant was disposed of and replenished

with fresh methanol. The solution was redispersed by a high-speed vortex (1–3 min), bath-sonication (30 min), horn-sonication (90 sec), and shaker (over 2 h).

Second, to synthesize control ZIF-8, zinc nitrate hexahydrate (0.5 g, 1.68 mmol) was dissolved in acetone (20 mL) and 2-methylimidazole (0.5 g, 6.09 mmol) was dissolved in acetone (20 mL), respectively. Two solutions were mixed by pouring the organic ligand solution into the metal solution, and the mixture solution was stirred (200 rpm) at room temperature for 1 h. The product was washed the same way as BZ three times with fresh methanol to remove unreacted species.

### 2.3.3 Fabrication of Mixed-Matrix Membranes

The polymer solution and ZIF-8 solution were prepared separately. First, the 6FDA-DAM polymer was dissolved in DMF solvent and stirred with a stir bar for approximately 2 h until a homogeneous suspension was obtained. Second, ZIF-8 particles were kept in solution before mixing with the polymer solution for uniform dispersion. The solvent containing the ZIF-8 suspension was exchanged from methanol to DMF by repeated centrifugation and washing three times. To fabricate targeted ZIF-8 weight loadings in MMMs, the concentration of ZIF-8 in the solvent-exchanged suspension was determined using TGA. In short, the small amount of well-dispersed suspension (100 $\mu$L) was heated in the TGA from room temperature to 300 °C at 10 °C $min^{-1}$ in an $N_2$ atmosphere to determine the concentration of ZIF-8 nanoparticles in a given-volume solution. Based on these concentration values, the pure polymer, 10, 20, 30, and 40 wt% of ZIF-8 MMM solution was prepared. The polymer solution and MOF suspension were mixed by stirring for 1 h and then horn sonicated (Qsonica, Q500) for 60–90 sec. The mixture was poured onto a glass petri dish (soda-lime Steriplan from Duran Wheaton Kimble (DWK)) and then placed in a vacuum oven (static vacuum at 0.04 bar) at 60 °C overnight. Then, a dynamic vacuum was pulled for about 3 h to remove the residual solvent in the oven. The membranes (40–60 $\mu$m thickness) were detached from the glass petri dish and annealed in a vacuum oven at 180 °C for 18 h. Each membrane was cast at least three times to evaluate reproducibility. The exact loading of the membrane was measured by TGA analysis,

further described in the characterization section.

### 2.3.4 Acid Treatment of MMMs

Pure polymer, 40 wt% BZ and CZ MMM coupons were submerged in acetic acid for 10 min and washed with DI water at least three times by immersion. There was no chemical change observed by 1H NMR for 6FDA-DAM after the treatment. The amount of residual MOF was measured by the TGA analysis described in the characterization section, indicating that $< 1\%$ of MOF remained after the acid treatment.

### 2.3.5 Pure Gas Permeation Measurement

Pure-gas permeation tests of $O_2$, $N_2$, $H_2$, $CH_4$, and $CO_2$ were performed on an automated, custom-built, constant-volume, variable-pressure permeation system (Maxwell Robotics). Membrane coupons of approximately 1 $cm^2$ in the area were cut out from as-prepared films, and their thicknesses were measured using a micrometer. These coupons were then attached to the center of a brass shim stock disk that was 47 mm in outer diameter and 7 mm in inner diameter using impermeable 5-min epoxy glue (Devcon, 14250), which resulted in an active area for permeation ranging from 10–20 $mm^2$ determined by a scanned image and ImageJ software (NIH). The samples were then loaded and sealed in a stainless-steel cell and submerged in a constant-temperature water bath set to 35 °C by an immersion circulator (Thermo Fisher, SCL150L). The leak rate measured under a static vacuum for 1 h before tests was $<$ 1% of the gas permeation rate for all tests. All samples were held under vacuum for at least 5 h before testing, and a helium flush at 1 atm followed by degassing and a 1 h vacuum hold was done before introducing different gas. Tests were conducted at least three times for each sample, and uncertainty is reported as the standard deviation. High-pressure $CO_2$ hysteresis tests (1–40 bar) were performed to characterize the plasticization resistance of all samples. During the depressurization steps, $CO_2$ gas feed pressure was decreased in increments that matched the pressurization steps.

The permeation rate of each gas was calculated from the steady-state pressure

rise in the downstream volume using the following equation:

$$P_i = \frac{Vl}{p_2 ART} \times \frac{dp_i}{dt} \tag{2.1}$$

where $P_i$ is pure gas permeability (i: $O_2$, $N_2$, $H_2$, $CH_4$, $CO_2$) in barrer ($10^{-10}$ $cm^3$(STP) cm $cm^{-2}$ $s^{-1}$ $cmHg^{-1}$), $V$ is the downstream volume ($cm^3$), l is the membrane thickness (cm), $p_2$ is the average upstream pressure (cmHg), $A$ is the active area of the film, $R$ is the ideal gas constant, $T$ is the absolute temperature (K), and $dp_i/d_t$ is the steady-state pressure rise in the downstream (cmHg $s^{-1}$) after subtracting the leak rate. The ideal selectivity ($\alpha$) was calculated as the ratio of two pure gas permeabilities ($P_i/P_j$) where i is more permeable.

### 2.3.6 Mixed-Gas Permeation

Mixed-gas permeation tests were performed on an automated, custom-built, constant-volume, variable-pressure permeation system (Maxwell Robotics). Pure polymer, 40 wt% BZ, and 40 wt% CZ MMMs were loaded in a stainless-steel cell, then placed in the system where the temperature was set at 35 °C by a built-in air-heating circulator. The gas pairs $H_2/CH_4$, $H_2/N_2$, and $O_2/N_2$ were tested (50:50 feed, 2 bar). Before these tests, all samples were held under a dynamic vacuum for at least 5 h, and pure gases were tested to confirm that the membrane gas transport properties matched earlier pure-gas tests. Most importantly, $CO_2/CH_4$ test was performed from 2 to 14 bar partial pressure to show the plasticization resistance of the samples. The downstream was held under a dynamic vacuum during each test until steady-state was reached. Then, permeate gas was collected in the downstream volume under a static vacuum, whose composition was analyzed by gas chromatography (Agilent 7890B).

### 2.3.7 High-Pressure Pure-Gas Sorption

$O_2$, $N_2$, $H_2$, $CH_4$, and $CO_2$ high-pressure (up to 50 bar) sorption isotherms were collected at 35 °C by an automated pressure decay method using a dual volume and dual transducer sorption system from Maxwell Robotics. For these tests, 0.1–0.3 g of membrane film or MOF powder was used. After sample loading, the cell was sealed with a VCR gasket, and the whole system was evacuated for 8 h to remove any dissolved gases in the films. The amount of gas sorbed into the sample at each pressure point was calculated using a mole balance between each dosing and equilibration step. Sorption coefficients were obtained by dividing the gas concentration at 1 bar ($S = C/p$). Diffusion coefficients were calculated by applying the solution–diffusion model.[50]

### 2.3.8 Kinetic Uptake Experiments

The gas sorption uptake curves on control (CZ) and branched ZIF-8 (BZ) samples were measured on the sorption apparatus at 35 °C after degassing under vacuum at 120 °C using gas molecules in a size range of hydrogen to propane (2.9–4.2 Å). Gas diffusion time constants ($D/r^2$) were extracted by fitting the fractional adsorption kinetic uptake curve with the following micropore diffusion model.[51] For an isothermal system in which the uptake rate is controlled by intracrystalline diffusion, and assuming there is only a negligible change in the adsorbed phase concentration at the center of the particle and the surface concentration is constant throughout the measurement, the solution for the transient diffusion equation for a spherical particle is:

$$\frac{M_t}{M_\infty} = \frac{q - q_0}{q_\infty - q_0} = 1 - \frac{6}{\pi^2}\sum_{n=1}^{\infty}\frac{1}{n^2}\exp\left(-\frac{n^2\pi^2 D \cdot t}{r^2}\right) \tag{2.2}$$

where $r$ is the particle's radius, $q$ is adsorbed phase concentration, and $M$ is mass adsorbed. For particles with irregular morphologies, the uptake curve solutions are

less convenient than the simple form of spherical particles, and it is common practice to use diffusion time constants.[26, 52, 53] For short times (fractional uptakes up to 0.25), 2.2 can be simplified as:

$$\frac{M_t}{M_\infty} = \frac{6}{\sqrt{\pi}}\sqrt{\frac{D \cdot t}{r^2}} \tag{2.3}$$

The diffusion time constants can be calculated by fitting fractional uptake, $M_t/M_\infty$ versus $\sqrt{t}$ using the slope obtained by the LINEST function in Microsoft Excel.[54] For small gases where the half times ($M_t/M_\infty$ =0.5) were extremely short (within 1–5 sec) due to fast diffusion, the model for long times ($M_t/M_\infty > 0.6$) was fitted.[55]

$$\frac{M_t}{M_\infty} = 1 - \frac{6}{\pi}\exp\left(-\frac{\pi^2 D \cdot t}{r^2}\right) \tag{2.4}$$

The diffusion time constants were calculated by linearly fitting $\ln(1-M_t/M_\infty)$ and $t$ using the LINEST function (Figure 2-2). Interestingly, CZ shows significantly lower diffusivity values (by $10^{5-6}$), assuming spherical particles with a radius of 30 nm. It has been known that Fickian diffusivity is not a function of crystal size,[56] and a recent study by Zhang et al. shows comparable thermally corrected diffusivity between 200 nm and 162 $\mu$m ZIF-8. However, these two data sets were obtained using different approaches, where 200 nm ZIF-8 was back-calculated from MMMs, and 162 $\mu$m ZIF-8 data was obtained using the kinetic uptake method. A separate study reported a 5 order-magnitude difference in n-butanol diffusivity between ZIF-8 particles of 60 nm and 88 $\mu$m.[57]

To the best of our knowledge, the discrepancy we observe in this work is attributed to the nascent packing structure of BZ nanocrystals when dried under vacuum. As shown in Figure 2-3, the densely packed mesoporous BZ particles likely have multiple time scales of diffusion resistance from the outer surfaces of the dried agglomerate, so the effective thickness of the dried BZ crystals is likely much larger than that of CZ, shifting diffusion coefficients to an artificially low value. Therefore, BZ was

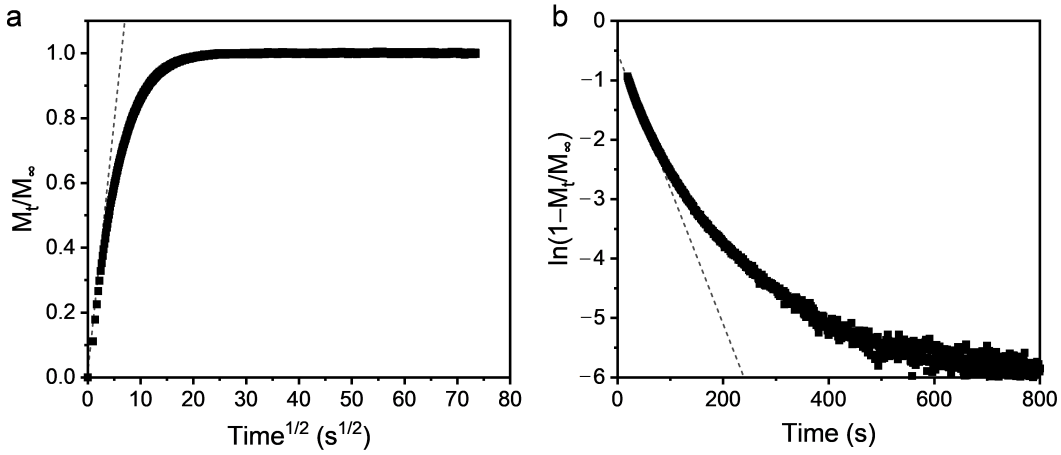


Figure 2-2: Kinetic uptake curves for BZ sample of (a) $CH_4$ using the short-time fitting approximation (Equation 2.3) and of (b) $CO_2$ using the long-time fitting approximation (Equation 2.4).

ground (GBZ) and tested the same way to test the agglomeration effect. As shown in Figure 2-4, GBZ shows 3–4 times higher diffusion time constants than BZ, suggesting a considerable resistance from agglomeration.

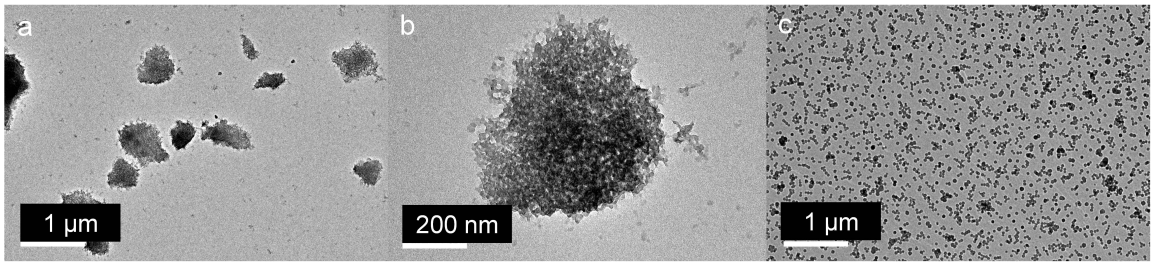


Figure 2-3: TEM image of redispersed after vacuum drying (a–b) BZ, and (c) CZ. Scale bars are shown in white.

### 2.3.9 Estimation of the Channel Dimensions of Acid-Treated BZ MMMs

As shown in Figure 2-35b and Figure 2-38, BZ MMMs show a significant loss in selectivity and a concomitant increase in permeability above 20 wt% (=28.4 vol%) loadings when treated with acid. The branch width of the BZ particle is approximately 20 nm, which matches closely with Knudsen diffusion expectations after the ZIF-8 is

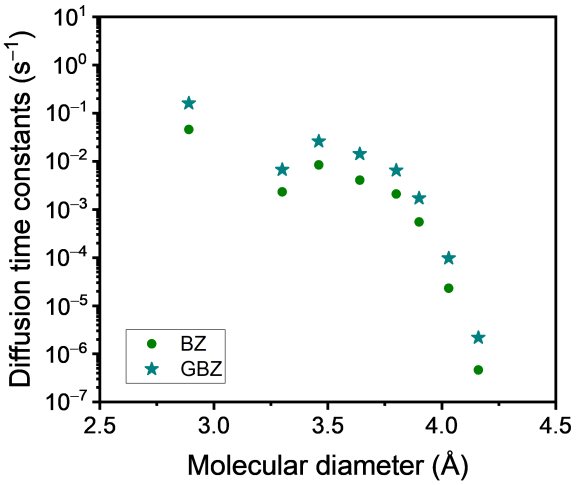


Figure 2-4: Diffusion time constants of BZ and ground BZ (GBZ).

digested to leave behind a mesoporous structure.[58] As BZ loading increases, acid-treated samples show transport properties partially reminiscent of convective flow, expected at dimensions of about 100 nm.[25] To bound our argument of channel formation, self-diffusion selectivity was calculated based on Hagen-Poiseuille's law, where the gas flux is inversely proportional to the dynamic viscosity of gases.[59] Because acid-treated membranes do not decrease below this selectivity, we confirm that only part flow is accessed with this approach, and average pore dimensions do not exceed 100 nm even at the highest BZ loadings, equivalent to five agglomerated particles.

### 2.3.10 Characterization

**Thermogravimetric analysis(TGA, TA Instruments 550 Thermogravimetric Analyzer)** was used to evaluate the loading of the MMMs and the amount of residual MOF in the MMMs after acid treatment. Heating profiles were collected for a 30–800 °C scan at 10 °C min$^{-1}$ in an air atmosphere. As the final product is pure zinc oxide, the actual MOF amount in the samples can be back-calculated using the final weight of membranes to the final weight of pure MOF samples after the same procedure.

**$^{13}$C magic angle spinning (MAS) solid-state nuclear magnetic resonance (NMR)** spectra were collected on a Bruker Avance Neo spectrometer with a nominal power of 500.18 MHz and loaded with a 3.2 mm HX solids probe. All spectra were collected for 2000 scans using a spin rate of 20 kHz, a spectral width of 200 ppm, and a spin-lock at 0.02, 0.05, 0.1, 1, 2 ms. Integrated peak area values at different spin lock times were exponentially fit to spin lock time to obtain $T_{1\rho}$ for each peak.

Solution $^{1}$H-NMR spectra were collected on an AscendTM spectrometer (Bruker) with TopSpinTM 3.2 (500 MHz). All spectra were obtained from 1–5% ($w/v$) solutions using 0.7 mL of solvents. Acetic acid-d4 ($CD_3CO_2D$) was used for pure MOF characterization, and polymer chloroform-d ($CDCl_3$) was used for acid-treated membranes characterization.

**Attenuated total reflection (ATR) Fourier transform infrared (FT-IR) spectra** were collected on a Thermo Fisher FTIR6700 using 32 scans with a resolution of 4 $cm^{-1}$ in the range of 400–4000 $cm^{-1}$ .

**Transmission electron microscopy (TEM)** images were acquired on an FEI Tecnai (G2 Spirit TWIN) multipurpose digital system operating at 120 kV. TEM samples were prepared by loading 1–3 drops of the suspension in methanol on fomvar coated 400 mesh copper grid (Ted Pella) in the case of pure MOF samples or suspension in DMF on lacey thin carbon-coated 400 mesh copper grids (Ted Pella) in the case of MMM solution samples.

**Field emission scanning electron microscope (FE-SEM)** images were acquired on a Zeiss Merlin SEM operating at 3 kV. SEM samples were sputter-coated with a 5 nm layer of gold/palladium alloy using a Desk II cold sputter unit (Denton Vacuum LLC) to dissipate the charge of non-conductive samples.

**Focused ion beam scanning electron microscope (FIB-SEM)** images were

collected on an FEI Helios Nanolab 600 Dual Beam System with gallium ion milling to observe a smoother cross-section. The samples were saturated with methanol and then fractured after being frozen in liquid nitrogen. Next, the film surface was coated in the same manner as FE-SEM samples. Using the e-beam, a thin, rectangular platinum layer was coated, and the sample was tilted at 52°. The underside of the Pt layer was Ga-ion milled using a regular cross-section with a suitable beam current ( 6.5 nA), followed by additional lower current milling using a cleaning cross-section to obtain a smooth surface for imaging.

**Powder X-ray diffraction (PXRD)** spectra were collected on a Rigaku Smartlab Multipurpose X-ray diffractometer with Cu-K$\alpha$ radiation ($\lambda$=1.5406 Å) at a voltage of 45 kV and 200 mA. The spectra were scanned over the 2–40°($2\theta$) angular range with a step size of 0.01°.

**Brunauer-Emmett-Teller (BET) nitrogen physisorption isotherms** were collected on a Micromeritics 3Flex instrument at 77 K. MOF powder samples and MMM film samples of at least 0.1 g were loaded into pre-weighed BET tubes, and degassed for 12 h at 120 °C before each measurement in a Micromeritics Smart VacPrep. The apparent surface areas were determined with the BET method in the range between $P/P_0$ of 0.02–0.1, following the instruction in Shearer's work. [60]

**Dynamic Mechanical Analysis (DMA)** testing was performed on a Q850 (TA instrument) with oscillation temperature ramp mode. The sample size was prepared as ca. 5.3 mm by 15 mm. Measurements were taken at a frequency of 1 Hz and an amplitude of 10 $\mu$ m in the range of 30 °C to 200 °C at a rate of 3 °C $min^{-1}$. Glass transition temperatures were determined at the maximum points of loss modulus plots.

**A Differential Scanning Calorimeter (DSC250)** was also used to determine glass transition temperatures of membrane samples from the second trace of a cyclic

heating protocol run between room temperature and 420 °C, followed by heating to 550 °C at a heating and cooling rate of 20 °C $min^{-1}$.

**Dynamic Light Scattering (DLS)** analysis was conducted at 25 °C on a Zetasizer Nano S90 (Marvern) to obtain the number-averaged particle size distribution of MOF samples dispersed in methanol. The particles were dispersed at ultralow loading and sonicated before the measurements.

The elemental and chemical spectroscopic analyses were examined by **X-ray photoelectron spectroscopy (XPS)** using an ULVAC-PHI Versaprobe II instrument with a monochromatic Al K$\alpha$ X-ray source ($h\nu$ = 1486.6 eV). The X-ray source power was 50 W, and the beam spot size was 200 $\mu$ m. Survey spectra and high-energy resolution spectra were taken using pass energies of 187.85 and 23.50 eV, respectively. All spectra were obtained with a photoelectron take-off angle of 45°.

### 2.3.11 Model Fitting

For the gas transport behavior of MMMs, the Maxwell model is the most commonly used in the literature, where the central assumption includes a randomly distributed and non-interacting spherical filler phase.[61, 47] The equation is shown below:

$$P = P_m \left\{ \frac{P_f + 2P_m - 2\phi_f(P_m - P_f)}{P_f + 2P_m + \phi_f(P_m - P_f)} \right\} \tag{2.5}$$

where $\phi_f$ is the volume fraction of the dispersed phase, $P$ is the effective permeability of MMMs, and Pm and $P_f$ are the permeabilities of the polymer matrix and dispersed filler, respectively. The volume fraction has been converted from the weight loading, using bulk density of ZIF-8 (0.85 $g/cm^3$) and 6FDA-DAM (1.35 $g/cm_3$), and $P_f$ were obtained from C. Zhang et al.[26, 16]

Dilute dispersion of prolates fully oriented along the direction of flow can be described by:

$$P = P_m \left\{ \frac{nP_f + (1-n)P_m + (1-n)\phi_f (P_f - P_m)}{nP_f + (1-n)P_m - n\phi_f (P_f - P_m)} \right\} \tag{2.6}$$

where

$$n = \frac{1-e^2}{2e^2}\left( \ln \frac{1+e}{1-e} - 2e \right), \quad e = \sqrt{\left(1 - \frac{b}{a}\right)} \tag{2.7}$$

where a and b are the lengths of each axis of prolate (a > b).

Although the Bruggeman model is expected to predict higher particle loading systems better, it has not been adopted in this work. The model is still bound to the no inter-particle interaction assumption, and the effect of particle shape and agglomeration is not considered.[62, 63]

The Lewis-Nielsen model was introduced to explain the gas transport of MMMs at maximum particle loadings,[42] which is shown below:

$$P = P_m \left\{ \frac{1 + (K_E - 1)\eta\phi}{1 - \eta\phi\psi} \right\}$$

$$\eta = \frac{\lambda_P - 1}{\lambda_P + 2}, \quad \lambda_P = \frac{P_f}{P_m}, \quad \psi = 1 + \frac{(1-\phi_m)\phi}{\phi_m^{\,2}} \tag{2.8}$$

where $K_E$ is the Einstein constant, which was obtained from the literature.[64] The random orientation and packing were taken into account by introducing the geometric factor $\psi$. Boundary conditions were imposed at maximum packing where P = Pf and at the lower loading (Dirichlet and Neumann condition) to cover both dilute and maximum packing conditions.[65]

Numerical solutions were solved by MATLAB fsolve function. Here, we chose the $\chi 2$ parameter as the objective function instead of the sum of squared residuals (SSR).[66] SSR is an unweighted objective function, while $\chi 2$ uses the experimental uncertainty in each point as a weighing factor. In other words, the data point with

the smallest uncertainty is weighed the most. One caveat is that $\chi 2$ minimization can result in inaccuracies at higher loading points where the error is more significant, which can be observed in the case of oxygen (Figure 2-34), where the fitted model has a poorer visual fit at higher loadings, yet matches the lower loading points better.

### 2.3.12 Score Calculation

The Robeson upper bound is the most widely accepted metric for comparing different membranes for gas separation performance. Therefore, Qian and Asinger et al.[67] proposed the concept of "score" to easily compare different MMMs. This "score" is the perpendicular distance between a data point and the upper bound front. A positive score indicates the point is above the line and vice versa. As the Robeson plot is a log-log plot, the membrane performance score can be expressed as:

$$score = \frac{\lambda \ln(P_i) + \ln(\alpha_{i/j}) - \ln(\beta)}{\sqrt{\lambda^2 + 1}} \tag{2.9}$$

where $P_i$ is the permeability of gas $i$, $\alpha_{i/j}$ is the selectivity of gas $i$ over gas $j$, and $\beta$ and $\lambda$ are Robeson parameters, which can be found in the referenced paper.[18]

In this paper, the difference in score between MMMs and the pure polymer membrane, rather than the absolute score of the MMMs, was adopted to compare the effect of incorporating ZIF-8 in different polymer matrices (Figure 2-39).

## 2.4 Results and Discussion

### 2.4.1 Chemical and Structural Characterization of Branched and Control ZIF-8 and Their Corresponding MMMs

BZ and CZ particles with different morphology were synthesized according to the procedures described in the experimental section (Figure 2-5a and b). BZ, characterized as a pseudo-one-dimensional structure with randomly connected strands, was

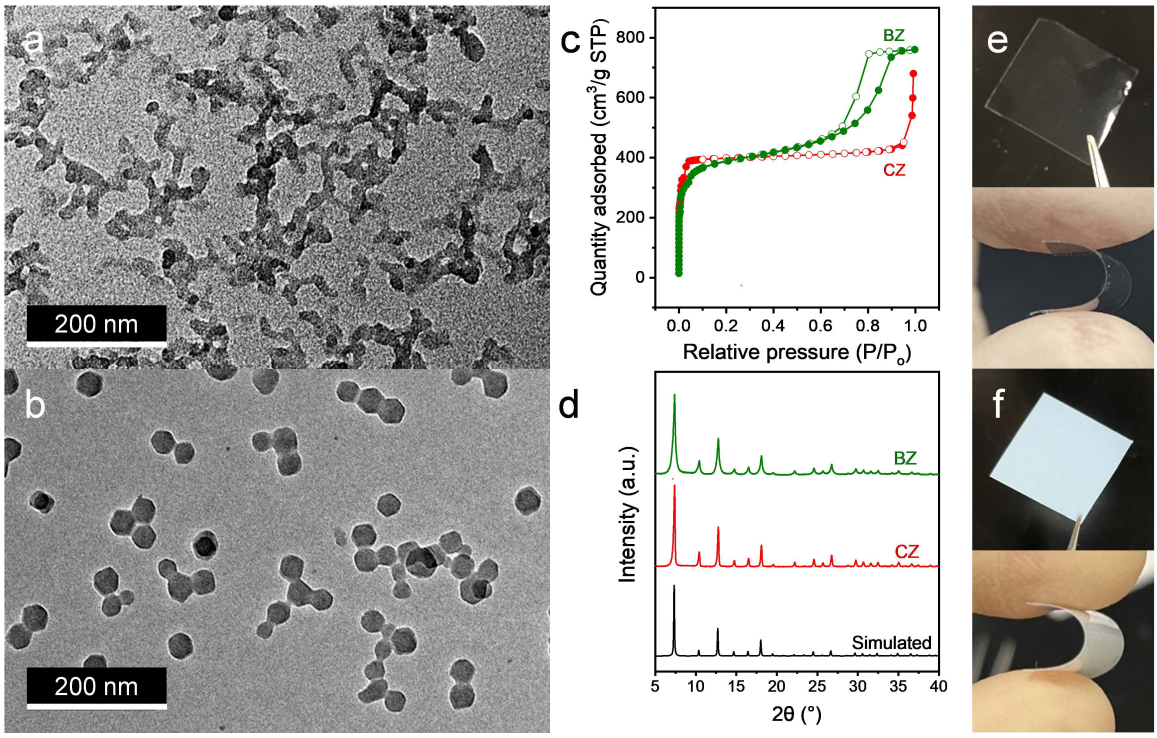


Figure 2-5: TEM images of (a) branched ZIF-8 (BZ) and (b) control ZIF-8 (CZ). (c) $N_2$ physisorption isotherm at 77 K. Filled and open circles correspond to adsorption and desorption processes. (d) XRD patterns of BZ and CZ. Images of MMMs with 40 wt% of (e) BZ and (f) CZ.

obtained using a triethylamine (TEA) modulator. In contrast, the control ZIF-8 (CZ) was synthesized without a modulator and had the conventional morphology of a roughly spherical form.

When characterized using dynamic light scattering (DLS, Figure 2-6), the branched connections and high aspect ratio in BZ resulted in a large hydrodynamic diameter of 202 ± 81 nm compared to CZ (59 ± 13 nm). Of note, the branch thickness for BZ is approximately one order of magnitude smaller than the dimensions from the DLS analysis. This difference indicates that BZ branches are not agglomerated 1D rods but 3D networks even after sonication. On the other hand, the CZ particles show similar dimensions when characterized by these two independent techniques.

The interconnected network of BZ also significantly affected the shape of the $N_2$ physisorption isotherm (Figure 2-5c). At low relative pressures, both BZ and CZ (vacuum-dried pure MOF particles) exhibited typical type 1 isotherms that represent

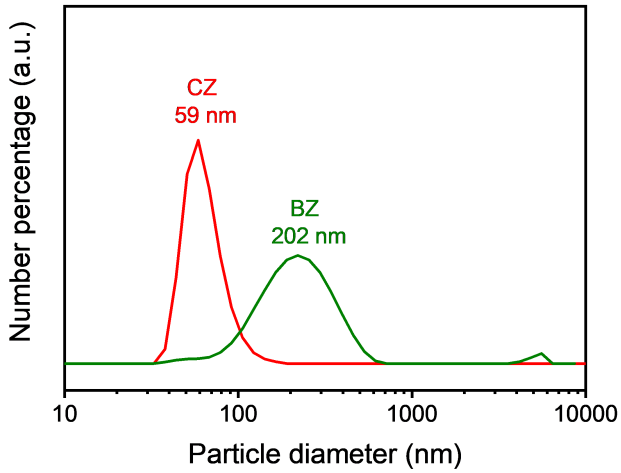


Figure 2-6: Number-averaged particle size distribution of BZ and CZ (202 ± 81 nm and 59 ± 13 nm) uncertainty was obtained from sample-to-sample standard deviation with five measurements.

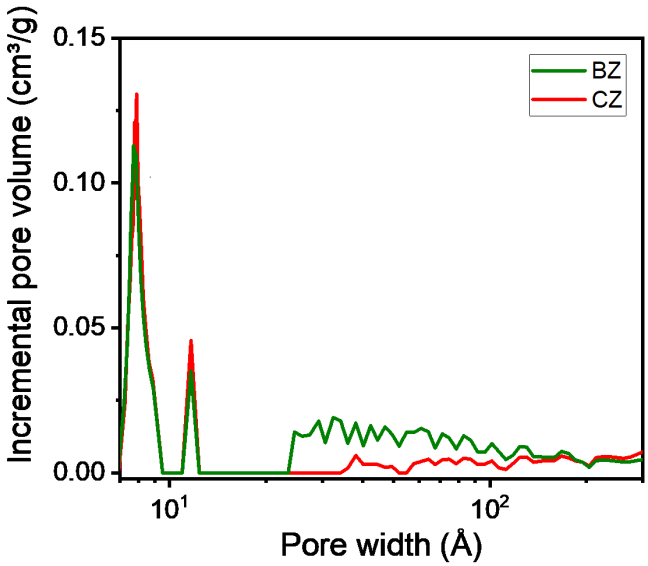


Figure 2-7: Pore size distribution by non-local density functional theory (NLDFT) of BZ and CZ. As suggested from the type IV(a) hysteresis of BZ, mesoporous characteristics were also observed in pore size distribution, where BZ shows significantly larger incremental pore volume in mesoporosity region (2–50 nm) than CZ.

microporous materials ($\leq$ 1 nm pores) with a steep uptake. However, only BZ showed type IV(a) hysteresis at high relative pressure, suggesting the presence of mesopores ($\geq$ 2 nm, Figure 2-21), which were attributed to the spacings between the branches of the dried network cages. This finding indicated that the hierarchical structure of the branched materials forms mesopores that were stable enough to endure activation for BET analysis.[68]

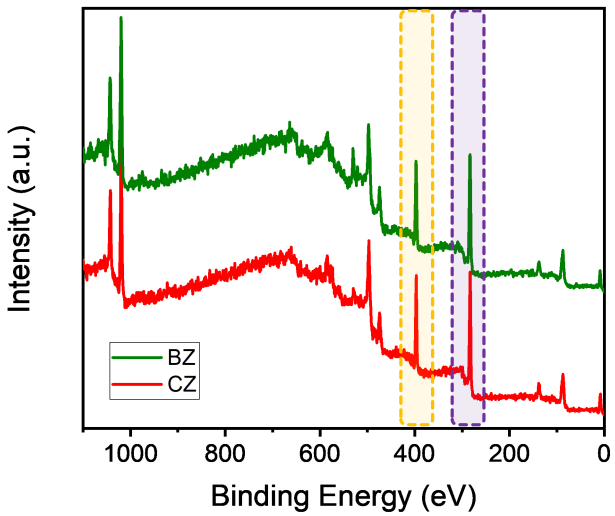


Figure 2-8: XPS full-scan spectra of BZ and CZ. The atomic ratio of nitrogen (dashed-highlighted yellow box) to zinc (dashed-highlighted purple box) is observed as 3.54 for CZ and 3.62 for BZ, where the stoichiometric ratio is 4.

Although there were distinct morphological differences, BZ and CZ otherwise showed comparable physicochemical characteristics. As shown in Figure 2-5d, they both exhibited the same crystalline phase of ZIF-8, with similar crystallite size from the Scherrer equation.[69, 62] The average crystallite diameter of BZ and CZ was 19.5 $\pm$ 0.2 and 22.7 $\pm$ 1.1 nm, respectively, which closely matched the branch width and the nanosphere size determined from TEM images. The surface areas calculated from the BET analysis were comparable (1557 $\pm$ 68.8 and 1593 $\pm$ 19.2 $m^2$ $g^{-1}$ for BZ and CZ, respectively). The atomic ratio of nitrogen to zinc for both samples was also similar (3.54 and 3.62 for BZ and CZ, Figure 2-8). Despite the use of the modulator during the BZ synthesis, there was no detectable contribution of tethered modulator

remaining in the sample after the washing steps, as confirmed by $^1$H NMR analyses (Figure 2-9).

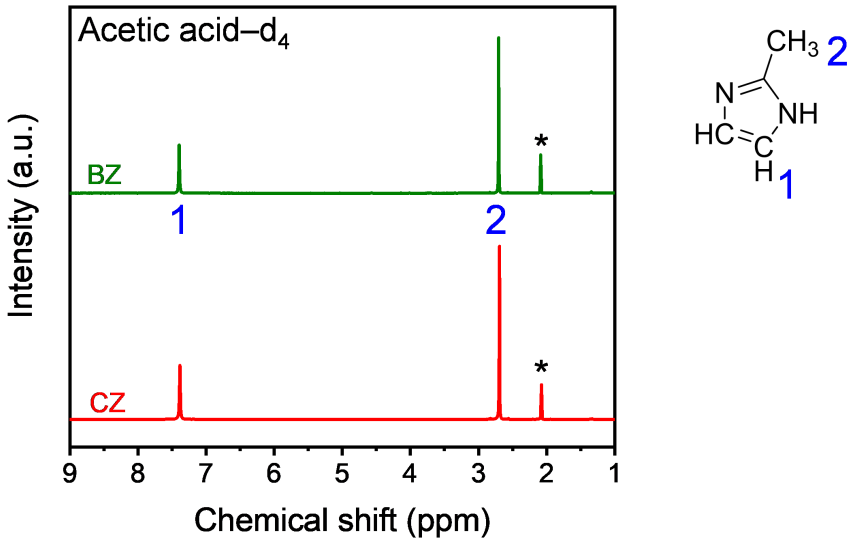


Figure 2-9: $^1$H NMR spectra of acid-digested BZ and CZ. The peak area ratios were calculated as 2:3.15 and 2:3.13, respectively (The stoichiometric ratio is 2:3). No additional peak was observed in the BZ sample, implying no modulator left after the washing steps. The asterisk indicates the solvent peak.

In order to study gas transport behavior, BZ and CZ MMMs were prepared using 6FDA-DAM as a polymeric matrix, which is known for having excellent "polymer–sieve matching" for other ZIF-8/polymer MMMs.[23,28] For all MMM samples, cross-sectional SEM images (Figure 2-10–Figure 2-15) showed uniform distributions without noticeable filler aggregations and proportionally increasing particle density with MOF loading. This trend was also characterized by energy-dispersive X-ray spectroscopy (EDX, Figure 2-16 and Figure Figure 2-17), where ZIF-8 (represented by Zn) and polymer (represented by F) were uniformly distributed. In addition, the MMMs showed a higher intensity of ZIF-8 characteristic peaks in FT-IR spectra and XRD patterns as MOF loading increased (Figure 2-18 and Figure 2-19). The exact concentrations of MOFs in MMMs were within a 2% difference from the desired loadings, confirmed by the weight of calcinated ZnO using TGA analysis (Figure 2-20).

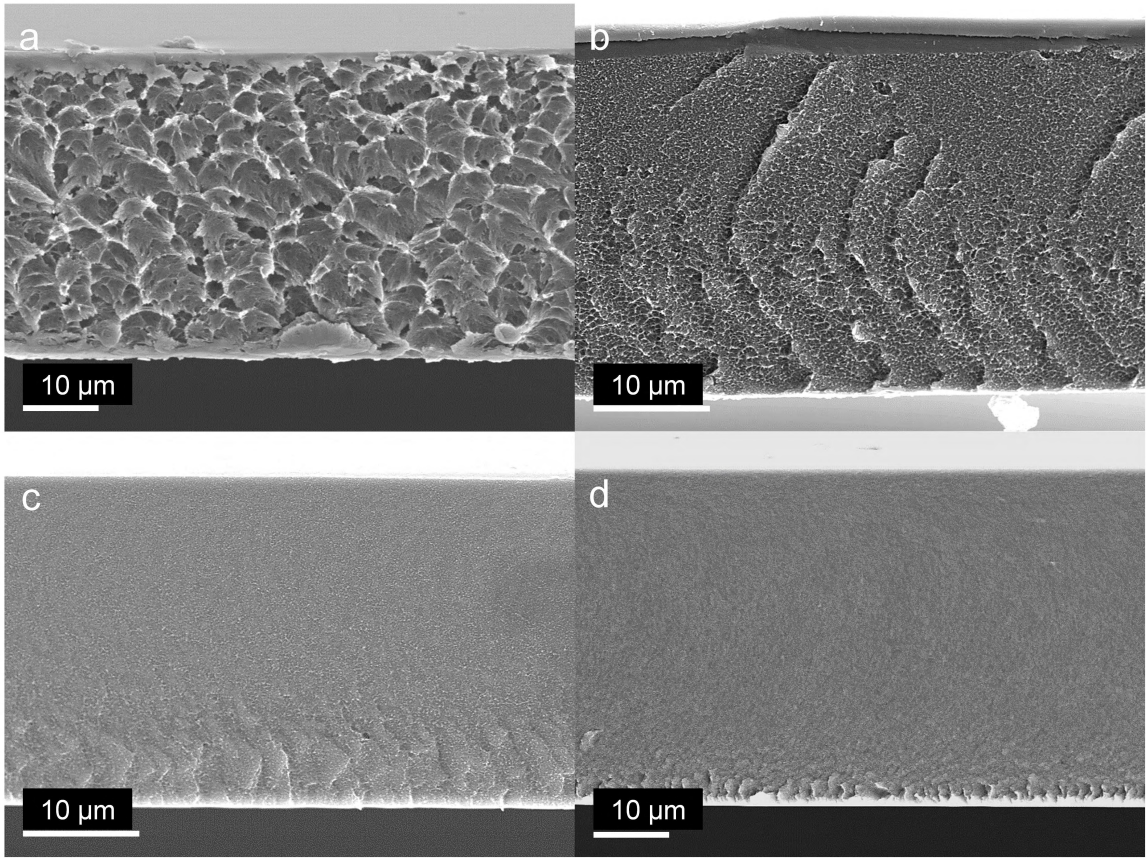


Figure 2-10: Cross-sectional FE-SEM images with low magnification for BZ/6FDA-DAM MMMs with various MOF loadings (a) 10, (b) 20, (c) 30, (d) 40 wt%. Scale bars are shown in white.

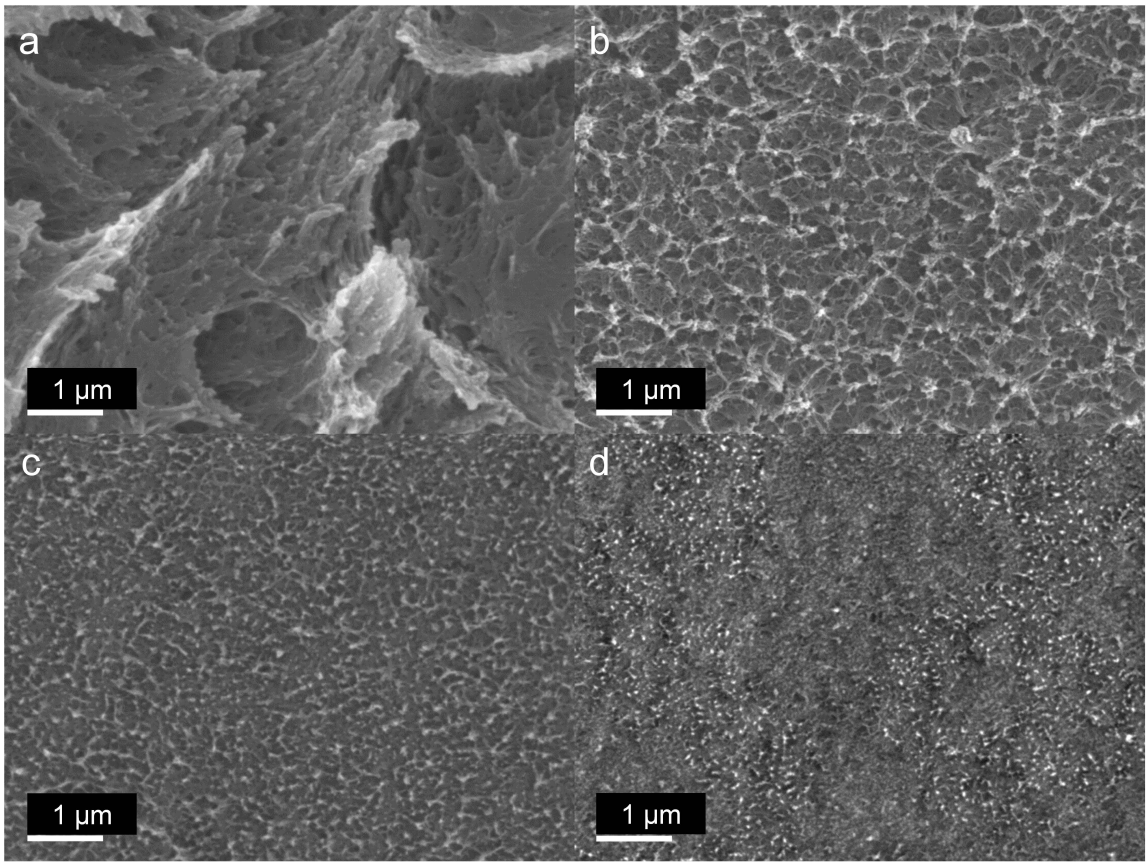


Figure 2-11: Cross-sectional FE-SEM images with high magnification for BZ MMMs with various MOF loadings (a) 10, (b) 20, (c) 30, (d) 40 wt%. Scale bars are shown in white.

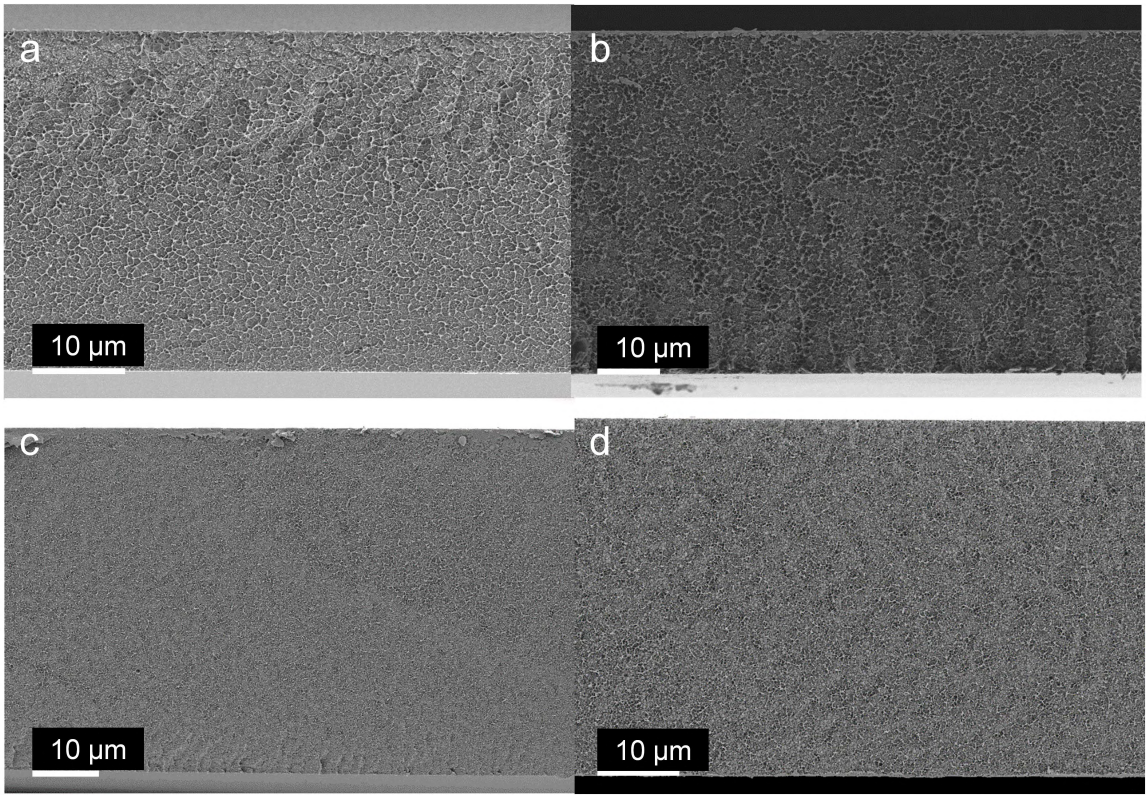


Figure 2-12: Cross-sectional FE-SEM images with low magnification for CZ/6FDA-DAM MMMs with various MOF loadings (a) 10, (b) 20, (c) 30, (d) 40 wt%. Scale bars are shown in white.

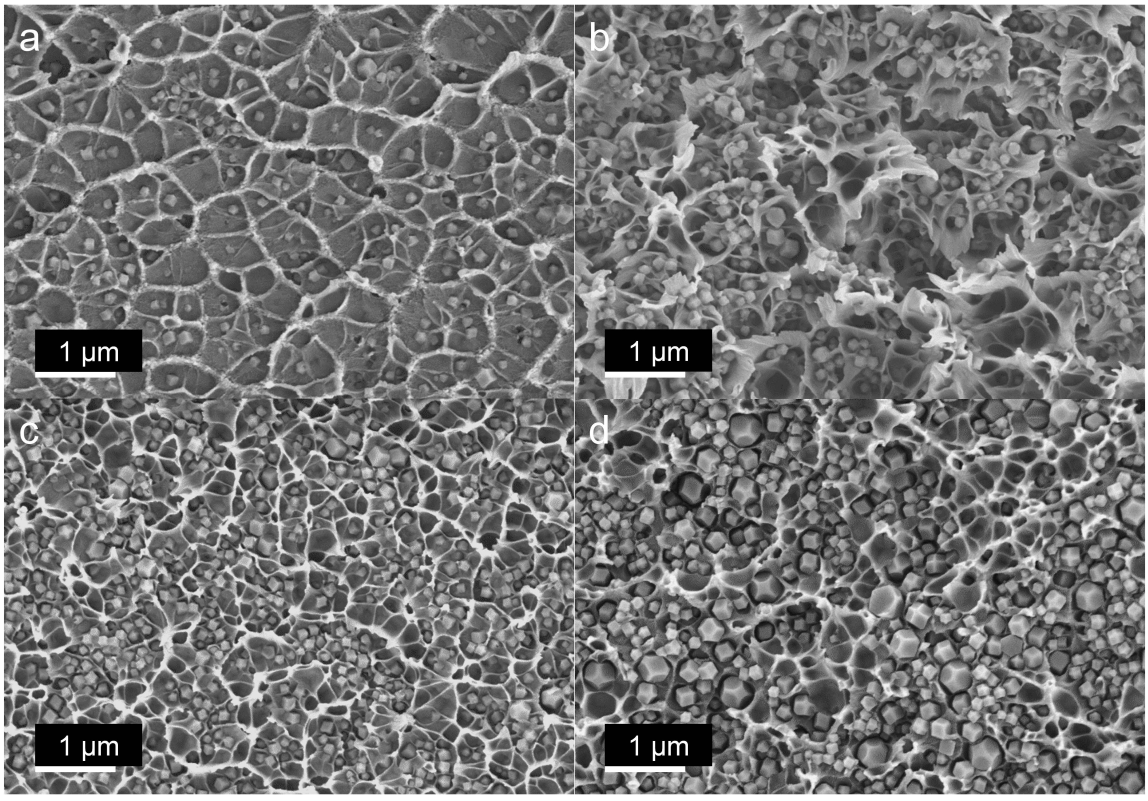


Figure 2-13: Cross-sectional FE-SEM images with high magnification for CZ MMMs with various MOF loadings (a) 10, (b) 20, (c) 30, (d) 40 wt%. Scale bars are shown in white.

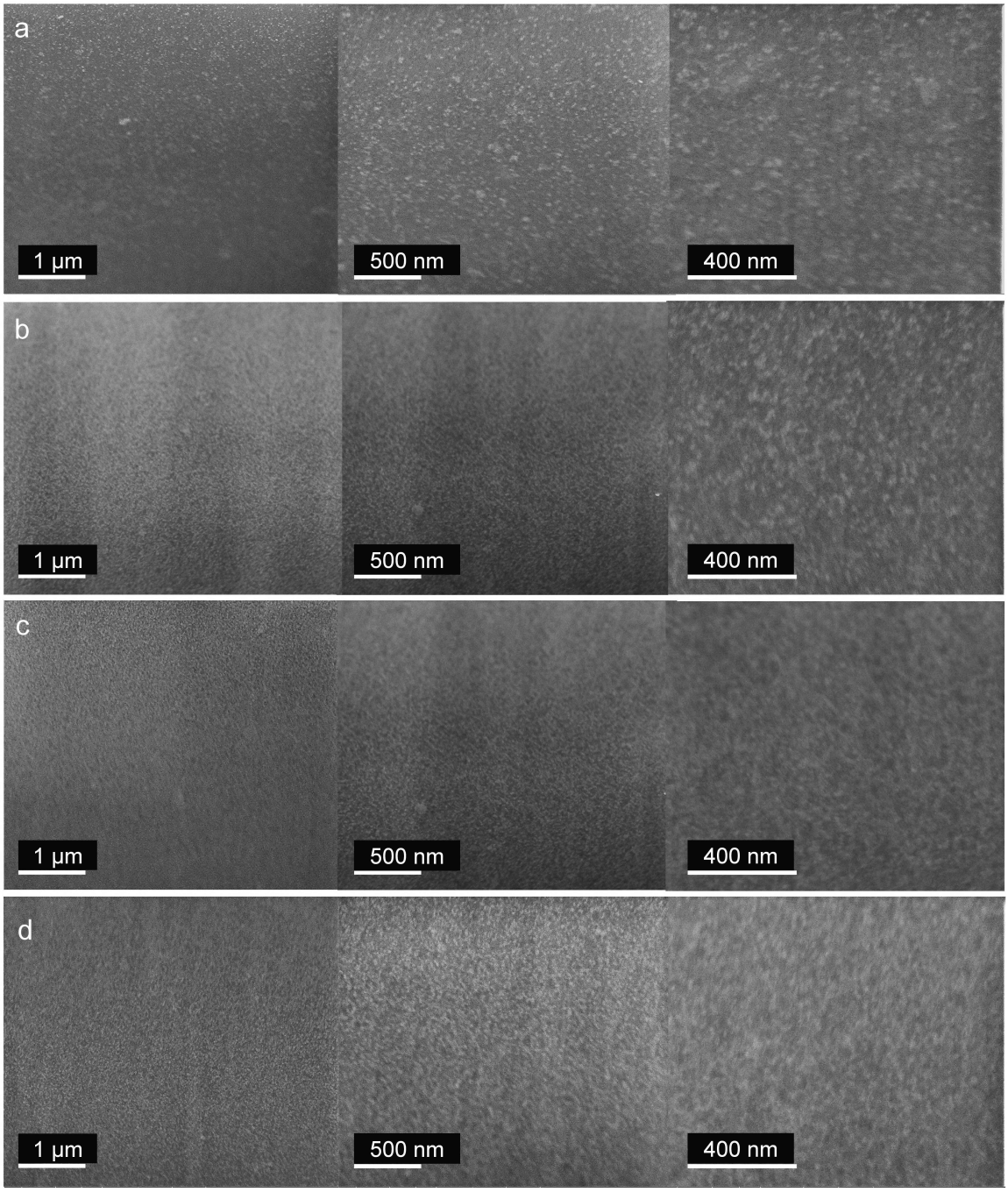


Figure 2-14: FIB-SEM images for (a) 10, (b) 20, (c) 30, (d) 40 wt% BZ/6FDA-DAM MMM, respectively. Scale bars are shown in white.

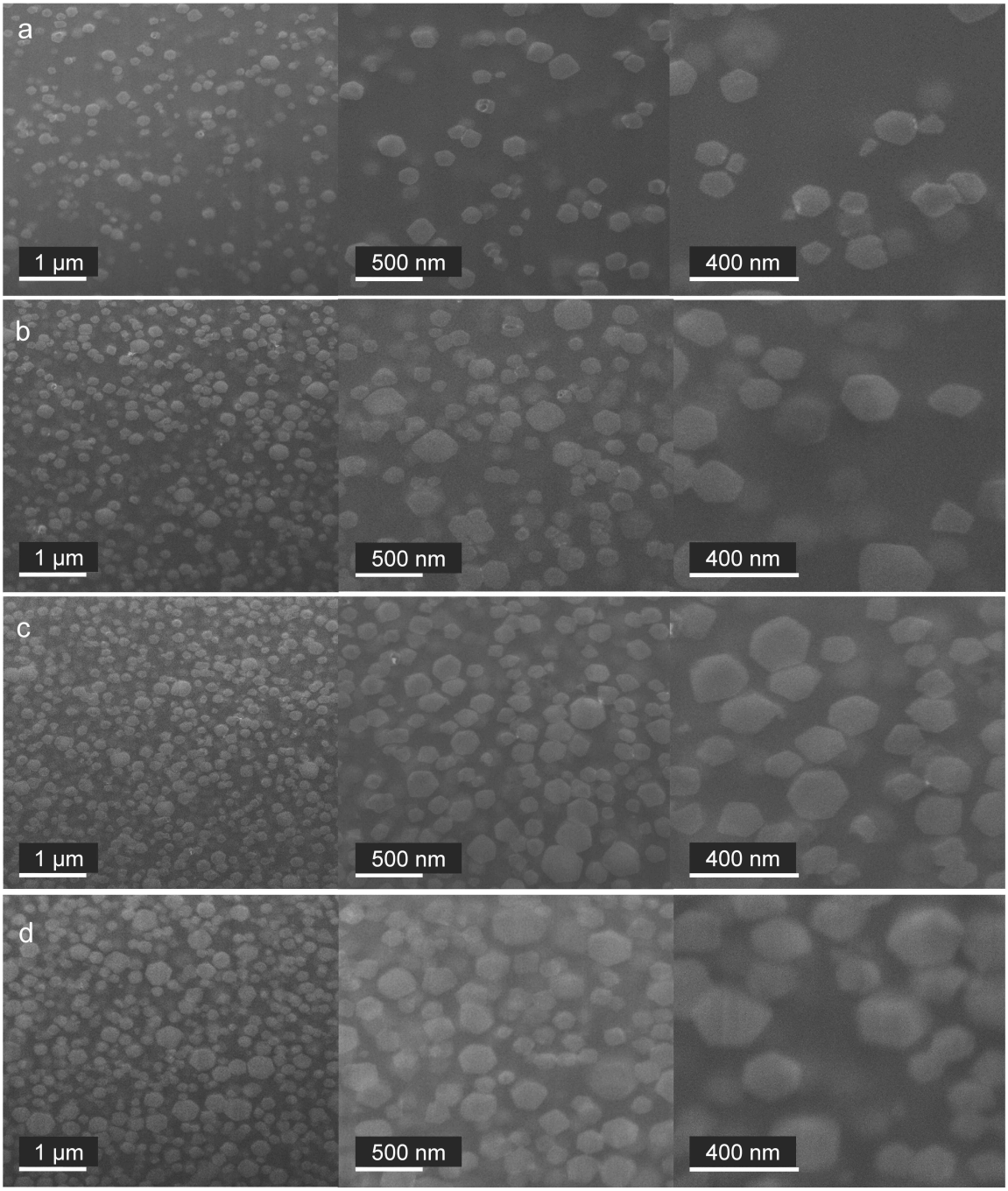


Figure 2-15: FIB-SEM images for CZ MMMs (a) 10, (b) 20, (c) 30, (d) 40 wt% CZ/6FDA-DAM MMM, respectively. Larger-sized particles than as-prepared nanoparticles appear at higher loadings, which has not been observed in BZ MMMs. This difference may be attributed to the agglomeration followed by Ostwald ripening for CZ during the membrane preparation, while the BZ remains intact as a network. Scale bars are shown in white.

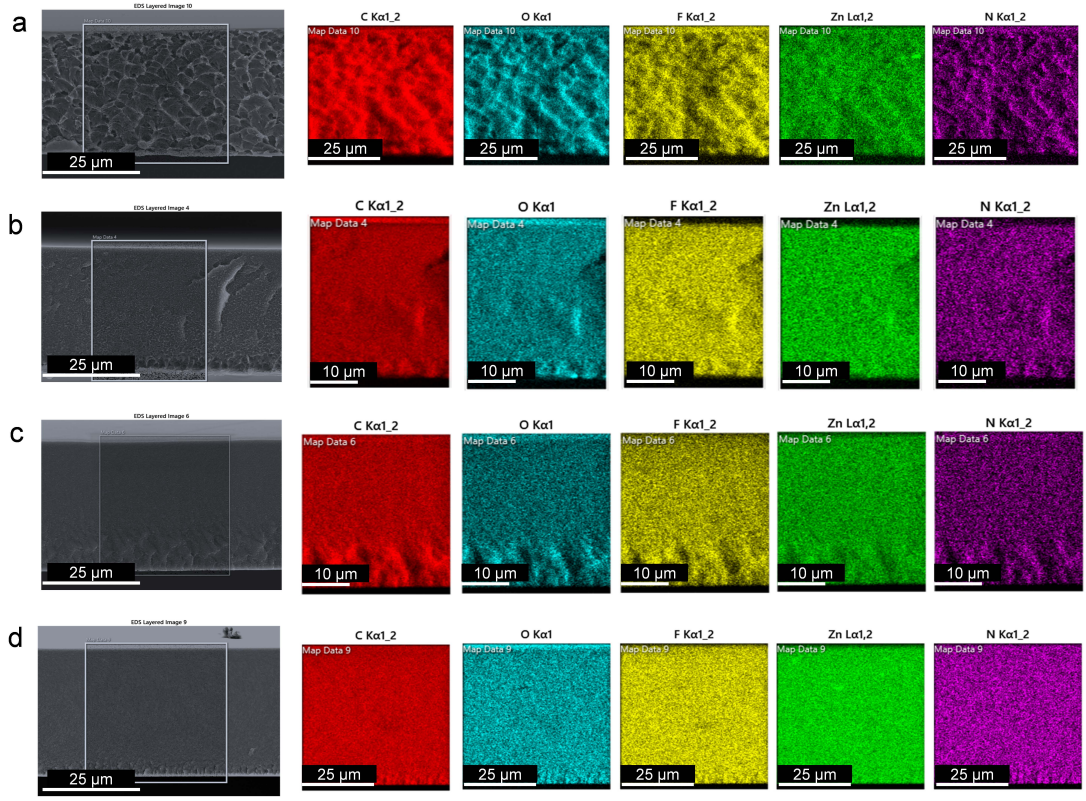


Figure 2-16: Cross-sectional SEM images and EDX analysis (C, O, F, Zn and N) for BZ MMMs with various MOF loadings (a) 10, (b) 20, (c) 30, (d) 40 wt%. Scale bars are shown in white.

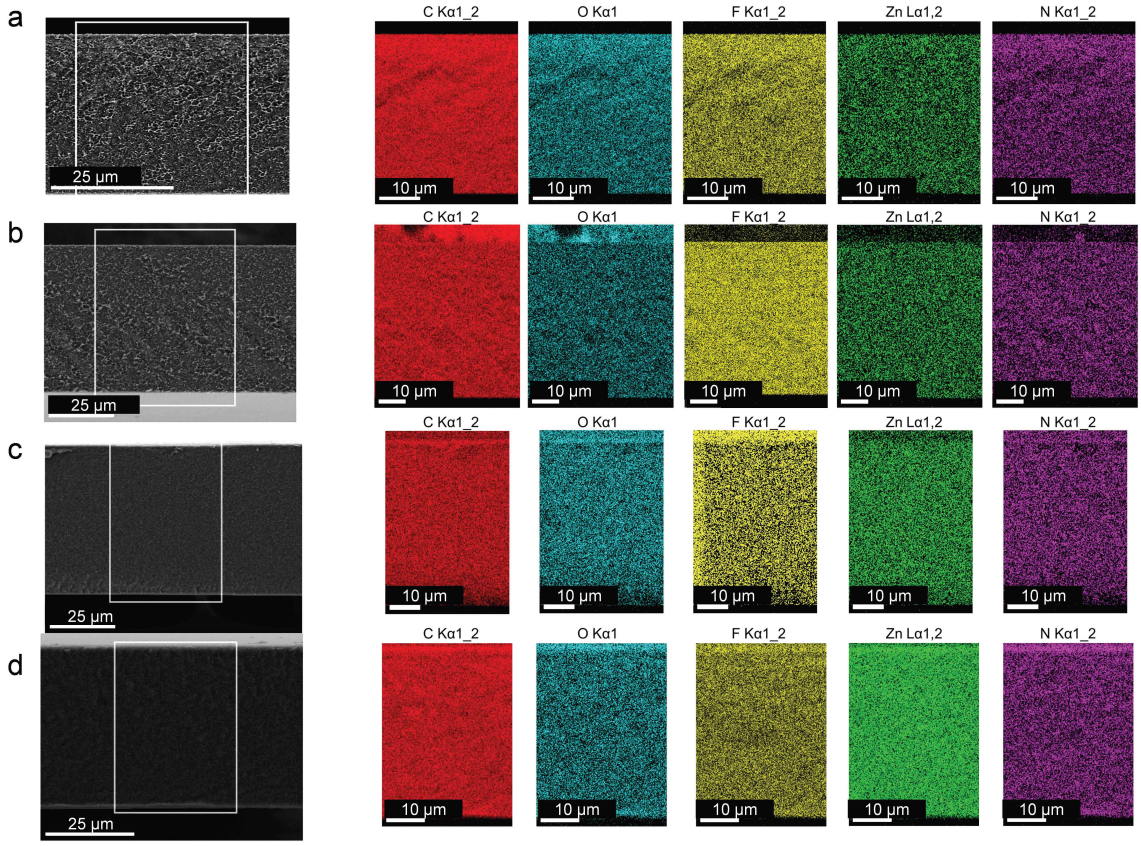


Figure 2-17: Cross-sectional SEM images and EDX analysis (C, O, F, Zn and N) for CZ MMMs with various MOF loadings (a) 10, (b) 20, (c) 30, (d) 40 wt%. Scale bars are shown in white.

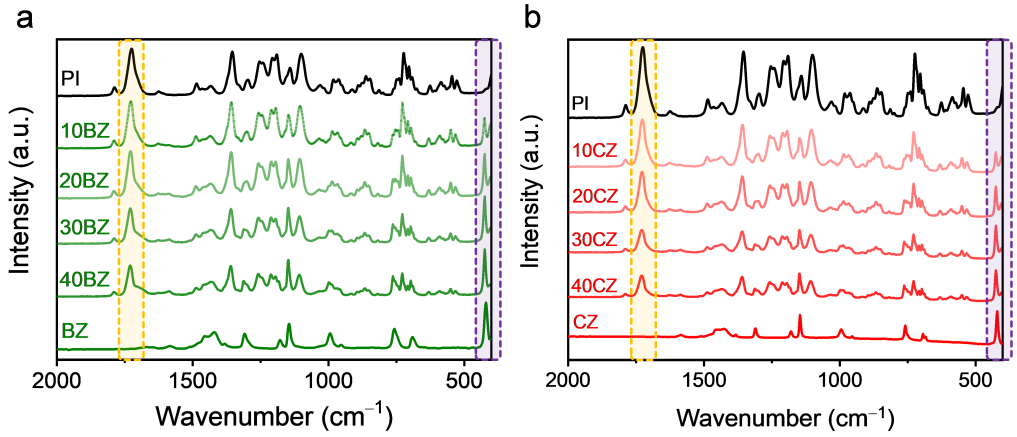


Figure 2-18: FT-IR spectra for (a) BZ and its MMMs and (b) CZ and its MMMs with various MOF loadings (0, 10, 20, 30, and 40 wt%. Dash-highlighted purple boxes indicate Zn-N bonding at 421 cm$^{-1}$ wavenumber, and dash-highlighted yellow boxes indicate carbonyl stretching.

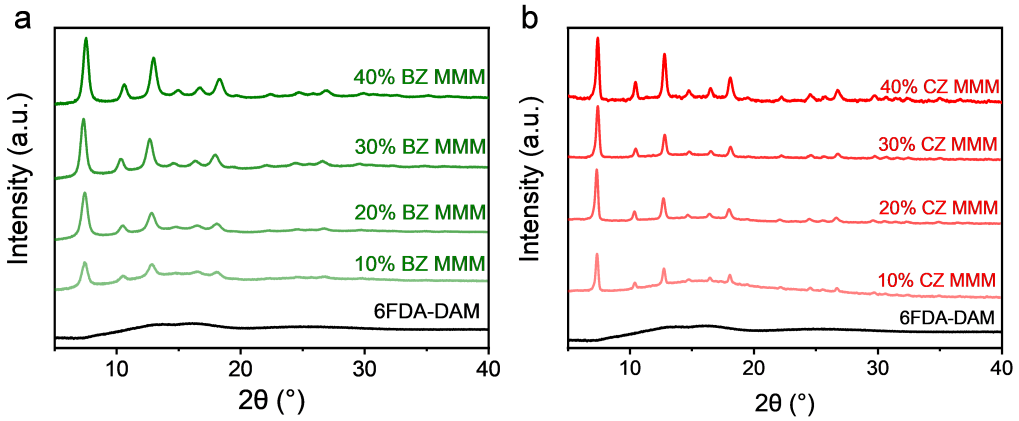


Figure 2-19: XRD patterns for (a) BZ MMMs and (b) CZ MMMs with various MOF loadings (0, 10, 20, 30, and 40 wt%).

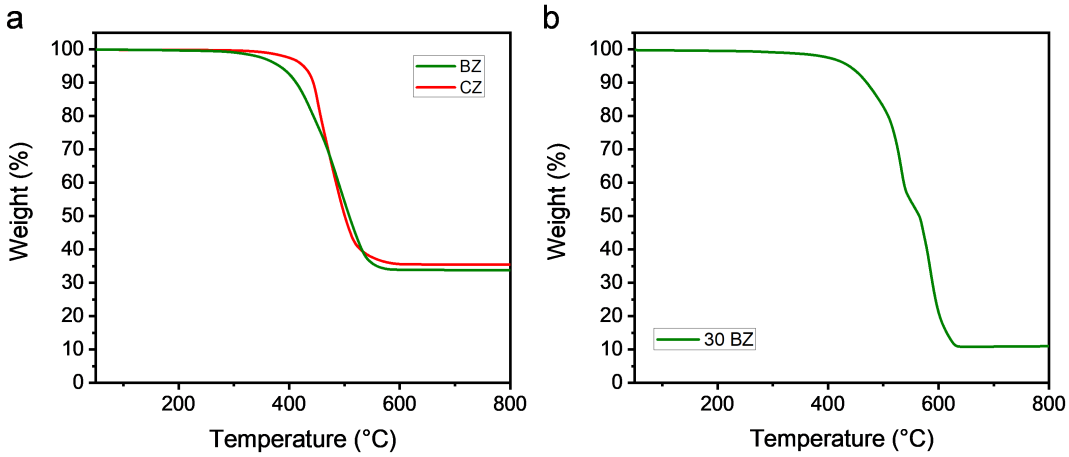


Figure 2-20: TGA curves of (a) as-prepared BZ and CZ powder under an air environment. The earlier downturn and lower residual of BZ may be attributed to the high surface-to-volume ratio of BZ, where the surface of the MOF usually has more defects than the bulk. [1] And TGA curve of (b) 30 wt% BZ MMMs under the same condition. From the final weight residue of 10.93%, the actual loading can be calculated to be 30.56 wt% using the final mass difference between the MMM and pure MOF after heating in air.

### 2.4.2 Membrane Characterization and Gas Transport Analysis

Pure-gas permeation for 6FDA-DAM polymeric films, BZ MMMs, and CZ MMMs were tested with various MOF loadings (10, 20, 30, and 40 wt%). The interactions between BZ and CZ with the polymer were systematically investigated for the individual components or MMMs using a suite of characterization techniques, including dynamic mechanical analysis (DMA) to study the polymer phase, $N_2$ physisorption to study the MOF phase, and solid-state NMR relaxation to study both phases. Then, the interconnected network of BZ was further explored using transport model fittings for the MMMs, and direct evidence of crossing the percolation threshold unique to the BZ structure was confirmed using acid treatment experiments.

#### MOF– Polymer Interconfinement

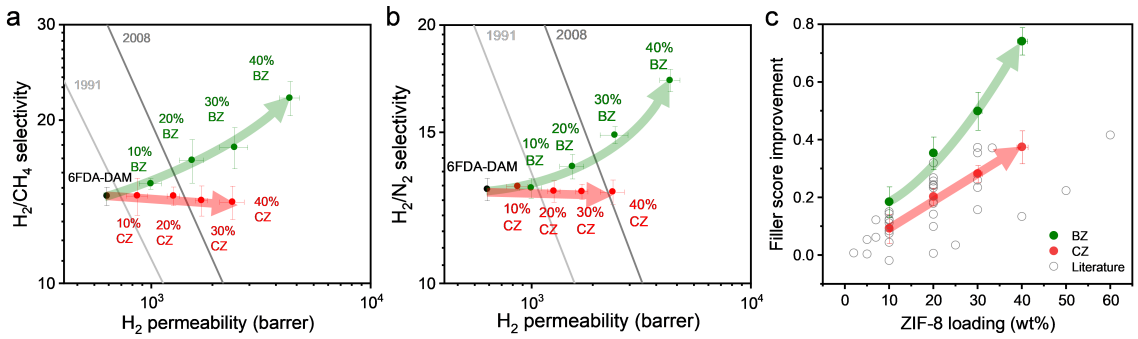


Figure 2-21: Robeson plots of a pure 6FDA-DAM polymeric film and CZ and BZ MMMs with various MOF loadings (10, 20, 30, and 40 wt%) for (a) $H_2/CH_4$ separation, (b) $H_2/N_2$ separation. (c) Performance improvement (score) with ZIF-8 addition of BZ and CZ for $H_2/CH_4$ separation compared to literature data of polyimide-based MMMs.[2, 3, 4, 5, 6, 7, 8, 9, 10] Error bars represent the standard deviations of triplicate measurements of different batches.

As shown in Figure 2-21, BZ MMMs exhibited significantly higher permeabilities and distinct selectivity trends relative to CZ. Typically, ZIF-8 shows excellent propylene (4.0 Å)/propane (4.3 Å) separation performance despite its small crystallographic pore aperture (3.4 Å) because the effective diffusivity "cut-off" is observed in the range of 4.0–4.2 Å.[70, 71, 72, 26] The discrepancy in pore sizes is attributed to a "gate open-

Table 2.1: Data set used for filler score improvement calculation for $H_2/CH_4$ (1/2).

| Pure polymer | | | ZIF-8 MMM | | |
|---|---|---|---|---|---|
| Name | $P_{H2}$ (barrer) | Selectivity ($H_2/CH_4$) | Loading (wt.%) | $P_{H2}$ (barrer) | Selectivity ($H_2/CH_4$) |
| 6FDA-DAM | 625.5 | 14.5 | 10 | 990.4 | 17.02 |
| | | | 20 | 1528 | 19.45 |
| | | | 30 | 2385 | 20.43 |
| | | | 40 | 4259 | 25.62 |
| | | | 10 | 860.2 | 14.53 |
| | | | 20 | 1257 | 14.52 |
| | | | 30 | 1687 | 14.25 |
| | | | 40 | 2334 | 14.15 |
| Matrimid | 28.8 | 120.0 | 20 | 31.2 | 173.30 |
| | | | 30 | 47.3 | 125.02 |
| | | | 40 | 71.4 | 80.06 |
| | | | 50 | 18.2 | 363.72 |
| | | | 60 | 35.8 | 358.41 |
| 6FDA-Durene | 518.5 | 17.3 | 33.3 | 2137 | 15.23 |
| HPI | 186 | 80.9 | 10 | 300.0 | 68.18 |
| | | | 20 | 365.0 | 59.84 |
| TR-30 | 194 | 44.1 | 10 | 308.0 | 41.07 |
| | | | 20 | 414.0 | 49.29 |
| TR-50 | 273 | 39.6 | 10 | 432.0 | 40.75 |
| | | | 20 | 440.0 | 54.32 |
| TR-70 | 327 | 25.7 | 10 | 475.0 | 26.99 |
| | | | 20 | 518.0 | 45.84 |
| TR-90 | 417 | 22.7 | 10 | 492.0 | 28.44 |
| | | | 20 | 1206 | 27.85 |
| 6FDA-BI | 33.4 | 278.3 | 10 | 45.7 | 240.5 |
| | | | 20 | 78.5 | 224.3 |
| | | | 25 | 79.4 | 141.8 |
| | | | 30 | 174.0 | 140.3 |
| Matrimid | 30.3 | 94.7 | 10 | 46.3 | 102.9 |

Table 2.2: Data set used for filler score improvement calculation for $H_2/CH_4$ (2/2).

| Pure polymer | | | ZIF-8 MMM | | |
|---|---|---|---|---|---|
| Name | $P_{H2}$ (barrer) | Selectivity ($H_2/CH_4$) | Loading (wt.%) | $P_{H2}$ (barrer) | Selectivity ($H_2/CH_4$) |
| Matrimid | 32.68 | 142.1 | 5 | 38.1 | 146.3 |
| | | | 10 | 52.6 | 116.8 |
| | | | 20 | 63.5 | 138.1 |
| | | | 30 | 112.1 | 96.60 |
| 6FDA-based hydroxyl polyimides | 219.7 | 70.4 | 2 | 223.5 | 70.95 |
| | | | 5 | 228.0 | 68.88 |
| | | | 10 | 237.6 | 61.88 |
| | | | 20 | 260.4 | 61.56 |
| Matrimid | 32.68 | 142.1 | 20 | 63.3 | 166.7 |
| Matrimid | 28.81 | 120.0 | 20 | 51.4 | 146.8 |
| TBDA2-6FDA-PI | 390 | 48.8 | 7 | 790.0 | 37.62 |
| | | | 20 | 1443 | 34.36 |
| | | | 30 | 2585 | 28.10 |
| | | | 7 | 600.0 | 40.00 |
| | | | 20 | 1156 | 38.53 |
| | | | 30 | 1858 | 35.73 |
| PIM-1 | 1630 | 5.26 | 11 | 2560 | 8.0 |
| | | | 28 | 2980 | 12.96 |
| | | | 36 | 5745 | 11.26 |
| | | | 43 | 6680 | 15.53 |
| PIM-1 | 3712 | 5.60 | 60 | 7700 | 6.39 |
| | | | 60 | 14533 | 5.33 |
| | | | 40 | 13695 | 7.35 |
| XLPEGDA | 16.7 | 2.56 | 10 | 43.2 | 2.70 |
| | | | 20 | 94.3 | 3.21 |
| | | | 30 | 138.5 | 3.27 |
| | | | 50 | 309.5 | 2.86 |
| PPEES | 7.9 | 31.6 | 10 | 17.5 | 64.81 |
| | | | 20 | 32.7 | 43.55 |
| | | | 30 | 92.3 | 38.48 |

ing" effect, where the methyl group of the ligand has low activation energy to rotation, allowing the transport of molecules larger than their aperture size.[73, 74] This trend was observed for CZ MMMs for propylene/propane separation, as expected, but not for BZ MMMs, where incorporating BZ resulted in a surprising decrease in selectivity and a concomitant increase in permeability for propylene/propane (Figure 2-22a). This result indicated that the traditional molecular sieving at a cut-off between 4.0–4.2 Å for ZIF-8 occurred only with CZ MMMs, and not with BZ MMMs.

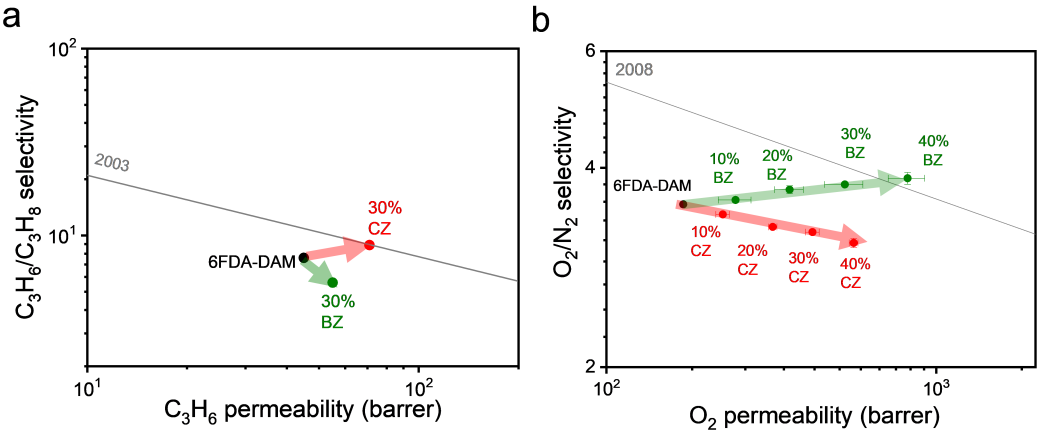


Figure 2-22: Robeson plots for a pure 6FDA-DAM polymeric film, (a) 30 wt% CZ and BZ MMMs for $C_3H_6/C_3H_8$ separations, and (b) CZ and BZ MMMs with various MOF loadings (10, 20, 30, and 40 wt%) for $O_2/N_2$ separations at 35 °C and 1 bar. Error bars represent the standard deviations of triplicate measurements.

Instead, BZ MMMs resulted in higher selectivity for light gas separations such as $H_2/N_2$, $H_2/CH_4$, and $O_2/N_2$ with loading, indicating a smaller effective pore size of BZ (Figure 2-21 and Figure 2-20b). Conversely, the CZ MMMs show constant selectivity at all loadings, as can be anticipated from the 4.0–4.2 Åcut-off. Therefore, only BZ MMMs significantly surpass the Robeson upper bounds for hydrogen separations, even under binary mixed-gas conditions (Figure 2-23). To contextualize this unexpected trend, the enhancement of gas separation performance in BZ MMMs was compared to previously reported ZIF-8/polyimide MMMs (Figure 2-21c). Here, a generalized performance improvement (called 'filler score improvement') was calculated to illustrate how MMM performance improved with increasing ZIF-8 loading relative to the Robeson upper bound front (Figure 2-24a).[67] CZ MMMs showed a

gradual increase in score with MOF loading, similar to other reported data points. However, the score of BZ MMMs increased more rapidly, where BZ MMMs outperformed other ZIF-8 MMM samples at 30 wt% and above.

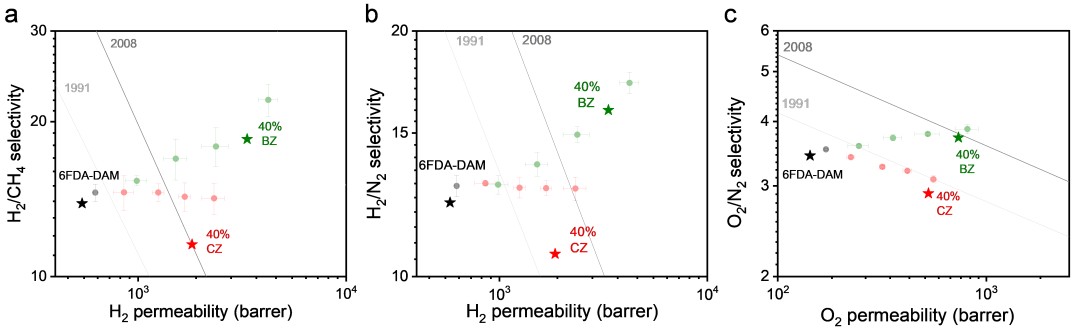


Figure 2-23: Robeson plots for gas transport performance under mixed-gas conditions for a pure polymeric film, 40 wt% CZ MMMs, 40 wt% BZ MMMs for (a) $H_2/CH_4$, (b) $H_2/N_2$, and (c) $O_2/N_2$ separations at 35 °C and 2 bar total pressure (all 50:50 feed).

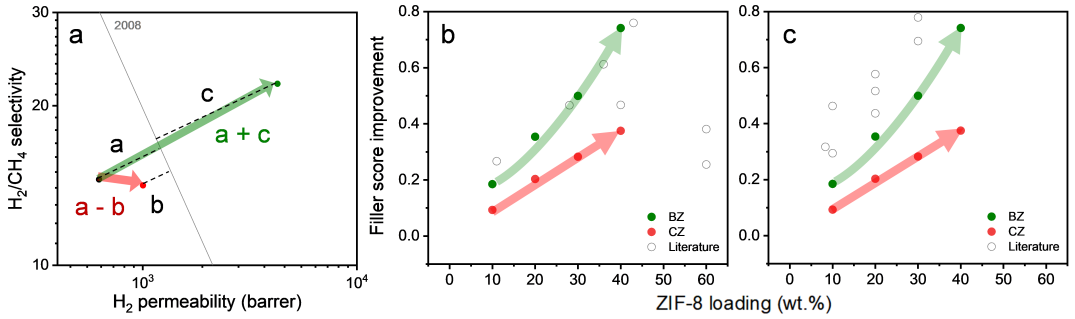


Figure 2-24: (a) Filler score improvement calculation illustration. Score data with ZIF-8 addition of BZ and CZ for $H_2/CH_4$, separation compared to literature data of (b) PIM-1 and (c) rubbery polymers. Note that the absolute performance of rubbery polymers in all cases is below the upper bound both before and after ZIF-8 addition. [11, 12, 13, 14]

More specifically, the molecular cut-off of BZ MMMs was located near the crystallographic pore size of ZIF-8 (3.4 Å), suggesting that BZ had limited ligand rotation relative to CZ when MOF samples were incorporated into MMMs. Therefore, the transport mechanism in BZ versus CZ samples was further investigated. By evaluating gas sorption coefficients for the pure polymer and CZ and BZ MMMs, it was clear that all samples had similar sorption behavior (Figure 2-25a). Conversely, the

effective diffusion coefficients were remarkably different (Figure 2-25b), which explained the distinct trends in gas separation performance for each MMM. Because the MMMs were formed with the same polymers, we hypothesized that the narrower effective pore size of BZ in MMMs could be due to either the intrinsic properties of BZ as reported previously with rapid heat-treated polycrystalline ZIF-8 membranes [75] or a difference in MOF–polymer interactions, which has not been reported to the best of our knowledge.

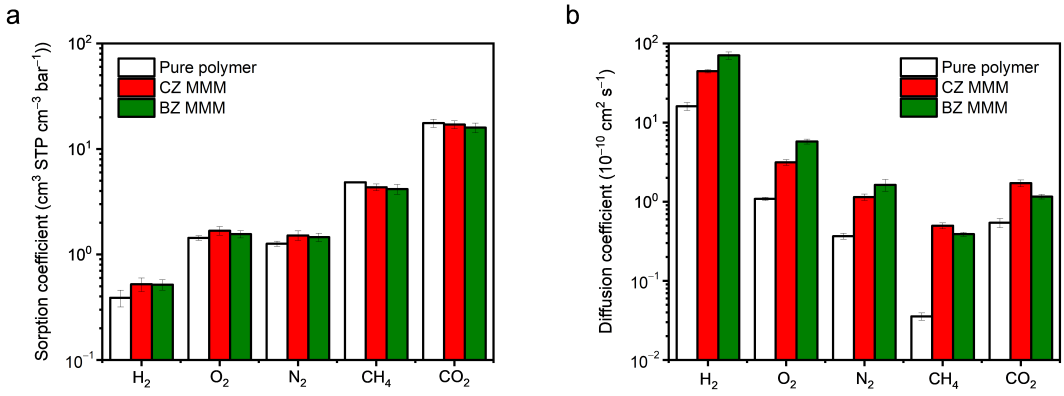


Figure 2-25: (a) Sorption coefficient and (b) diffusion coefficient of 6FDA-DAM pure polymer film, CZ 40 wt% MMM, and BZ 40 wt% MMM.

First, the intrinsic properties of pure BZ and CZ MOF powders were studied by measuring the diffusion "cut-off" using a kinetic uptake method. As shown in Figure 2-26a, both samples showed a typical diffusion cut-off for ZIF-8 around 4.0–4.2 Å, which agreed well with the previously reported ZIF-8 diffusivity trends (Figure 2-27).[65, 66] This result indicates that the pore sizes of pure BZ and CZ were comparable, which meant that the difference in selectivity was attributed not to the intrinsic pore size of MOFs but to the interaction with the polymer matrix.

Since the pure MOF powders showed the same cut-off pore sizes, the role of MOF–polymer interactions was further investigated to see if they could explain the shifted cut-off in selectivity for MMM permeation performance. There were notable differences between BZ and CZ even during the MOF–polymer casting suspension preparation step. When the 6FDA-DAM polymer was introduced to the BZ MOF

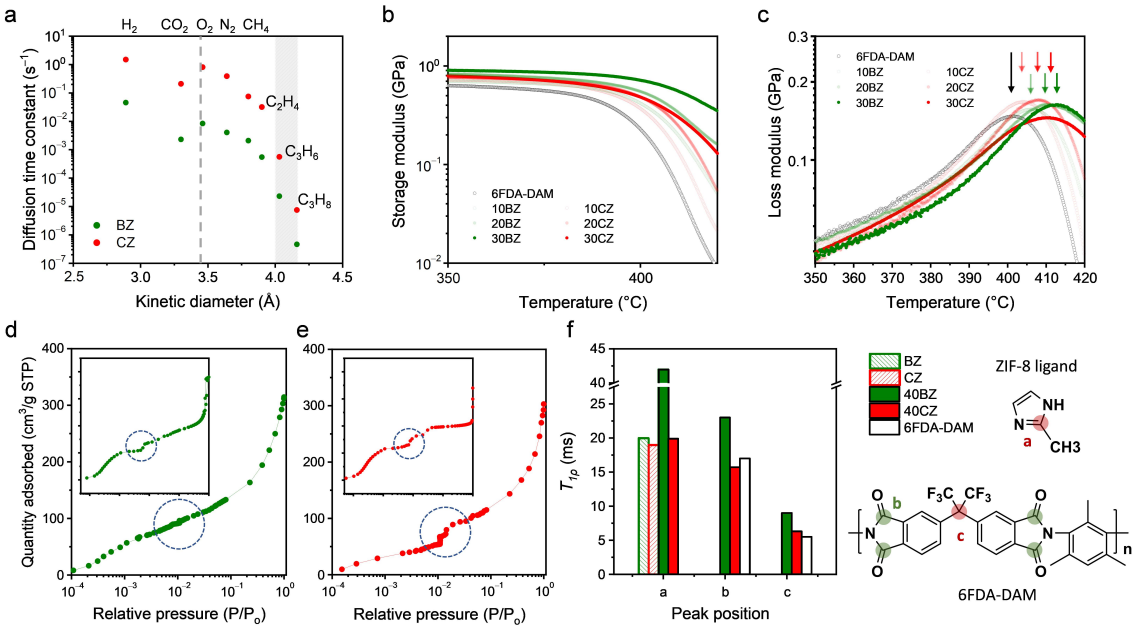


Figure 2-26: (a) Diffusion time constants of gases in size range 2.9–4.2 Åfor BZ and CZ. The dashed line indicates the crystallographic pore size of ZIF-8, and the diagonal-stripe region (4.0–4.2 Å) shows the experimental cut-off. The offset between BZ and CZ data is attributed to differences in particle packing during sample preparation. (b) Storage moduli and (c) loss moduli of pure polymer and CZ MMMs and BZ MMMs at various loadings characterized by dynamic mechanical analysis (DMA). The glass transition temperature, $T_g$, is marked with color-coded arrows for clarity. Log-log plot of $N_2$ physisorption isotherm at 77 K of (d) 40 wt% BZ MMM, pure BZ powder (inset), (e) 40 wt% CZ MMM, and pure CZ powder (inset). The x-axis and y-axis scales and units of insets are the same as in Figure 2-26d and Figure 2-5c, respectively. (f) $T_1\rho$ results from solid-state $^{13}$C NMR. The chemical formula of the ZIF-8 ligand and 6FDA-DAM with peaks labeled are also shown.

solution in the presence of DMF solvent, the mixture became highly viscous due to the pre-formed interconnections of BZ particles (Figure 2-28). Therefore, the BZ–polymer suspension formed a gel-like solution, whereas the CZ–polymer suspension was significantly less viscous (Figure 2-29).

The interaction between polymer and MOF was investigated by characterizing polymer chain mobility through DMA analysis to decouple storage and loss moduli and evaluate the glass transition temperature ($T_g$) of the pure polymer and MMMs. As shown in Figure 2-26b, the relaxation modes of the MMMs were affected by filler incorporation in all samples, where storage moduli increase with MOF loading because

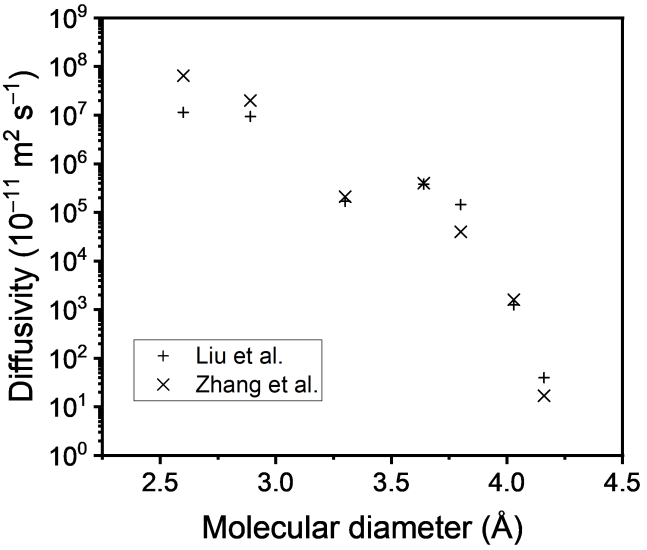


Figure 2-27: Diffusivity of ZIF-8 in previous papers, which shows the typical cut-off between 4.0–4.2 Å.[15, 16]

the ZIF-8 within the polymer matrix reduced polymer chain movement. BZ MMMs more efficiently confined polymer flexibility than CZ counterparts. In addition, $T_g$ values of samples were measured by two different methods, DMA and DSC, to support these findings (Figure 2-26c and 2.3). Both data sets showed that $T_g$ increased with filler loading, but larger increments were observed for BZ MMMs, again demonstrating more pronounced restrictions to polymer chain mobility with the BZ samples.

Table 2.3: Glass transition temperature of pure 6FDA-DAM film, BZ and CZ MMMs measured by DSC.

| $T_g$ (°C) | 0 wt% | 10 wt% | 20 wt% | 30 wt% | 40 wt% |
|---|---|---|---|---|---|
| BZ MMMs | 389.6 | 391.1 | 393.0 | 394.9 | 395.8 |
| CZ MMMs | 389.6 | 390.3 | 391.7 | 393.8 | 394.0 |

Next, $N_2$ physisorption analysis was conducted on the pure MOFs and MMMs to study the ZIF-8 gate opening phenomena. As presented in the insets of Figure 2-26d and e, pure ZIF-8 showed the commonly observed discontinuous step-wise increase

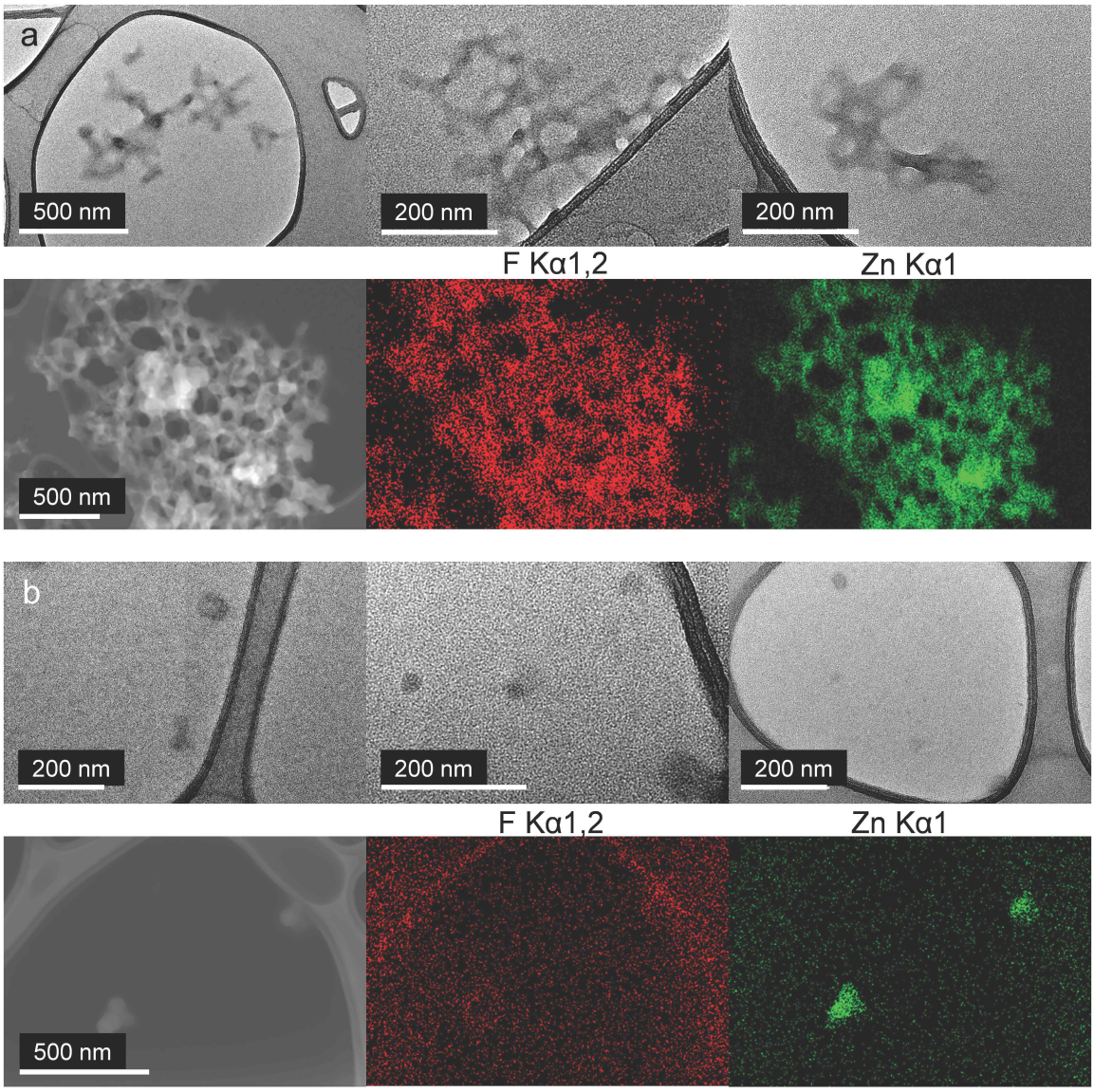


Figure 2-28: Diluted 40 wt% (a) BZ and (b) CZ MMM solution characterized by TEM and STEM EDX mapping. Both fillers are well-coated with a thin polymer layer (represented by F mapping). CZ particles exist individually or as a few particles, while BZ particles are already interconnected. This different pre-coating behavior may hinder CZ from forming interconnected networks within MMMs. Scale bars are shown in white.

of quantity absorbed near 0.01 $P/P_0$, indicating that BZ and CZ both exhibited the gate opening phenomena of ZIF-8 in their pure powder form. Once introduced to the polymer matrix, this step-wise feature disappeared for the BZ MMM, whereas the CZ MMM maintained the gate-opening phenomenon. Thus, the ligand flexibility of BZ was suppressed in the context of MMMs. This result matched well with the

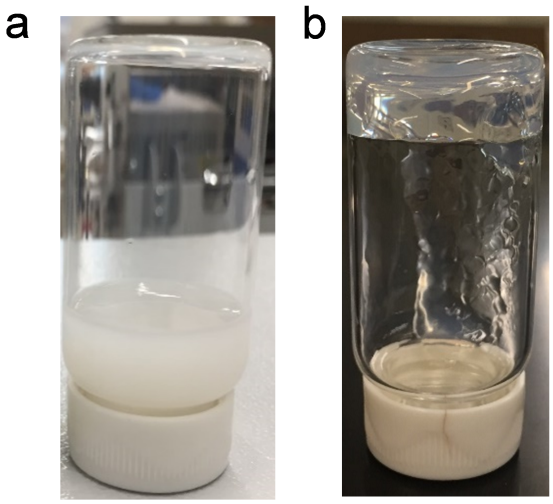


Figure 2-29: Upside down vial after mixing 6FDA-DAM solution and MOF dispersion.

gas transport study, where BZ MMMs showed a smaller effective pore size than CZ MMMs, while pure MOF samples showed the same diffusivity cut-off.

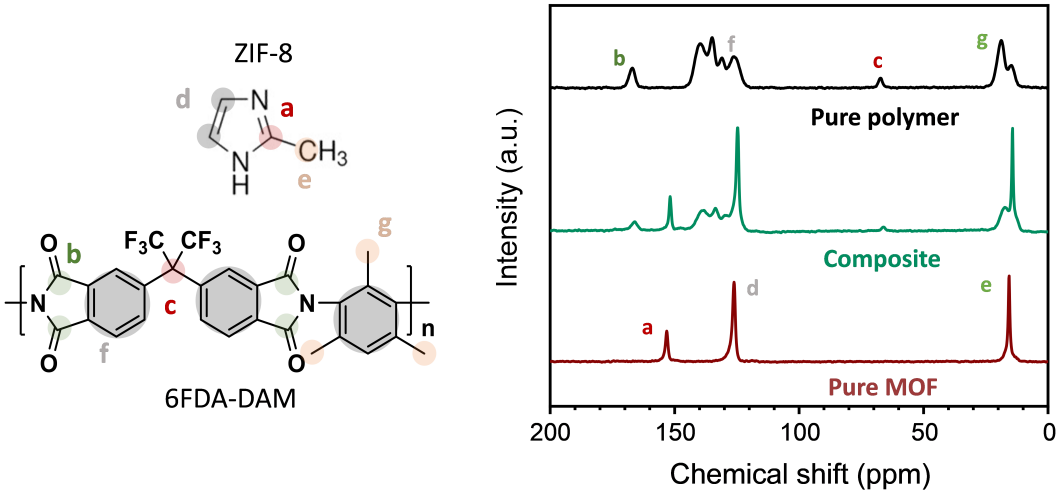


Figure 2-30: Peak locations in solid-state $^{13}$C NMR relaxation analysis plots.

In order to further elucidate this finding, both phases were analyzed together for spin-lattice relaxation times in the rotating frame ($T_{1\rho}$) using solid-state magic-angle spinning (MAS) $^{13}$C NMR, as shown in Figure 2-26f. $T_{1\rho}$ indicates each carbon site's relative mobility in the polymer and MOF phases. It provides a site-specific molecular probe to evaluate motions within the polymer chain and the MOF ligand,

especially at the frequency controlled by the spin-lock field relevant to gas diffusion in membranes.[76, 77] Increases in $T_{1\rho}$ suggest that more time is required to relax nuclear spins; thus, higher $T_{1\rho}$ values indicate that molecular structures are more rigid with respect to an applied external magnetic field.[78] The 40 wt% BZ MMM showed the most significant relaxation times for all non-overlapping peaks (the complete list of peaks is shown in Figure 2-30), suggesting more confined molecular motions in both phases. This result was particularly noteworthy because these peaks include points of motion ('a' and 'c'), the carbons essential for bending molecules in the otherwise rigid structure of ZIF-8 and 6FDA-DAM.[79, 80] Therefore, significantly larger $T_{1\rho}$ values of carbon atoms 'a' and 'c' suggested that BZ and 6FDA-DAM confined each other more effectively than CZ and 6FDA-DAM. This result was consistent with the other characterizations results described above.

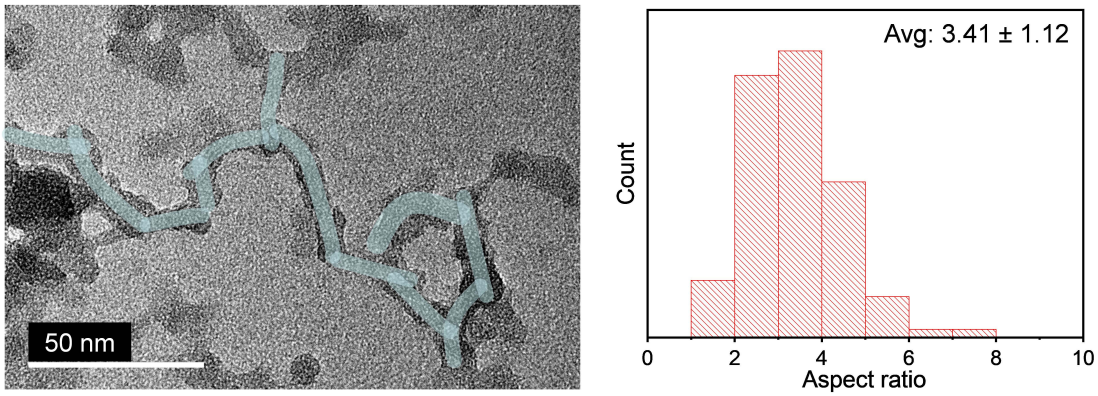


Figure 2-31: The aspect ratio of BZ nanoparticles was determined by TEM images. As shown in the left side TEM image, each connection is regarded as the end of one particle to simplify the particle shape analysis. The right side histogram shows the aspect ratio of 200 particles measured using high magnification TEM images. Scale bars are shown in white.

The origin of this interphase confinement could relate to the distinct branched morphology of BZ, as the surface-area-to-volume ratio of BZ was approximately five times higher than that of CZ, assuming BZ particles are approximated as prolate spheroids with an aspect ratio of 3.41 (Figure 2-31). Besides, considering the dimension of the ZIF-8 unit cell (a = b = c = 16.99 Å), only 6–9 unit cells could fit in

the width of branches, while 35–90 unit cells fit within the diameter of CZ particles. This significant difference implied that the surface of BZ could play a much more important role than CZ, leading to the unexpectedly high selectivity of BZ MMMs for separating small molecules. Although challenging to probe, there may be other factors that could contribute to the strong interphase confinement of BZ MMMs, such as the exposed MOF crystal facet or the subtle differences in surface chemistry below the detectable resolution of analytical techniques currently available.

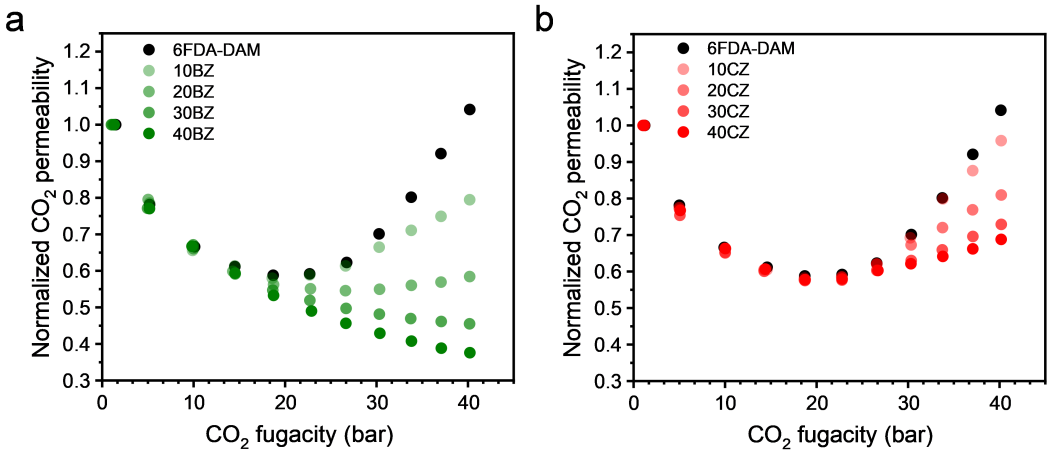


Figure 2-32: $CO_2$ plasticization pressure curves for (a) a pure 6FDA-DAM polymeric film and BZ MMMs and (b) a pure 6FDA-DAM polymeric film and CZ MMMs with various MOF loadings (10, 20, 30, and 40 wt%).

Moreover, the interconnected nature of BZ improved membrane stability. This finding relates to restricting polymer chain mobility, potentially due to multiple ZIF–polymer connection points across the branch networks. The role of the BZ structure on MMM stability was investigated by evaluating $CO_2$ plasticization curves up to approximately 40 bar (Figure 2-32). With increasing loading, BZ MMMs gradually increased the $CO_2$ plasticization pressure (i.e., the minimum points in Figure 2-32). Above 20 wt%, no plasticization pressure was observed up to approximately 40 bar. This absence of plasticization pressures under these conditions is an exceedingly rare experimental observation for glassy polymers that have not been crosslinked.[81, 82, 83] On the other hand, all the CZ MMMs showed the same $CO_2$ plasticization pressure point, although the permeability increase after the plasticiza-

tion pressure was subdued with increased CZ loading. Similarly, hysteresis loops of pressure–permeability isotherms revealed that BZ MMMs showed better reversibility compared to that of CZ MMMs and the pure polymer films (Figure 2-33). Mixed-gas permeation experiments also confirmed that BZ MMMs showed no plasticization pressures for $CO_2$ or $CH_4$ when these gases co-permeate through the MMM up to 25 bar total pressure, as shown in Figure 2-34. Notably, the CZ and pure polymer films exhibited $CO_2$ and $CH_4$ permeability increases at partial pressures lower than 10 bar, a clear indication of plasticization. The results indicated that BZ successfully stabilized the MMM by effectively confining the polymer segmental motion upon exposure to condensable gases.

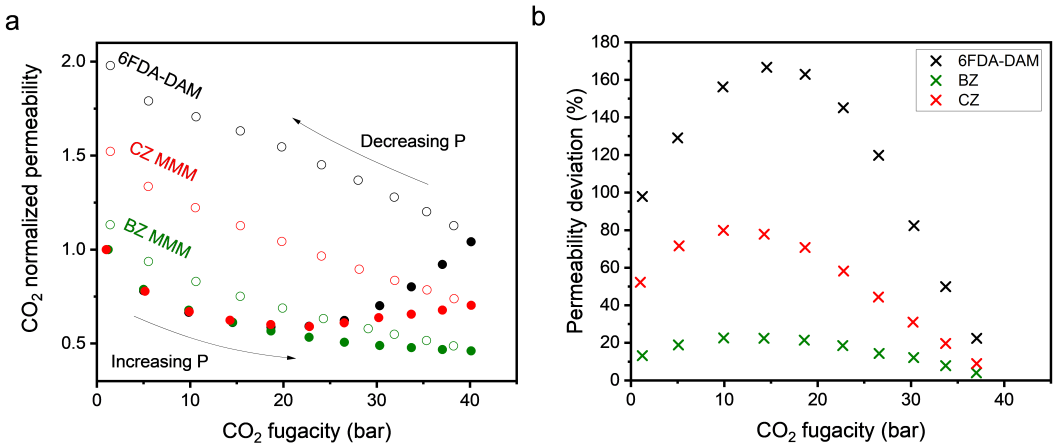


Figure 2-33: The initial gas feed pressures were set at 1 bar, and the gas feed pressure was increased to 40 bar with 5 bar increments for each pressurization step. The filled circles indicate the pressurization step, and the unfilled circles indicate the depressurization step after reaching 40 bar of initial pressurization.

### Percolation Network

In addition to different selectivity trends, BZ MMMs showed consistently higher hydrogen permeability than CZ MMMs, where the difference became more significant with increased loading (Figure 2-35a). Since CZ and BZ consisted of the same lattice structure, this trend implies that BZ provided more interconnected gas transport pathways than CZ due to its abundant MOF–MOF connections.

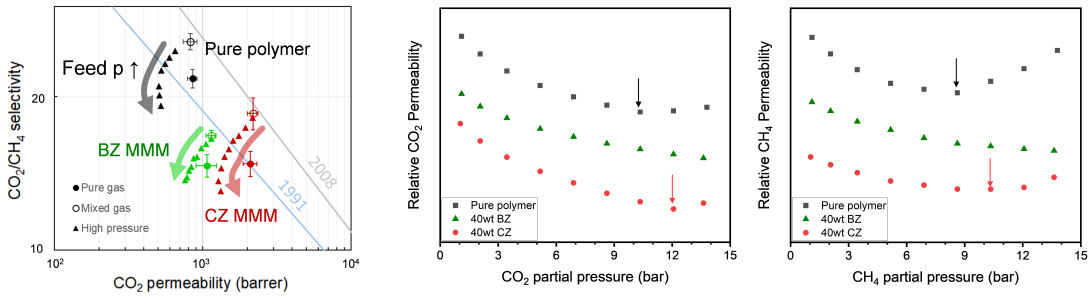


Figure 2-34: Mixed-gas performance for 40 wt% BZ and CZ MMMs tested using a 50:50 $CO_2/CH_4$ binary mixture feed at 35 °C.

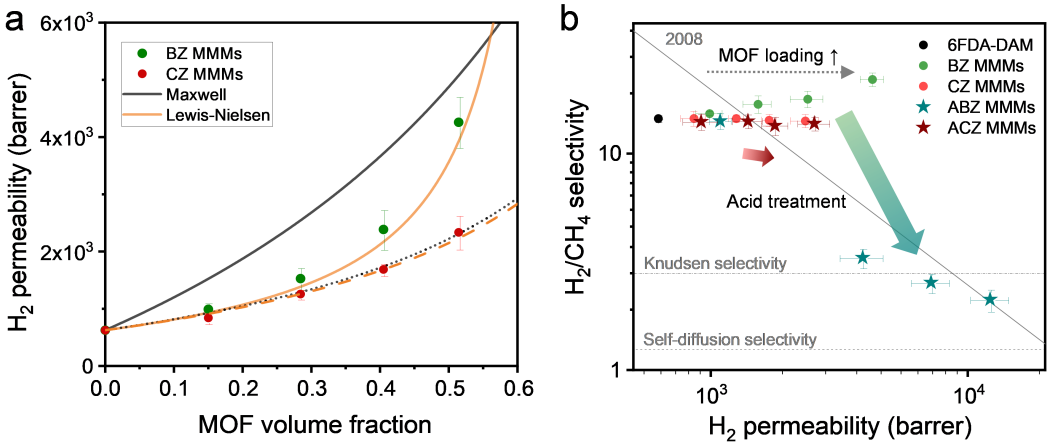


Figure 2-35: (a) $H_2$ permeability of BZ and CZ MMMs plotted with Maxwell model and Lewis-Nielsen model fittings using an aspect ratio of 3.41 (BZ) and 1 (CZ). Solid lines are for BZ MMMs, and dashed lines are for CZ MMMs. (b) Change in $H_2/CH_4$ gas separation performance after acid treatment of BZ and CZ MMMs. The maroon and cyan stars correspond to acid-treated BZ (ABZ) MMMs and acid-treated CZ (ACZ) MMMs, respectively. The black dot corresponds to the pure 6FDA-DAM film, which did not change after acid treatment. Error bars represent the standard deviations of triplicate measurements of different batches.

Permeability trends were analyzed in-depth with accessible MMM transport models to understand different filler effects. First, the Maxwell model, the most widely used model to explain and predict gas transport via MMMs, was considered. Assuming spherical particles, the Maxwell model fitted CZ data well (Figure 2-35a), suggesting that CZ is well-dispersed with minor filler–filler interactions. However, this model fitted the permeability of BZ MMMs poorly at all loadings when using a TEM-estimated aspect ratio of 3.41. This disparity could be attributed to the Maxwell model's assumption that there is no interaction between fillers, which would be violated with network nanostructure.[84]

An alternative to the Maxwell model, the Lewis-Nielsen model, was also applied to BZ MMMs, as presented in Figure 2-35a. The model assumes random orientation by adopting a geometric factor, $\psi$, designed to consider "aggregated" particles, or interconnected branched particles in this case, and loadings up to the maximum volume packing.[65] The Lewis-Nielsen model fitted BZ MMMs at all loadings within error when using the same aspect ratio for the branched particles. Additionally, the aspect ratio could be directly estimated through $\chi^2$ minimization, resulting in predictions of aspect ratios similar to experimentally observed values (Figure 2-36).

Similar trends were observed for other gases (Figure 2-36a), where both Maxwell and Lewis-Nielsen models fitted CZ MMMs data perfectly, assuming no inter-filler interaction. At the same time, the gas transport behavior of BZ MMMs could be explained only by the Lewis-Nielsen model. This result supports our assertion that BZ particles have fused and truly interconnected porous crystalline branches linked at the branch point, where percolation pathways are pre-set, altering the permeability trends in a unique and beneficial way. However, these features did not necessarily confirm a fully percolated network throughout the MMMs. This important next step in validating top-to-bottom percolation required additional proof.

To help identify percolation more definitively, additional gas transport experiments were performed on MMMs after removing the MOF phase via acid treatment. ZIF-8 is known to dissolve in weak acids, so d4-acetic acid is often used as a digesting solvent for ZIF-8.[85, 86] Therefore, the MMMs were treated with acetic acid to digest

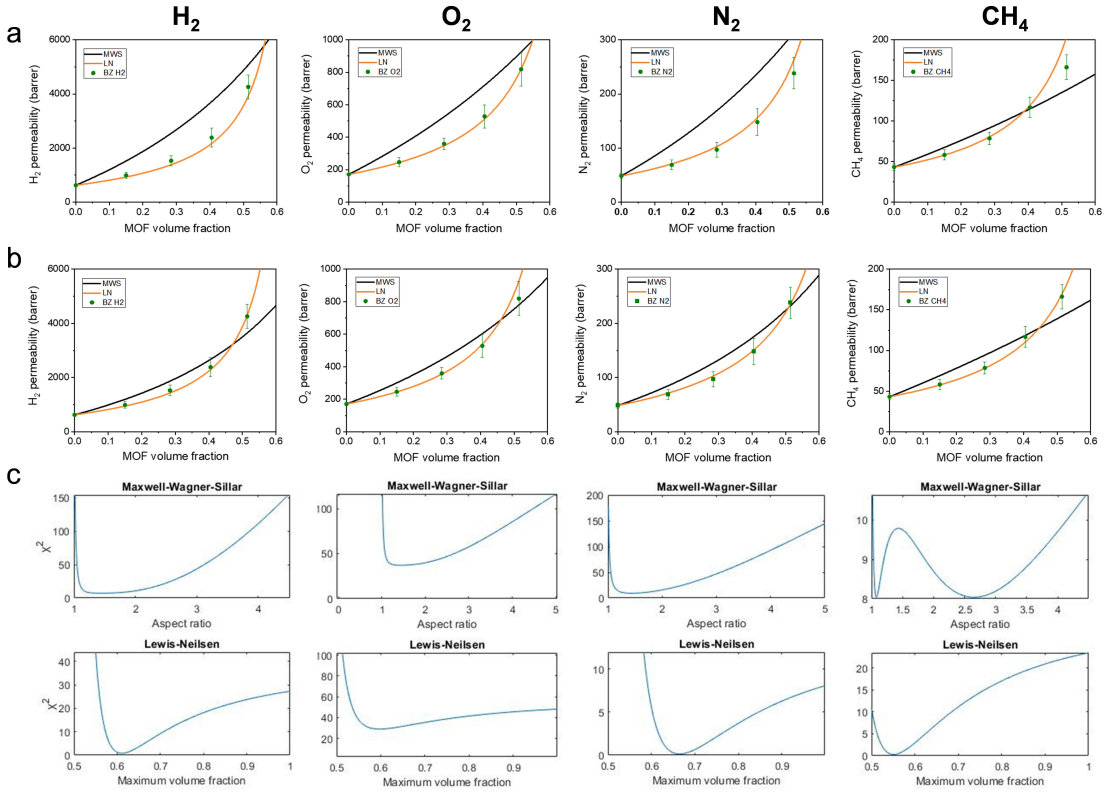


d

| Aspect ratio | Maxwell-Wanger-Sillar | $\chi^2$ | Lewis-Nielsen | $\chi^2$ |
|---|---|---|---|---|
| $H_2$ | $1.43^{+0.31}_{-0.20}$ | 7.23 | $4.01^{+0.63}_{-0.57}$ | 0.806 |
| $O_2$ | $1.43^{+0.33}_{-0.21}$ | 36.9 | $4.54^{+0.60}_{-0.95}$ | 28.9 |
| $N_2$ | $1.43^{+0.20}_{-0.15}$ | 9.23 | $2.59^{+0.95}_{-0.91}$ | 0.139 |
| $CH_4$ | $1.43^{+0.33}_{-0.21}$ | 16.0 | $1.60^{+2.44}_{-0.09}$ | 9.26 |

Figure 2-36: Maxwell-Wagner-Sillar (black line) and Lewis-Nielsen model plot (orange line) with BZ experimental data points (a) using aspect ratio of 3.41 determined by TEM images, and (b) fitted aspect ratio determined by $\chi^2$ minimization method. (c) $\chi^2$ values as a function of geometric factors (y label: $\chi^2$) (d) Aspect ratio and its error ($\sigma$) calculated from $\chi^2$ minimization and corresponding $\chi^2$ value.

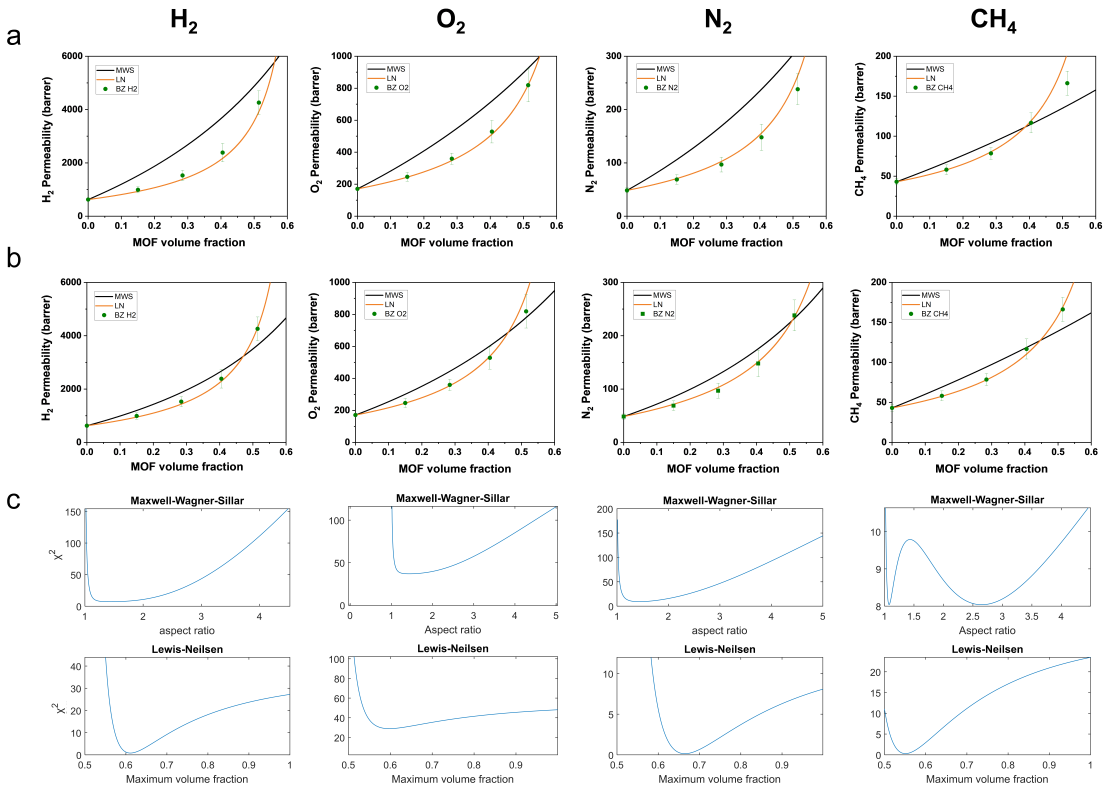


d

| Aspect ratio | Maxwell-Wanger-Sillar | $\chi^2$ | Lewis-Nielsen | $\chi^2$ |
|---|---|---|---|---|
| He | $1.43^{+0.18}_{-0.12}$ | 15.8 | $3.37^{+0.06}_{-0.08}$ | 0.166 |
| $H_2$ | $1.43^{+0.29}_{-0.09}$ | 7.23 | $4.01^{+0.13}_{-0.22}$ | 0.806 |
| $O_2$ | $1.43^{+0.64}_{-0.28}$ | 36.9 | $4.54^{+0.29}_{-0.78}$ | 28.9 |
| $N_2$ | $1.43^{+0.19}_{-0.14}$ | 9.23 | $2.59^{+0.07}_{-0.12}$ | 0.139 |
| $CH_4$ | $1.08^{+0.09}_{-0.04}$ , $2.63^{+0.88}_{-0.71}$ | 8.04 | $5.37^{+0.14}_{-0.39}$ | 0.297 |

Figure 2-37: TGA curves of acid-treated 40 wt% CZ and BZ MMMs in air atmosphere.

the MOF phase within the MMM, after which the samples were washed thoroughly with DI water several times. The absence of MOF in MMMs after this treatment was confirmed by TGA analysis (Figure 2-37). Moreover, there was no change to the polymer phase after acid treatment, as confirmed by $^1$H NMR (Figure 2-38). In other words, acid-treated MMMs were simply MOF-etched membranes containing voids that MOFs had occupied before the treatment.

As shown in Figure 2-35b and Figure 2-39, the acid-treated BZ MMMs showed a substantial loss in selectivity and a remarkable increase in permeability for loadings of 20 wt% (=28.4 vol%) and above. This drastic loss of molecular sieving capability clearly suggested the formation of a top-to-bottom MOF percolation network within

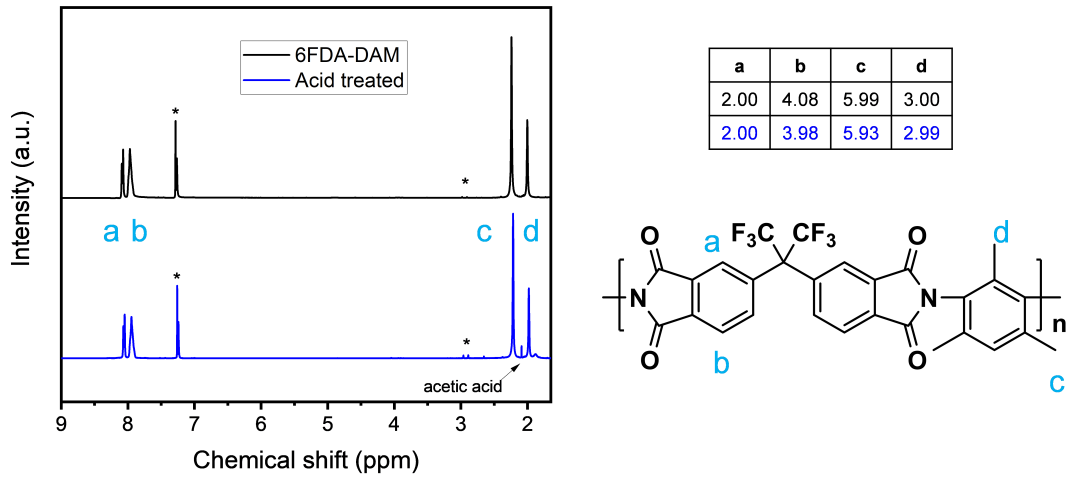


Figure 2-38: 1H NMR spectra of 6FDA-DAM and acid-treated 6FDA-DAM. The atomic ratio between each peak has not changed after acid treatment.

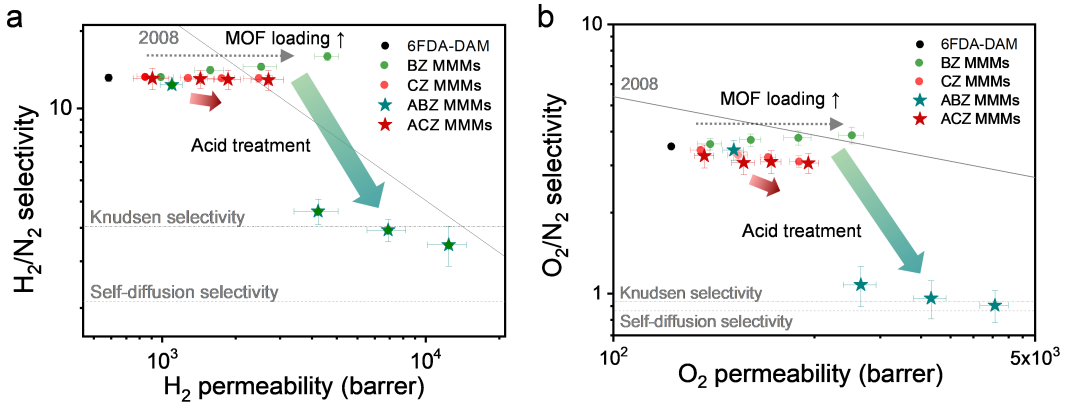


Figure 2-39: (a) $H_2/N_2$ and (b) $O_2/N_2$ gas separation performance change after acid treatment of BZ and CZ MMMs. The black data point corresponding to the pure 6FDA-DAM film did not change after acid treatment. The percolation threshold is estimated at 29.0 vol% (Equiv., 20.5 wt%) for spheres. However, to the best of our knowledge, no percolation network formation was observed in previous ZIF-8 MMM studies, even near a theoretical packing limit of spheres.[3,42] The priming effect shown in Figure S20 may explain the difference between our results and the literature.

the MMMs. This result closely matched the theoretical percolation threshold of randomly oriented and overlapping prolates at 13.9 wt% (= 20.5 vol%).[87] Additionally, this gas transport study could infer a rough dimension of the channel. After acid treatment, selectivity was observed between the Knudsen and self-diffusion selectiv-

ity (Figure 2-35b). This range corresponded closely with the branch sizes on the order of tens of nanometers. On the other hand, no interconnected network was observed for CZ MMMs at any loadings after acid treatment. Instead, they showed only a slight increase in permeability and decrease in selectivity, a typical result indicating the formation of island-like voids throughout the polymer. This novel post-casting MOF-etching experiment coupled with a gas permeation study successfully provided direct evidence of the formation of BZ percolation networks with a channel size similar to the particle dimension.

## 2.5 Conclusions

A simple method to synthesize branched ZIF-8 (BZ) at ambient conditions was developed, and gas transport behavior in the branched particles was compared to that of the typical rhombic dodecahedral sample (control ZIF-8, CZ) in mixed-matrix membranes (MMMs). BZ particles showed an enhanced interaction between polymer and MOF phases originating from the high surface contribution of BZ. This confinement impacts both phases of the composite. For the MOF phase, ligand rotation was suppressed, shifting the dominant size-sieving cut-off from propylene/propane to much lighter gases, such as $H_2$-based separations. For the polymer phase, the interconnected BZ structure reduced polymer chain mobility, resulting in improved resistance to plasticization. Most importantly, this work showed that a BZ percolation network was successfully formed within MMMs, providing an opportunity to access high-performing MOF property sets without significant mass transport limitations from the less-permeable polymer phase even at low loadings. With strong interphase confinement and percolation networks, this branching approach could improve the separation performance as well as mechanical properties and stability of MMMs at significantly lower loadings than previously required.

# Chapter 3

# Leveraging MOF–Polymer Confinement to Boost Hydrogen Separation Efficiency at Low Temperatures

## 3.1 Abstract

Temperature dependence of permeability, diffusion, and sorption coefficients of branched ZIF-8 (BZ) and control ZIF-8 (CZ) mixed matrix membranes (MMMs) for a variety of gases ($H_2$, $N_2$, $CH_4$, $C_2H_4$, $C_2H_6$, $C_3H_6$, and $C_3H_{8)}$ were conducted over a temperature range of 7 to 65 °C. Due to a strong MOF-polymer confinement, BZ MMM showed more significant temperature dependence on $H_2$-based separations. As the temperature decreases, there is a significant increase in $H_2/CH_4$ permselectivity (~80%, 27) with minor changes in $H_2$ permeability (~20%, 1804 barrer). On the other hand, with increasing temperature, separation performance converges to CZ MMM. This change is akin to a volume knob rather than a discrete switch, suggesting that manipulating the temperature could be a promising approach to fine-tune MMM performance. Temperature dependence of sorption and diffusion showed the opposite trend, yet

diffusion contribution was significantly larger, showing the mechanism behind the separation and temperature dependence is diffusive selection. This study paves the way for a deeper understanding and optimization of the temperature-dependent properties of mixed matrix membranes with flexible MOFs.

## 3.2 Introduction

Membrane separations are invaluable to the chemical industry due to their energy efficiency and compact size.[23, 88, 89] Advancements in gas separation membrane processes have provided promising alternatives to cryogenic distillation, absorption, and adsorption for commercial applications, including but not limited to, water purification, olefin-paraffin separation, biogas upgrading, hydrogen recovery, and air separation.[90, 31, 32] Polymer membranes, favored for their low capital costs, mechanical resilience, and excellent processability into high-surface-area hollow fiber modules, are subject to an 'upper bound' trade-off between gas productivity and separation efficiency.[91, 35] These limitations, depicted by Robeson upper bound plots, expose the restrictions inherent in current separation performance.[17, 18]

In an effort to transcend these constraints, inorganic membranes such as carbon molecular sieves (CMS), zeolites, and metal–organic frameworks (MOFs) have been proposed.[63, 92] MOFs, consisting of metal nodes (ions or clusters) connected by organic ligands forming periodic porous lattices, are particularly noteworthy, where their rigid, crystalline structure with adjustable, uniform pore size and affinity to specific gas molecules results in enhanced performance and stability.[40, 93, 94] However, fabricating pure polycrystalline MOF films presents significant challenges, thereby escalating the cost and complexity of utilizing pure MOFs as membrane materials.[42]

Subsequently, research has turned towards the incorporation of MOF particles into polymers to produce mixed-matrix membranes (MMMs).[43, 44, 45, 67, 95, 96] While MMMs successfully address the fabrication challenges associated with MOFs and the performance trade-offs characteristic of polymers, the continuous phase in most MMMs is typically polymer, which introduces substantial mass transfer resistance

and compromises the advantages of the MOF phase.[42, 47] High MOF loading can alleviate this issue by creating a continuous percolation network of MOF fillers,[48] yet, this high-loading strategy often induces unwanted aggregation and non-selective interfacial voids due to the incompatibility between the polymer and MOF.[46, 97, 10]

Previously, we effectively addressed this issue by engineering the morphology of ZIF-8 into an interconnected branched nanostructure, or branched ZIF-8 (BZ), that enabled percolation network formation at loadings as low as 20 wt%.[30] This uniformly distributed network structure within the polymeric matrix provided exceptional polymer phase mechanical properties and $CO_2$ plasticization resistance (up to ~50 bar). It also restrained the gate-opening behavior of ZIF-8, resulting in a effectively smaller pore size as observed through gas transport analysis at 35 °C.

In this work, we further examine the potential of the observed interphase confinement, specifically under varied temperature conditions for gas transport analyses. This in-depth study highlights distinct differences in molecular separation when incorporating control ZIF-8 (CZ) and BZ in a 6FDA-DAM polymer matrix. We provide a holistic understanding of the complex separation process by analyzing both sorptive and diffusive contributions to permeation and permselectivity over a range of temperatures (7–65 °C).

### 3.2.1 Background

The intrinsic productivity of a membrane for a specific penetrant ($i$) is characterized by permeability, denoted as the pressure and thickness normalized steady-state flux of the penetrant:

$$P_i = \frac{N_i l}{\Delta p_i} = \frac{Vl}{pART} \cdot \frac{dp_i}{dt} \tag{3.1}$$

where $N_i$ ($=V/ART \times dp/dt$, where $V$ denotes the downstream volume, $A$ is the active area of the film, $R$ is the ideal gas constant, and $T$ is the absolute temperature) presents the flux of the penetrant ($i$) through a membrane of thickness ($l$) under a

transmembrane pressure difference ($\Delta p_i \approx p$, as downstream pressure is close to vacuum). Permeability is commonly expressed in units of barrer, defined as $10^{-10}$ $cm^3$(STP) cm $cm^{-2}$ $s^{-1}$ $cmHg^{-1}$.

Gas transport through polymers and molecular sieves adheres to the "sorption-diffusion" model, where permeability is the product of an average sorption coefficient and an average diffusion coefficient:[98, 99, 100]

$$P = D \times S \tag{3.2}$$

In this equation, $P$, $D$, and $S$ represent the gas permeability, diffusivity, and solubility coefficients, respectively.

The sorption coefficient is mainly influenced by the condensability of a gas penetrant and the extent of polymer–penetrant interaction. The diffusion coefficient pertains to the capacity of a gas molecule to perform jumps within the selective matrix and can be calculated using experimental values of permeability and sorption coefficients using Equation 2. As the size of the diffusing molecules in a series of penetrants increases, $D$ values decrease. For many penetrants, critical temperature also rises with an increase in penetrant size, thereby often enhancing $S$. The resulting permeability mirrors these competing trends in $D$ and $S$ with an increase in penetrant size.[99]

The separation factor, defining a membrane's capability to separate different penetrants, is determined by the ratio of the permeability of the penetrants. Within the sorption–diffusion model, it can be written as:

$$\alpha_{i/j} = \frac{P_i}{P_j} = \left(\frac{D_i}{D_j}\right) \times \left(\frac{S_i}{S_j}\right) \tag{3.3}$$

Gas permeation and diffusion through membranes are typically activated processes, with temperature dependence outlined by an Arrhenius relationship, while gas sorption in membranes is described by a van't Hoff expression.[101]

$$D = D_0 \exp\left(\frac{-E_D}{RT}\right) \tag{3.4}$$

Here, $D$ signifies corrected diffusivity, $D_0$ is the pre-exponential factor, and $E_D$ denotes the activation energy for diffusion.

$$S = S_0 \exp\left(\frac{-\Delta H_S}{RT}\right) \tag{3.5}$$

Here, $S_0$ represents the pre-exponential factor, while $\Delta H_s$ denotes the sorption enthalpy.

The permeation activation energy, a complex parameter, is the sum of diffusion activation energy and the heat of sorption, and also follows the Arrhenius relationship.

$$P = P_0 \exp\left(\frac{-E_P}{RT}\right) \tag{3.6}$$

$$E_p = E_D + \Delta H_s \tag{3.7}$$

In Equation 3.6, $P_0$ stands for the pre-exponential factor, and $E_p$ is the activation energy of permeation.

## 3.3 Materials and Methods

### 3.3.1 Materials

Methanol (HPLC, $\geq$ 99.9%), *N,N*-dimethylformamide (DMF, HPLC, $\geq$ 99.9%), zinc nitrate hexahydrate (purum p.a., crystallized, $\geq$ 99.0%), 2-methylimidazole (99%), triethylamine ($\geq$ 99%), were purchased from Sigma-Aldrich and used as received. The

$H_2$ (HY UHP300, 99.999%), $CH_4$ (ME UHP300, 99.99%), $N_2$ (NI UHP300, 99.999%), $C_2H_4$, (EY UHP200, 99.9%), $C_2H_6$ (ET UHP300, 99.9%), $C_3H_6$ (PP P350, 99.5%), $C_3H_8$ (PR CP350, 99.0%) gas cylinders were purchased from Airgas. 6FDA-DAM (Batch: ZL11-137. MW: ~283 kDa, PDI: ~2.69) was purchased from Akron Polymer Systems and used as received.

### 3.3.2 MOF synthesis

Branched and control ZIF-8 nanoparticles were synthesized following the method detailed in our previous work.[30] Both involve creating separate zinc precursor and organic ligand solutions, with the main difference being the addition of triethylamine in the branched ZIF-8 synthesis. The reactions were quenched after 1 hour, and the nanoparticles washed three times with methanol.

### 3.3.3 6FDA-DAM and MMM film preparation

Films were also prepared following the method detailed in our previous work.[30] Given a wide range of temperatures tested, 30 wt% was chosen to guarantee the mechanical stability during the gas transport test. In short, the 6FDA-DAM polymer was dissolved in DMF solvent, and the ZIF-8 particles suspended in methanol were exchanged to DMF for three times. Films were fabricated by combining the polymer solutions with the ZIF-8 suspension. The mixtures were cast onto a glass petri dish dried under a static vacuum at 60 °C overnight and cured under a dynamic vacuum 180 °C for 18 hours.

### 3.3.4 Gas permeability measurements

Gas permeation tests of $H_2$, $N_2$, $CH_4$, $C_2H_4$, $C_2H_6$, $C_3H_6$, and $C_3H_8$ were conducted using an automated, custom-built, constant-volume, variable-pressure permeation system from Maxwell Robotics. From the prepared films, membrane coupons of roughly 1 $cm^2$ were cut and their thickness was measured five times using a micrometer to provide an average and a standard deviation. These coupons were then affixed

to a brass shim stock disk having an outer diameter of 47 mm and an inner diameter of 7 mm using impermeable 5-minute epoxy glue (Devcon, 14250).

The active permeation area was established to be between 5–20 $mm^2$ by scanning the setup and analyzing the image with ImageJ software from NIH. This process was repeated five times to ensure precision and provide an average and standard deviation. The samples were then sealed in a stainless-steel cell and held at one of five distinct temperatures (7, 20, 35, 50, 65 °C). Temperature control was managed using a PID temperature controller (Omega, CNI852-EI) and a chiller (Vevor, B0849YQMY4).

A set of protocols was implemented to guarantee a leak rate of less than 10% of the gas permeation rate. Each sample was vacuum-treated for a minimum of 8 hours (12 hours for $C_2$ gases ($C_2H_4$, $C_2H_6$) and $C_3$ gases ($C_3H_6$, $C_3H_8$)) before testing. Tests were run two to three times for each sample to calculate average values, and the calculated uncertainty was reported as the average instrumental error.

### 3.3.5 Gas sorption measurements

The gas sorption capacities of the materials for $H_2$, $N_2$, $CH_4$, $C_2H_4$, $C_2H_6$, $C_3H_6$, and $C_3H_8$ were measured at the same five temperature points (7, 20, 35, 50, 65 °C) for both the 30 wt% MMMs and the pure polymer membrane. All measurements were conducted using an automated pressure decay method, facilitated by a dual volume and dual transducer sorption system from Maxwell Robotics. For each test, a sample of membrane film (˜0.1 g) was loaded into the test cell. The cell was sealed, and the entire system was evacuated for at least 12 hours to remove any residual gases or moisture.

The quantity of gas sorbed by the sample at each pressure point was determined through a balance calculation performed between each dosing and equilibration phase. The sorption coefficients were determined as the secant slope of the isotherm at a given pressure, around 1 atm.

## 3.4 Results and discussion

In this study, permeabilities and sorption coefficients of pure 6FDA-DAM film, 30 wt% control ZIF-8 (CZ) MMM, and 30 wt% branched ZIF-8 (BZ) MMM were measured for seven gases, namely $H_2$, $N_2$, $CH_4$, $C_2H_4$, $C_2H_6$, $C_3H_6$, and $C_3H_8$, at five distinct temperatures (7, 20, 35, 50, 65 °C) at approximately 1 atm. The temperature range was selected based on the limitations of the instruments used, which allowed for a range between 7 and 65 °C. Further characterizations of the samples are detailed in our previously published work.[30]

Before delving into the specific gas transport behaviors, it is important to highlight that ZIF-8 is well-known for its exceptional separation capacity for propylene/propane ($C_3H_6/C_3H_8$).[26, 15, 102, 103] The high performance of ZIF-8 in this regard is largely due to an effective diffusivity "cut-off" that falls between 4.0–4.2 Å. This cut-off is noteworthy, as it is larger than the crystallographic pore aperture of 3.4 Å found in ZIF-8.[16] The mechanism behind this behavior is a phenomenon known as the "gate opening" effect, which enables the transport of molecules larger than the pore size through the rotation of the ligand's methyl groups.[74]

### 3.4.1 Temperature dependence of permeability

As discussed in our previous work, BZ MMM demonstrates stronger MOF-polymer interphase confinement, which suppresses the rotation of the ZIF-8 ligand and results in a smaller diffusion cut-off than CZ MMM. Consequently, BZ MMM exhibits superior performance in $H_2$-based separations but a reduced selectivity for $C_3$ separation. This led to a hypothesis where, we may prompt the gate-opening behavior of BZ that is otherwise suppressed by interphase confinement, similar to flipping a switch by applying energy (in this case, heat). Conversely, when subjected to low temperatures, CZ MMM might show suppressed gate-opening behavior. To confirm this hypothesis, we expected to observe a discontinuous or stepwise change in selectivity for the gas pairs—BZ MMM losing its $H_2$-based selectivity and gaining propylene/propane selectivity at high temperatures, and CZ MMM gaining $H_2$-based selectivity at lower

temperatures.

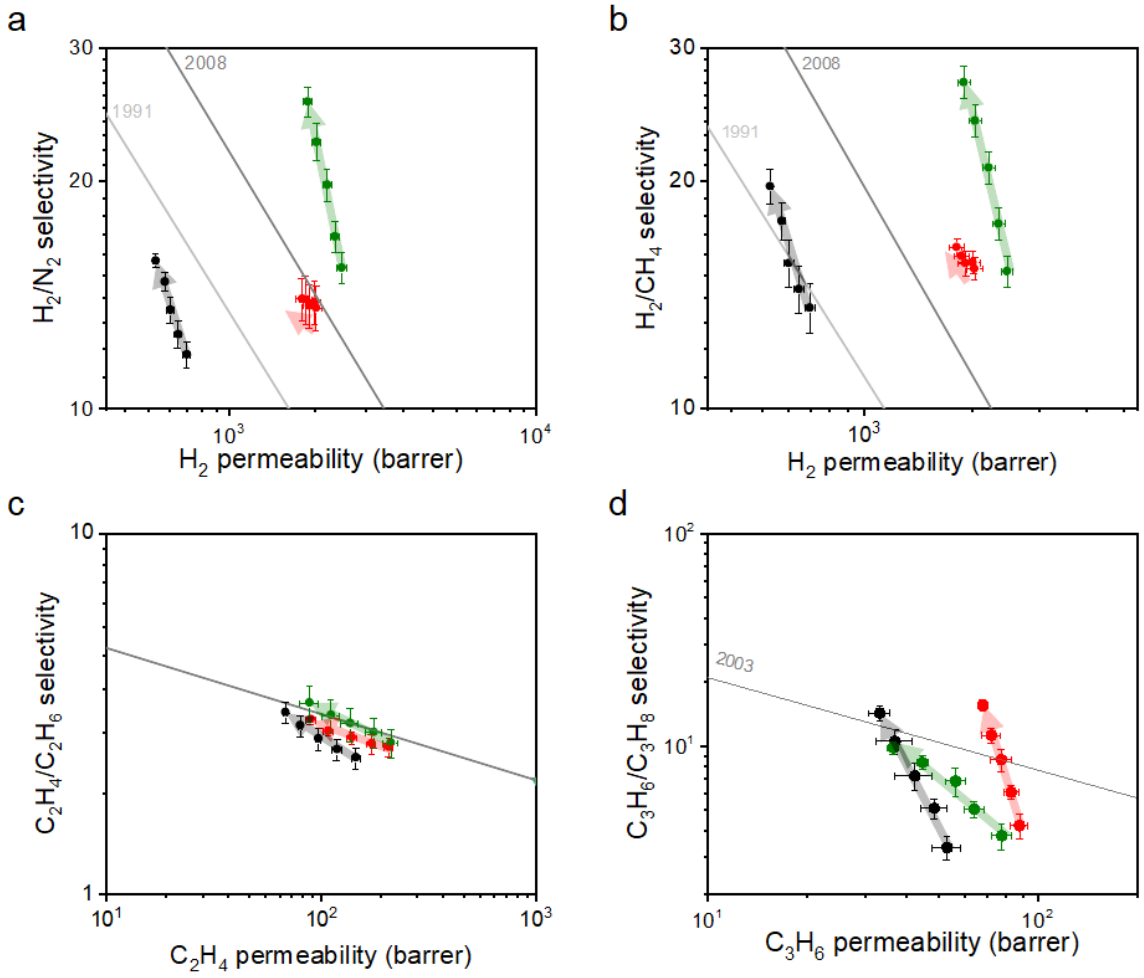


Figure 3-1: Robeson plots of a pure 6FDA-DAM polymeric film and 30 wt% CZ MMM and 30 wt% BZ MMMs with various temperatures (7, 20, 35, 50, and 65 °C) for (a) $H_2/N_2$ separation, (b) $H_2/CH_4$ separation, (c) ethylene/ethane separation, and (d) propylene/propane separation. The upper bounds for all gas pairs are also included in the plots.[17, 18, 19, 20] Arrows represent decrease in temperature.

As shown in Fig 3-1, a dramatic enhancement in $H_2$-based selectivity with BZ MMM at decreasing temperatures was observed when compared to CZ MMM. The high-temperature points of both MMMs converge as the slope of BZ MMM is steeper. For $C_2$ separations, there was no significant difference in temperature dependence observed between the samples. In contrast, for $C_3$ separations, CZ MMM showed a more pronounced performance boost as the temperature decreased compared to BZ MMM. Interestingly, as the temperature increased, the separation performances of

CZ MMM and BZ MMM also converged.

These results align with our hypothesis that temperature can influence gate-opening behavior. However, the change appears to be continuous rather than binary, operating more like a volume knob than a switch. If we extrapolate this trend, exposing both MMMs to even higher temperatures might lead to increasingly similar separation behaviors.

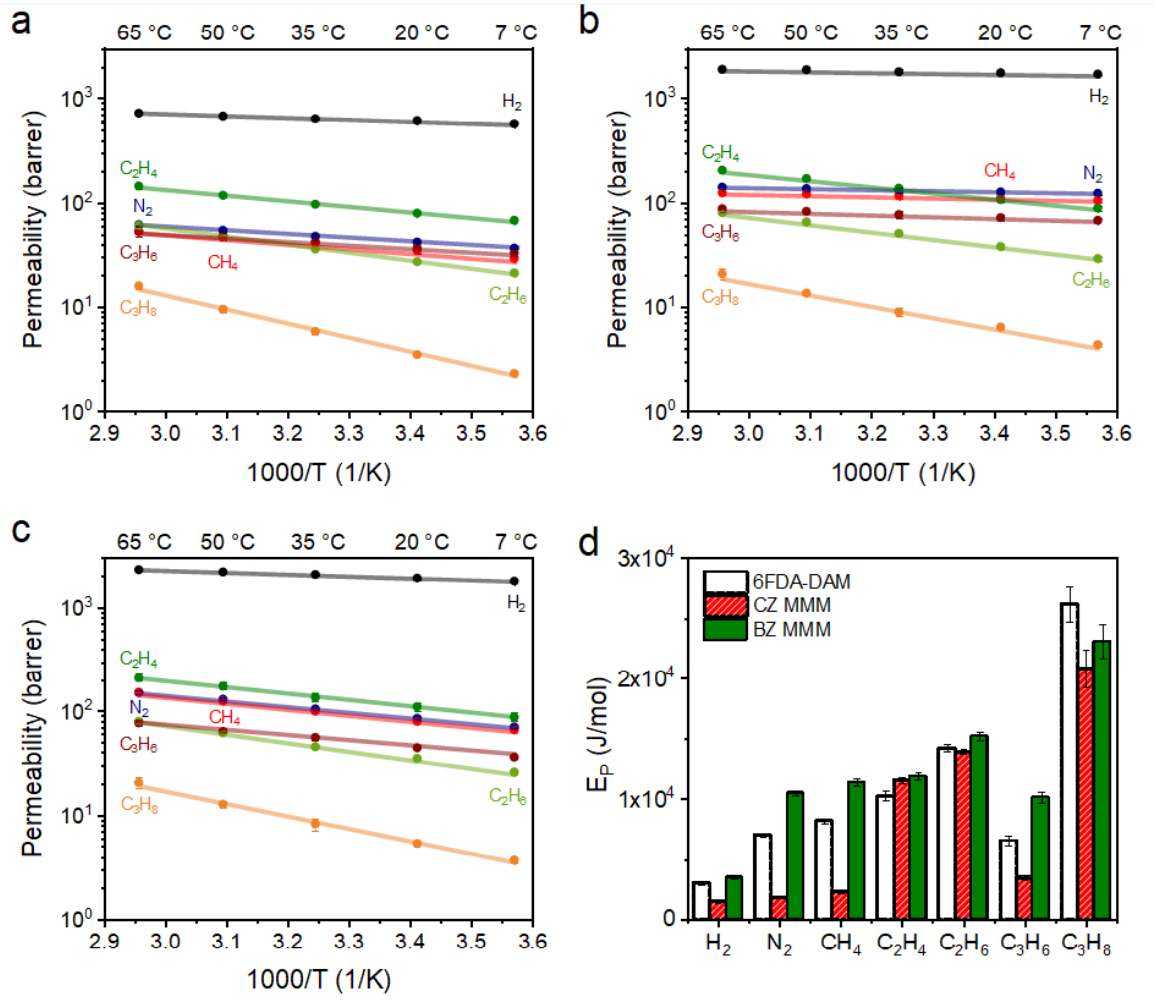


Figure 3-2: Logarithmic permeability of evaluated gases ($H_2$, $N_2$, $CH_4$, $C_2H_4$, $C_2H_6$, $C_3H_6$, and $C_3H_8$) plotted against inverse temperature for (a) 6FDA-DAM, (b) 30 wt% CZ MMM, and (c) 30 wt% BZ MMM. Each point indicates a measured data point, and each line signifies a linear fit for each gas across five temperatures. Comparative analysis of activation energy of permeation is presented in (d).

For a more detailed view, Fig 3-2 presents a linear fit of the permeability of the seven gases versus inverse absolute temperature for 6FDA-DAM, BZ MMM, and

CZ MMM. Consistent with earlier reports on polymeric membranes,[104, 105, 106], the gas permeability of all samples increases with temperature. The permeabilities followed an Arrhenius relationship where logarithmic permeability linearly correlates with inverse temperature, as shown in Fig 3-2. The permeation activation energies calculated for $H_2$, $N_2$, $CH_4$, $C_2H_4$, $C_2H_6$, $C_3H_6$, and $C_3H_8$ of the three samples using Equation 3.6 are tabulated in Table 3.11. Permeation activation energy generally increases with the penetrant size (Table 3.22), further demonstrating the strong size-sieving property.

Table 3.1: Effective permeation activation energy of evaluated gases ($H_2$, $N_2$, $CH_4$, $C_2H_4$, $C_2H_6$, $C_3H_6$, and $C_3H_8$) measured between 7 and 65°C, for 6FDA-DAM, 30 wt% CZ MMM, and 30 wt% BZ MMM.

| | $E_P$ [kJ/mol] | | | | | | |
|---|---|---|---|---|---|---|---|
| | $H_2$ | $N_2$ | $CH_4$ | $C_2H_4$ | $C_2H_6$ | $C_3H_6$ | $C_3H_8$ |
| 6FDA-DAM | 3.5 ± 0.1 | 7.0 ± 0.1 | 8.2 ± 0.2 | 10.3 ± 0.4 | 14.2 ± 0.3 | 6.6 ± 0.2 | 26.2 ± 1.0 |
| CZ MMM | 1.5 ± 0.1 | 1.8 ± 0.5 | 2.3 ± 0.1 | 11.5 ± 0.2 | 13.9 ± 0.2 | 3.5 ± 0.1 | 20.9 ± 0.9 |
| BZ MMM | 3.1 ± 0.2 | 10.5 ± 0.2 | 11.4 ± 0.3 | 11.9 ± 0.3 | 15.2 ± 0.3 | 10.1 ± 0.4 | 23.1 ± 1.0 |

Table 3.2: Critical temperature and molecular diameter (van der Waals diameter) values for the studied probe gas molecules

| | $H_2$ | $N_2$ | $CH_4$ | $C_2H_4$ | $C_2H_6$ | $C_3H_6$ | $C_3H_8$ |
|---|---|---|---|---|---|---|---|
| Critical temperature, $T_c$ (K)* | 33.2 | 126.2 | 190.6 | 282.5 | 305.3 | 365.2 | 369.9 |
| Molecular diameter, d (Å)[44] | 2.76 | 3.13 | 3.25 | 3.59 | 3.72 | 4.03 | 4.16 |

*www.NIST.gov

When comparing the MMMs, BZ MMM shows a higher activation energy of permeation for all gases. This could be indicative of the interphase confinement significantly influencing gas transport resistance. In particular, BZ MMM exhibits a substantial increase from $N_2$, while CZ MMM maintains similar $E_p$ values up to $CH_4$. The difference is relatively moderate for $C_2$ gas pairs ($C_2H_4/C_2H_6$). For $C_3$ gas pairs ($C_3H_6/C_3H_8$), CZ MMM displayed a larger $E_p$ difference than BZ MMM by showing a much smaller propylene $E_p$. These results align well with the selectivity trend in Fig 1, corroborating that the distinct gas separation performances of CZ and BZ MMMs are supported by differences in transport energetics.

Drawing direct conclusions from comparisons between the pure polymer and MMMs is more challenging, primarily because $E_p$ is a complex energetic parameter. However, considering the diffusion activation energies and the heats of sorption can provide a more nuanced understanding of the interactions between the membranes and the penetrant. The activation energy for permeation ($E_p$) can be conceptualized as the sum of a thermodynamic parameter (heat of sorption, $\Delta H_s$) and a kinetic parameter (activation energy for diffusion, $E_d$), as described in the Equation 3.7. As temperature rises, so do diffusion coefficients, given the positive diffusion activation energies. Conversely, sorption coefficients decrease due to the typically negative sorption enthalpy.[99] The change in diffusion coefficients usually outweighs the change in sorption coefficients, leading to a net increase in permeability,[107, 108] which was also observed in this study. As $E_p$ is a lumped value, individual analysis of sorption and diffusion processes can provide a more comprehensive understanding of the temperature dependence of permeation for a particular penetrant. A more detailed discussion on the temperature dependence of diffusion and sorption coefficients will be presented in the following sections.

### 3.4.2 Temperature dependence of sorption coefficients

Fig 3-3 presents a linear fit of the sorption coefficient of seven gases against inverse absolute temperature for 6FDA-DAM, BZ MMM, and CZ MMM. The sorption coefficients (S = C/p) were calculated as the secant slope of the isotherm at a specific pressure (~1 atm). The temperature dependence of sorption coefficients is described by the van't Hoff relationships, as shown in Equation 5, and the corresponding apparent heat of sorption values are compiled in Table 3.3. As anticipated, sorption coefficients for all gases decrease with increasing temperature, resulting in a negative heat of sorption.

The heat of sorption is a summation of two energy contributions: the first component represents the exothermic enthalpy change when a gas molecule transitions from the gaseous phase into a more stabilized, liquid-like sorbed state.[109] This enthalpy shift is largely determined by the condensability of gas, or the molecule's propen-

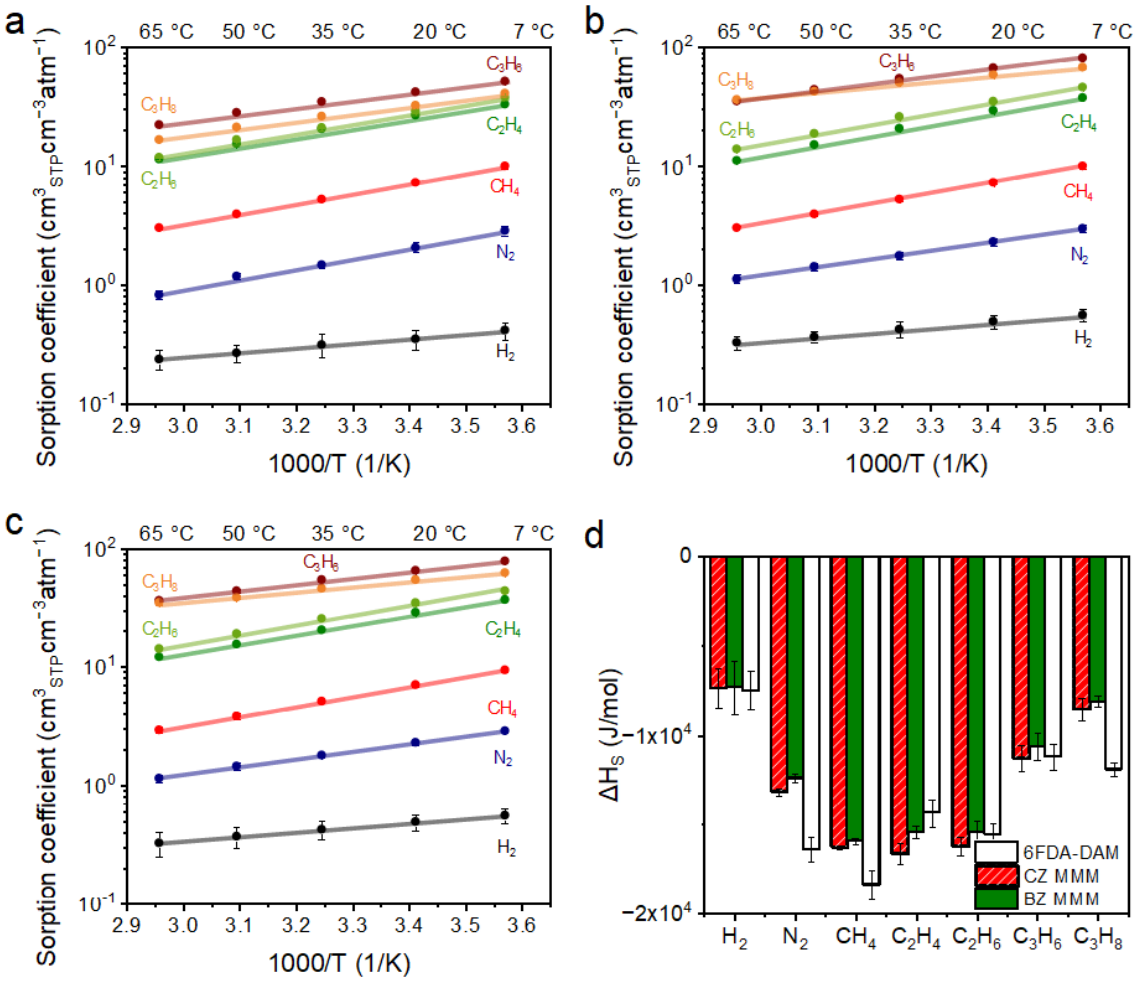


Figure 3-3: Logarithmic sorption coefficient of evaluated gases ($H_2$, $N_2$, $CH_4$, $C_2H_4$, $C_2H_6$, $C_3H_6$, and $C_3H_8$) plotted against inverse temperature for (a) 6FDA-DAM, (b) 30 wt% CZ MMM, and (c) 30 wt% BZ MMM. Each point indicates a measured data point, and each line signifies a linear fit for each gas across five temperatures. Comparative analysis of enthalpy of sorption is presented in (d).

sity to exist in the sorbed state, which can be represented by critical temperature. The second energy component represents the energy penalty from the formation of a sorption site and the energy involved in mixing the sorbed molecule with the newly created site.[110, 111] For $H_2$, $N_2$, and $CH_4$, the first component seems to play a crucial role, where the absolute value of sorption enthalpy increases in the order of $T_c$ increase (Table 3.2).However, from ethylene onwards, the second component begins to influence the values, resulting in a decrease in an irregular manner.

Nevertheless, the differences in sorption enthalpy among the MMM samples were

Table 3.3: Sorption enthalpy of evaluated gases ($H_2$, $N_2$, $CH_4$, $C_2H_4$, $C_2H_6$, $C_3H_6$, and $C_3H_8$) measured between 7 and 65°C, for 6FDA-DAM, 30 wt% CZ MMM, and 30 wt% BZ MMM.

| | $\Delta H_S$ [−kJ/mol] | | | | | | |
|---|---|---|---|---|---|---|---|
| | $H_2$ | $N_2$ | $CH_4$ | $C_2H_4$ | $C_2H_6$ | $C_3H_6$ | $C_3H_8$ |
| 6FDA-DAM | 7.5 ± 0.3 | 16.4 ± 0.7 | 18.4 ± 0.8 | 14.4 ± 0.8 | 15.5 ± 0.6 | 11.2 ± 0.5 | 11.9 ± 0.4 |
| CZ MMM | 7.4 ± 0.2 | 13.2 ± 0.2 | 16.3 ± 0.1 | 16.6 ± 0.6 | 16.2 ± 0.5 | 11.3 ± 0.4 | 8.5 ± 0.3 |
| BZ MMM | 7.3 ± 0.1 | 12.4 ± 0.2 | 15.9 ± 0.2 | 15.4 ± 0.4 | 15.4 ± 0.6 | 10.6 ± 0.5 | 8.1 ± 0.3 |

only moderate (Table 3.3), with BZ MMM consistently displaying smaller absolute values of sorption enthalpy. This suggests that gas interactions with CZ may be marginally stronger than with BZ in polymer matrix. Similar values across MMMs indicate that diffusion selectivity is the prevailing factor contributing to overall permselectivity trends.

### 3.4.3 Temperature dependence of diffusion coefficients

Fig 3-4 presents a linear fit of the diffusion coefficient of seven gases against inverse absolute temperature for 6FDA-DAM, BZ MMM, and CZ MMM. Much like permeability, the temperature dependence of diffusion coefficients follows an Arrhenius relationship (Equation 3.4). The corresponding diffusion activation energies are provided in Table 3.4. Diffusion coefficients increase with temperature, illustrating a positive activation energy of diffusion, which represents the minimum energy required for a penetrant to make a diffusive leap from one equilibrium site to another is positive. Larger penetrants typically necessitate higher diffusion activation energies to facilitate their passage through the size-discriminating pores that are responsible for diffusion selectivity.[99] As temperature increases, large-scale motions substantially boost the diffusivity of relatively large molecules by creating gaps in the polymer chains through which these molecules can traverse.[101] Similar to this, flexible ZIF-8 ligand seems to be also activated with increasing temperature.

BZ MMM exhibited higher diffusion activation energies ($E_D$ values, except for $C_2H_4$ where it is in the error margin with CZ MMM) compared to CZ MMM due to stronger MOF–polymer confinement. Comparing Table 3.3 and Table 3.4, diffusion

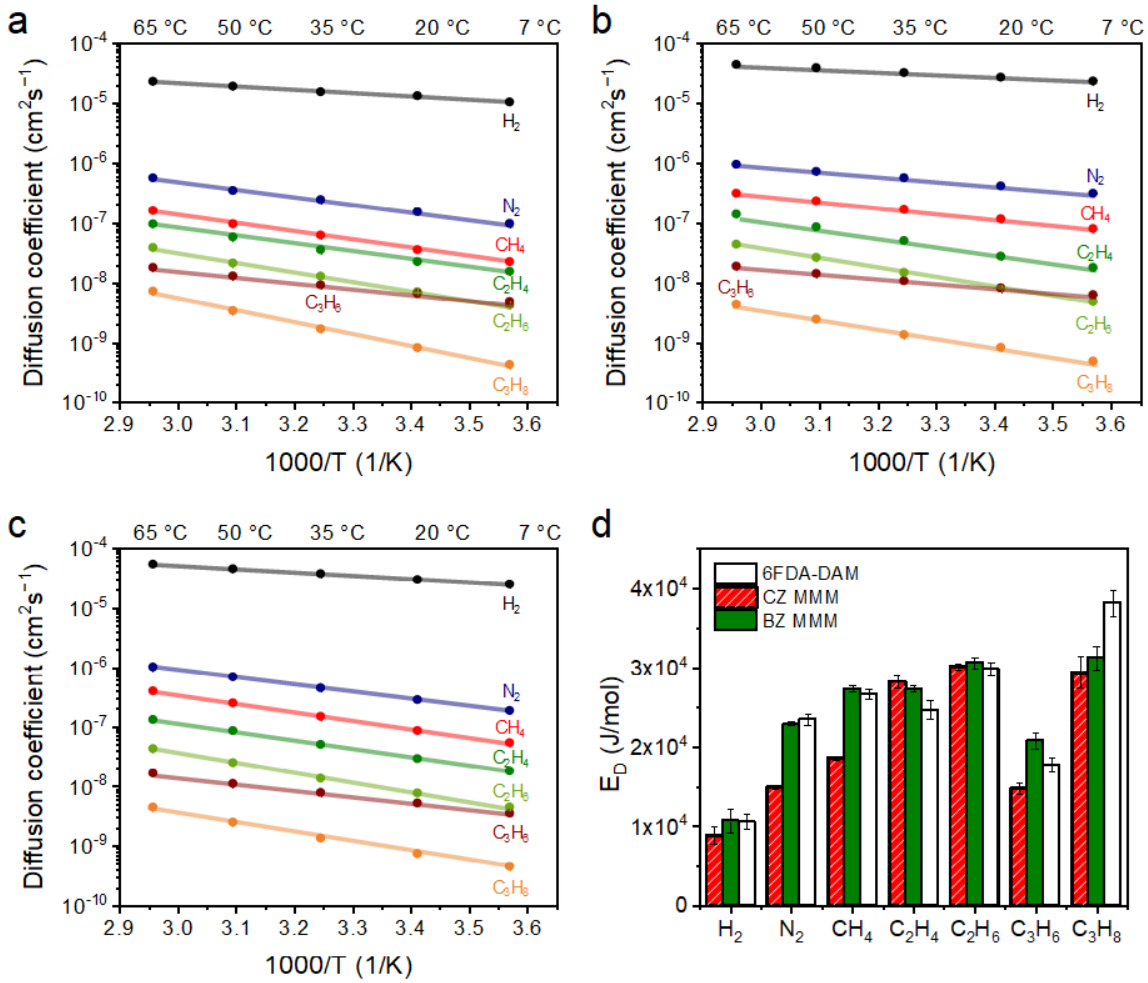


Figure 3-4: Logarithmic diffusion coefficient of evaluated gases ($H_2$, $N_2$, $CH_4$, $C_2H_4$, $C_2H_6$, $C_3H_6$, and $C_3H_8$) plotted against inverse temperature for (a) 6FDA-DAM, (b) 30 wt% CZ MMM, and (c) 30 wt% BZ MMM. Each point indicates a measured data point, and each line signifies a linear fit for each gas across five temperatures. Comparative analysis of activation energy of diffusion is presented in (d).

activation energy does indeed surpass the heat of sorption, exerting a more substantial influence on the permeation activation energy, as noted earlier. It's worth mentioning that the permeability increase is lower than that of diffusivity, this is due to the decreasing trend of the sorption coefficient (negative heat of sorption).

### 3.4.4 Selectivity considerations

Permselectivity ($\alpha_{i/j}$) and sorption selectivity ($S_i/S_j$) were determined using the permeation and sorption measurements, respectively, while diffusion selectivity ($D_i/D_j$)

Table 3.4: Table 4. Effective diffusion activation energy of evaluated gases ($H_2$, $N_2$, $CH_4$, $C_2H_4$, $C_2H_6$, $C_3H_6$, and $C_3H_8$) measured between 7 and 65°C, for 6FDA-DAM, 30 wt% CZ MMM, and 30 wt% BZ MMM.

| | $E_D$ [kJ/mol] | | | | | | |
|---|---|---|---|---|---|---|---|
| | $H_2$ | $N_2$ | $CH_4$ | $C_2H_4$ | $C_2H_6$ | $C_3H_6$ | $C_3H_8$ |
| 6FDA-DAM | 10.6 ± 0.4 | 23.4 ± 0.7 | 26.6 ± 0.7 | 24.6 ± 1.2 | 29.8 ± 0.9 | 17.7 ± 0.5 | 38.1 ± 1.3 |
| CZ MMM | 8.9 ± 0.2 | 15.0 ± 0.2 | 18.6 ± 0.2 | 28.2 ± 0.8 | 30.1 ± 0.4 | 14.8 ± 0.4 | 29.4 ± 0.1 |
| BZ MMM | 10.7 ± 0.2 | 22.9 ± 0.2 | 27.3 ± 0.5 | 27.3 ± 0.4 | 30.6 ± 0.7 | 20.7 ± 0.4 | 31.2 ± 1.0 |

was calculated using Equation 2. As shown in Fig 5,for hydrogen separations, diffusion selectivity contributes predominantly to the overall permselectivity, as sorption selectivity values are less than unity due to the low sorption of $H_2$ compared to other gases. In addition to the values being small, the temperature-induced change in sorption selectivity was much smaller than that of diffusion selectivity.

Comparing $H_2$-based separations for MMMs, diffusion selectivity of CZ MMM has less temperature dependence than 6FDA-DAM and BZ MMM due to the smaller diffusion activation energy ($E_D$) for $N_2$ and $CH_4$. This may suggest that CZ enables the diffusion of $N_2$ and $CH_4$ through the MOF phase with a minimal energy barrier that is less affected by temperature change due to the gate opening behavior, which is likely happen even at the lowest temperature tested (7 °C). When temperature increases, diffusion selectivity becomes very similar, implying a more opened gate for BZ MMM. Conversely, at lower temperatures, larger gases seem to pass through CZ MMM more easily, while the ligand rotation confinement in BZ MMM increases transport resistance for $N_2$ and $CH_4$. However, inferred from continuous change in diffusion selectivity of BZ MMM, the influence of the interphase confinement to gas transport is not a clear open-close process, but rather a continuous spectrum of change over five temperature points.

A similar trend is observed for $C_2$ gases, where at high temperatures, CZ and BZ MMM behave similarly, while the diffusion selectivity of BZ MMM increases more rapidly with decreasing temperature. However, this trend is observed to happen in a much lesser extent, which could be due to the smaller size difference of $C_2$ gases.

For $C_3$ gases, a similar behavior is observed at high temperatures, converging of diffusion selectivity of BZ MMM and CZ MMM. However, in this case, the diffusion

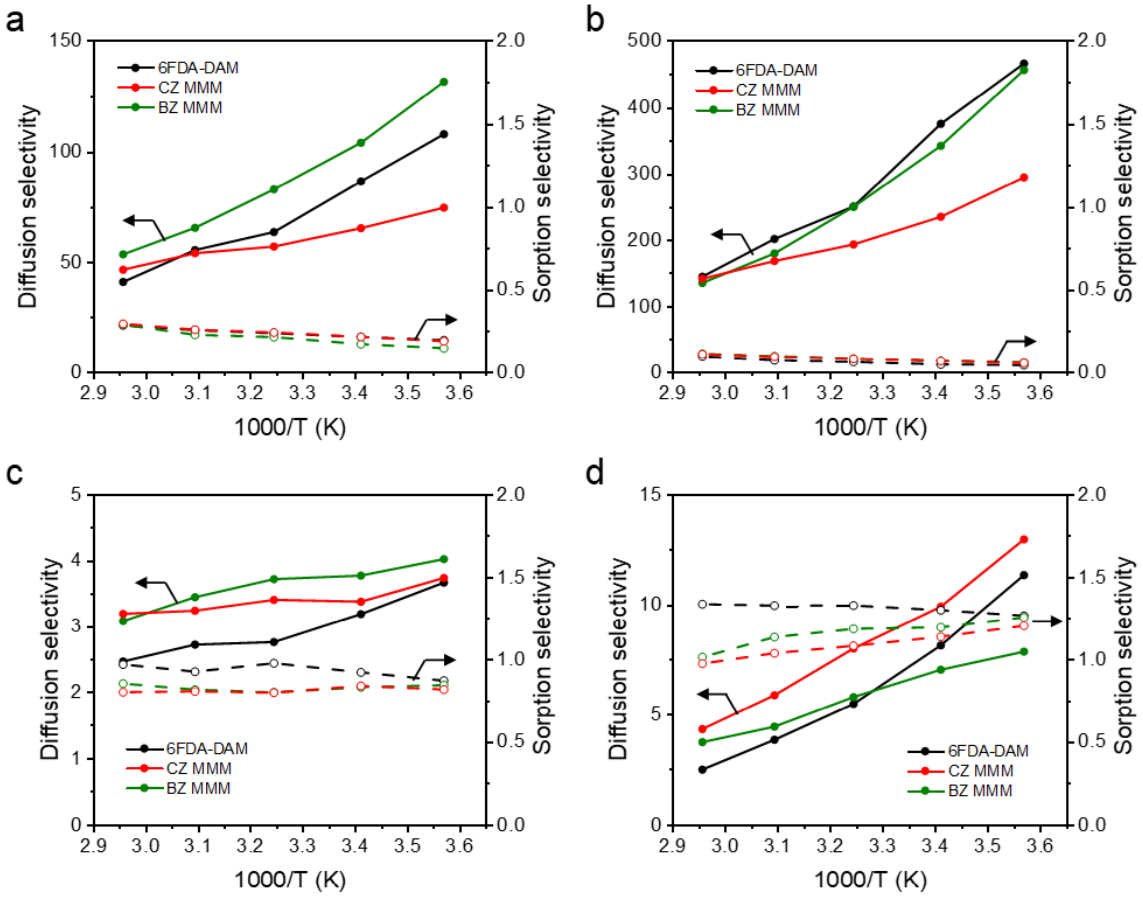


Figure 3-5: Diffusion and sorption selectivity over the range of five temperatures of 6FDA-DAM, 30 wt% CZ MMM, and 30 wt% BZ MMM for (a) $H_2/N_2$, (b) $H_2/CH_4$, (c) $C_2H_4/C_2H_6$, and (d) $C_3H_6/C_3H_8$ separations. Filled dots with solid lines illustrate diffusion selectivity and open dots with dashed lines display sorption selectivity.

selectivity of CZ MMM increases more rapidly with decreasing temperature. This suggests that the confined pore flexibility in BZ MMM negatively affects the diffusion of both propylene and propane, whereas CZ MMM, which still possesses gate-opening behavior, can allow propylene, but not propane, to pass through.

## 3.5 Conclusion

A comprehensive investigation into the temperature-dependent permeation, diffusion, and sorption of BZ and CZ MMMs was conducted. The findings highlighted the significant influence of temperature on the gate-opening behavior of ZIF-8 in BZ MMM.

As temperatures increase, the separation behavior of BZ MMMs tends to align more closely with CZ MMMs. However, this transition (or gate-opening) occurs continuously rather than acting as a discrete switch, leading to a consistent variation in selectivity with temperature changes. In-depth analyses of both diffusion and sorption processes revealed contrasting temperature dependencies, with diffusion effects generally outweighing those of sorption. Collectively, our findings broaden the understanding of temperature-dependent properties in mixed matrix membranes, particularly those incorporating highly flexible MOFs. This opens new pathways to optimize and finely control gas separation performance through temperature modulation in these membrane systems.

# Chapter 4

# Facet-Specific Gas Transport Properties of Metal-Organic Framework in Polymer Nanocomposite

## 4.1 Abstract

Metal–Organic Frameworks (MOFs) hold significant potential for various applications in gas, liquid, and ion processing and purification. Significant efforts on MOF nanoparticles underscore the importance of understanding their facet termination.While MOF-based nanocomposite research is growing, facet-specific studies on molecular transport are rare. Here, a pioneering investigation into facet-specific gas transport in nanocomposites was conducted using ZIF-8, with exposed {110} or {100} facets interacting with a polyimide. Despite their similar properties as MOFs, the {100} facet showed more significant MOF–polymer interactions as more angled apertures enable stronger binding with the polymer, corroborated by DFT calculations. This leads to unique gas transport trend: the {110} facet promotes propylene/propane separations, while the {100} facet enhances hydrogen-based ($H_2/N_2$, $CH_4$) and ethy-

lene/ethane separation, particularly at subambient temperatures mainly by diffusion selection. This study provides insights into gas transport and interaction in MOF composites, enabling unique applications through engineering the MOF surface.

## 4.2 Introduction

Metal–organic frameworks (MOFs) are crystalline materials consisting of metallic nodes interconnected by organic linkers with a regular and porous structure.[112, 113] Notably, frameworks offers versatility, presenting a nearly unlimited array of possibilities for applications in materials science and engineering.[93, 40, 63] Among the MOF family, zeolitic imidazolate frameworks (ZIFs) stand out, with ZIF-8 being one of the most widely studied examples.[114, 115, 116] ZIF-8, consisting of $Zn^{2+}$ ions and 2-methylimidazolate linkers, possesses excellent chemical and thermal stability, making it highly suitable for diverse applications such as separations, adsorption, and catalysis.[27, 67]

In these applications where smaller nanoscale MOF particles are favored due to enhanced dispersion and reduced mass transfer resistance, the interaction between MOF surfaces and molecules becomes crucial because of their large surface-to-volume ratio.[117] Interestingly, despite the same bulk structure, different MOF facets display unique characteristics in catalysis,[118, 119] sorption,[120, 121] and separation.[122] For instance, Mao et al. showed that preferentially oriented HKUST-1 films with {100} and {111} facets showed different pore sizes impacting $CO_2/SF_6$ separation,[123] and Pang et al. showed that the {110} facet of ZIF-8, though thermodynamically more stable, exhibited lower acid resistance than the {100} facet.[124] The results from these studies imply that specific facets can be leveraged to optimize desirable features for target applications.

On the other hand, there has been a lack of facet-specific studies in MOF nanocomposites, despite significant advancements in MOF hybridization with other materials.[125, 126] The hybridization of materials is gaining traction because it can significantly improve key features such as stability, transport, and conductivity.[127, 128, 129] For

example, in the context of gas separations, mixed-matrix membranes (MMMs) where the MOFs are embedded into a continuous polymer matrix, represents a promising strategy for leveraging the industrial-scale processability of polymers and the superior molecular sieving performance of MOFs.[67, 130]

Herein, we reveal an unprecedented, comprehensive investigation into the facet-specific gas transport properties of MOFs in MMMs. Our study uncovers intriguing differences in molecular separation when incorporating two different facet-terminated ZIF-8s ({110} and {100}) into the 6FDA-DAM polymer matrix. This result is unexpected, as ZIF-8 is isotropic (sod topology) with identical gas-accessible pores (6 membered ring, 6MR).[115] Initially, we confirmed similar physicochemical and gas-sorbing characteristics among two different facet-terminated ZIF-8 pure MOF particles. However, once prepared into MMM composites, the MOF–polymer interaction was stronger for the {100} facet, as suggested by both experiments and density functional theory (DFT) calculations. With this difference, it was observed that {100} facet-terminated particles considerably augment separation performance for smaller gas separations ($H_2$-based and ethylene/ethane) in an MMM environment, whereas {110} facet-terminated particles show typical findings for the well-known propylene/propane separation performance of ZIF-8. The gas transport behavior across MMMs were thoroughly analyzed, varying MOF loadings and temperatures, which revealed a distinct activation energy of diffusion for MOFs of identical chemical structures, but unique facet terminations. These findings highlight how the surface characteristics of a MOF are a crucial and under-explored area of study for tuning MOF properties in separation performance of MMMs.

## 4.3 Materials and Methods

### Materials

Methanol (HPLC, $\geq$ 99.9%), *N,N*-dimethylformamide (DMF, HPLC, $\geq$ 99.9%), zinc nitrate hexahydrate (purum p.a., crystallized, $\geq$ 99.0%), 2-methylimidazole (99%), Hexadecyltrimethylammonium bromide (CTAB, $\geq$ 99%) were purchased from

Sigma-Aldrich and used as received. The $H_2$ (HY UHP300, 99.999%), $CH_4$ (ME UHP300, 99.99%), $N_2$ (NI UHP300, 99.999%), $O_2$ (OX UHP300, 99.994%), $C_2H_4$, (EY UHP200, 99.9%), $C_2H_6$ (ET UHP300, 99.9%), $C_3H_6$ (PP P350, 99.5%), $C_3H_8$ (PR CP350, 99.0%) gas cylinders were purchased from Airgas. 6FDA-DAM (Batch: ZL11-137. MW: ~283 kDa, PDI: ~2.69) was purchased from Akron Polymer Systems and used as received. Acetic-d3 acid-d for NMR (99.5 atom%) was purchased from Acros Organics.

### 4.3.1 Preparation of ZIF-8 particles and corresponding MMMs

**Synthesis of ZIF-8 Particles**

**Rhombic Dodecahedra ZIF-8 (RDZ)** was synthesized utilizing a modified version of the method described by Lee et al.[30] To start, Zinc nitrate hexahydrate (0.5 g, 1.68 mmol) was dissolved in 20 mL of methanol, while 2-methylimidazole (0.5 g, 6.09 mmol) was separately dissolved in 20 mL of methanol. Both solutions were bath sonicated for 10 minutes. The organic ligand solution was then poured into the metal solution, and this combined solution was stirred at a rate of 600 rpm at room temperature for 1 hour. After stirring, the nanoparticles were washed thrice with fresh methanol, and a centrifuge was used to remove any unreacted species. After each centrifugation cycle (operated at 11,000 rpm for 20 minutes at 25 °C), the supernatant was discarded and replaced with fresh methanol. To achieve redispersion of the solution, a high-speed vortex was used for 1–3 minutes, followed by bath-sonication for 1 minute, and a shaker was employed for over 2 hours at a rate of 300 rpm.

**Cubic ZIF-8 (CubZ)** was synthesized using a modified procedure derived from Pang et al.[124] Initially, zinc nitrate hexahydrate (0.35 g, 1.18 mmol) was dissolved in 20 mL of deionized water. Concurrently, 2-methylimidazole (4.8 g, 58.47 mmol) along with hexadecyltrimethylammonium bromide (8 mg, 21.95 $\mu$mol) were dissolved in 60 mL of deionized water. Both solutions were dissolved by applying bath sonication for 10 minutes. The ligand solution was then poured into the metal solution to form a mixture, which was stirred at 600 rpm at room temperature for 3 minutes. Following

the stirring process, the mixture was transferred to an autoclave and placed in a pre-heated convection oven at 120 °C for 6 hours. After the mixture cooled down to room temperature, the nanoparticles were washed using the same procedure as employed for RDZ. It is worth noting that even though a modulator (CTAB) was used in the synthesis of CubZ, the residual CTAB accounted for less than 1 mol%, as revealed by digestion NMR (Figure 4-2).

**Fabrication of Mixed-Matrix Membranes**

The preparation of the polymer solution and the ZIF-8 solution were conducted separately. Firstly, 6FDA-DAM polymer was dissolved in DMF solvent and stirred for approximately 2 hours until a homogenous suspension was achieved. Concurrently, ZIF-8 particles were maintained in solution to ensure uniform dispersion prior to their integration with the polymer solution. The ZIF-8 suspension underwent solvent exchange from methanol to DMF through a series of three centrifugations and washing processes.

The fabrication of the desired ZIF-8 weight loadings in mixed matrix membranes (MMMs) was achieved by determining the concentration of ZIF-8 in the solvent-exchanged suspension using Thermogravimetric Analysis (TGA). In brief, a small volume of well-dispersed suspension (100 $\mu$L) was heated in the TGA from room temperature to 300 °C at a rate of 10 °C per minute in an $N_2$ atmosphere to determine the amount of MOF particles. This process helped establish the concentration of ZIF-8 nanoparticles in a suspension.

With these concentration values, pure polymer solutions were prepared with 10, 20, 30, and 40 wt% of ZIF-8 for the MMMs. Polymer solutions were mixed with the MOF suspension by stirring for 1 hour and subsequently probe sonicated (Qsonica, Q500) for 60–90 seconds. The resulting mixture was poured onto a glass petri dish (soda-lime Steriplan from Duran Wheaton Kimble (DWK)) and placed in a vacuum oven (maintained at a static vacuum of 0.04 bar) at 60 °C overnight.

Subsequently, a dynamic vacuum was employed for roughly 3 hours to eliminate residual solvent. The detached membranes (with a thickness ranging between 40–60

$\mu$ m) were then annealed in a vacuum oven at 180 °C for 18 hours. Each membrane was cast at least three times to ensure reproducibility. The precise loading of the membrane was measured through TGA analysis, as detailed further in Section 4.3.2.

### 4.3.2 Characterizations of ZIF-8 particles and corresponding MMMs

**Transmission electron microscopy (TEM)**

TEM images were captured on an FEI Tecnai (G2 Spirit TWIN) digital system, operating at 120 kV. TEM sample preparation involved loading 1–3 drops of the diluted suspension in methanol on fomvar coated 400 mesh copper grid for as-synthesized pure MOF samples. This step was done before MMM preparation to confirm the facet termination and dimensions of the ZIF-8 particles.

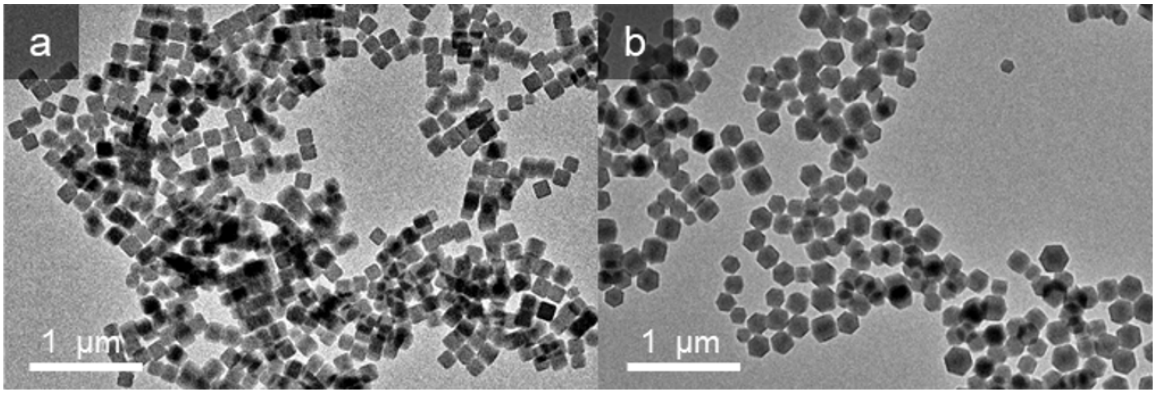


Figure 4-1: Low-magnification TEM images of (a) CubZ and (b) RDZ as-synthesized MOF particles, showing successful selective syntheses.

**MOF particle size analyses**

The particle size distribution of the MOFs was determined by analyzing a series of high-magnification TEM images using the ImageJ program. A total of 261 RDZ particles and 220 CubZ particles were measured, from which average particle dimensions and their corresponding standard deviations were obtained. Assuming ideal rhombic dodecahedron and cube morphologies for RDZ and CubZ, respectively, the average surface area and volume of each sample were calculated and are presented in Table 4.1.

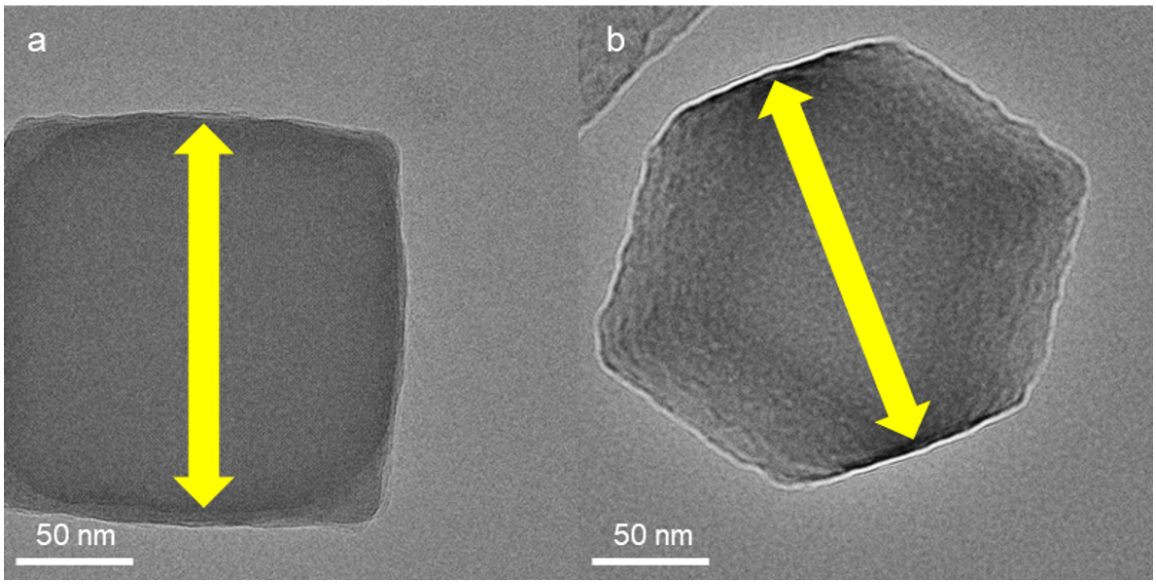


Figure 4-2: Measurement of MOF particle size, as indicated by the yellow arrows, for (a) CubZ and (b) RDZ.

Table 4.1: Average values, along with standard deviation, calculated from the measured lengths of over 200 particle counts, surface area and volume are derived from these measured dimensions.

| | CubZ | RDZ |
|---|---|---|
| Measured (yellow arrow) | 117 ± 14 nm | 139 ± 32 nm |
| Length of one edge | 117 ± 14 nm | 84.9 ± 19 nm |
| Surface area per particle | 82,600 ± 14,000 $nm^2$ | 81,500 ± 26,000 $nm^2$ |
| Volume per particle | 1,610,000 ± 330,000 $nm^3$ | 1,880,000 ± 740,000 $nm^3$ |

### Powder X-ray diffraction (PXRD)

PXRD spectra of as-synthesized MOF particles were collected on a Rigaku Smartlab Multipurpose X-ray diffractometer using Cu-K$\alpha$ radiation ($\lambda$=1.5406 Å) at a voltage of 45 kV and 200 mA and a zero-background specimen holder (UniversityWafer, Inc.). The spectra were scanned over the 5–40°.

### Brunauer-Emmett-Teller (BET) $N_2$ physisorption at 77 K

BET nitrogen physisorption isotherms were gathered using a Micromeritics 3Flex instrument, at a temperature of 77 K. Both MOF powder (Fig 4-4) and MMM film

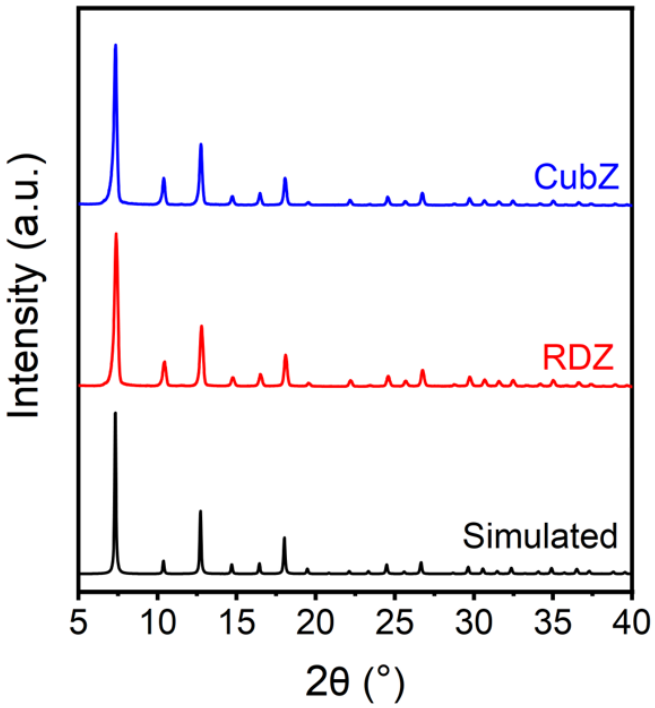


Figure 4-3: XRD patterns for CubZ and RDZ, displayed alongside a simulated ZIF-8 spectrum. All exhibited peak locations are identical across the patterns

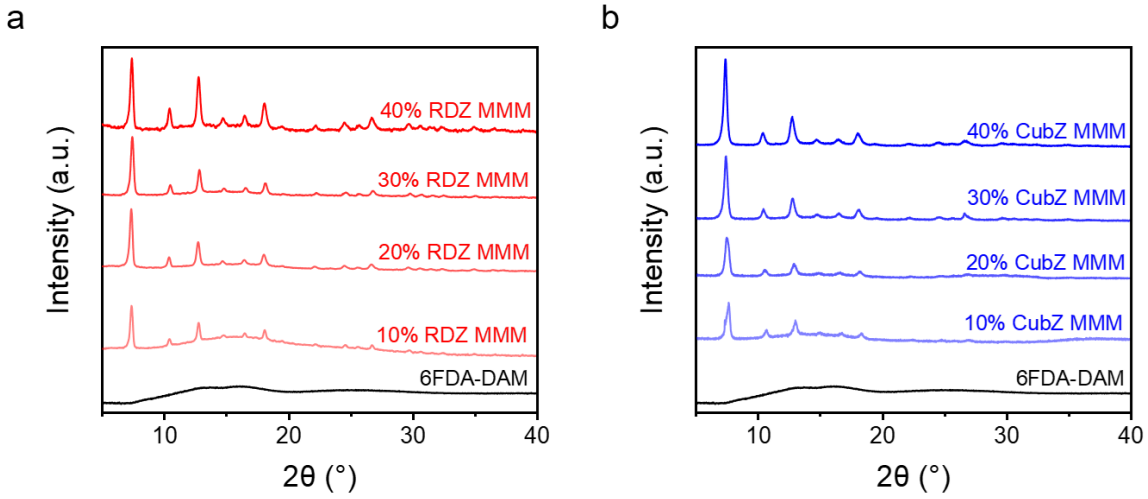


Figure 4-4: BET $N_2$ physisorption isotherms at 77 K for the as-synthesized RDZ and CubZ. Filled circles represent the adsorption process, while open circles denote the desorption process. Surface area of RDZ and CubZ is 1587 ± 21.9 and 1576 ±28.9, respectively, which were statistically identical.

samples (Figure 4-35), each weighing at least 0.1 g, were placed into pre-weighed BET tubes and subsequently degassed for 12 hours at 120 °C before each measurement,

which was conducted in a Micromeritics Smart VacPrep. The apparent surface areas were calculated using the BET method, in the relative pressure range ($P/P_0$) of 0.02–0.1, as outlined in Osterrieth, et al.[131]

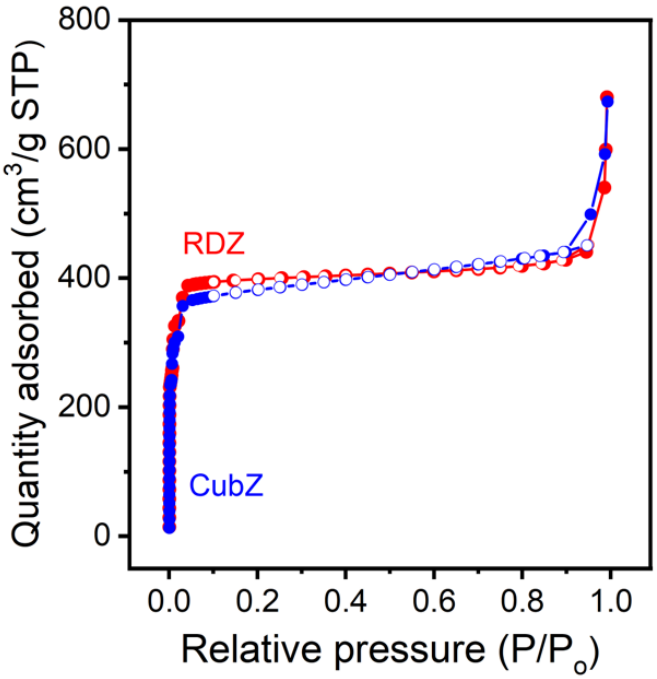


Figure 4-5: Semi-logarithmic plot of $N_2$ physisorption isotherms at 77 K for (a) 40 wt% CubZ MMM, with an inset of pure CubZ MOF powder, and (e) 40 wt% RDZ MMM, with an inset of pure RDZ MOF powder. The x-axis scales are consistent across all plots, and the y-axis of (b) is identical to that of (a). The inset y-scale corresponds to that of Figure 4-4.

**Field emission scanning electron microscope (FE-SEM)**

FE-SEM images were obtained using a Zeiss Merlin SEM operating at 3 kV. To prepare SEM cross-section samples, membranes were immersed in methanol to minimize air content and reduce the likelihood of non-uniform fracture. Subsequently, methanol-soaked samples were fractured in liquid nitrogen to achieve a uniform cross-section. Prior to imaging, the samples were sputter-coated with a 5 nm layer of gold/palladium alloy using a Desk II cold sputter unit from Denton Vacuum LLC to enable imaging of non-conductive samples by neutralizing charge effects. For Energy Dispersive X-ray Spectroscopy (EDX) analysis, the samples were left uncoated to

enhance elemental signals, and low-magnification imaging was employed to minimize electron beam damage to the sample.

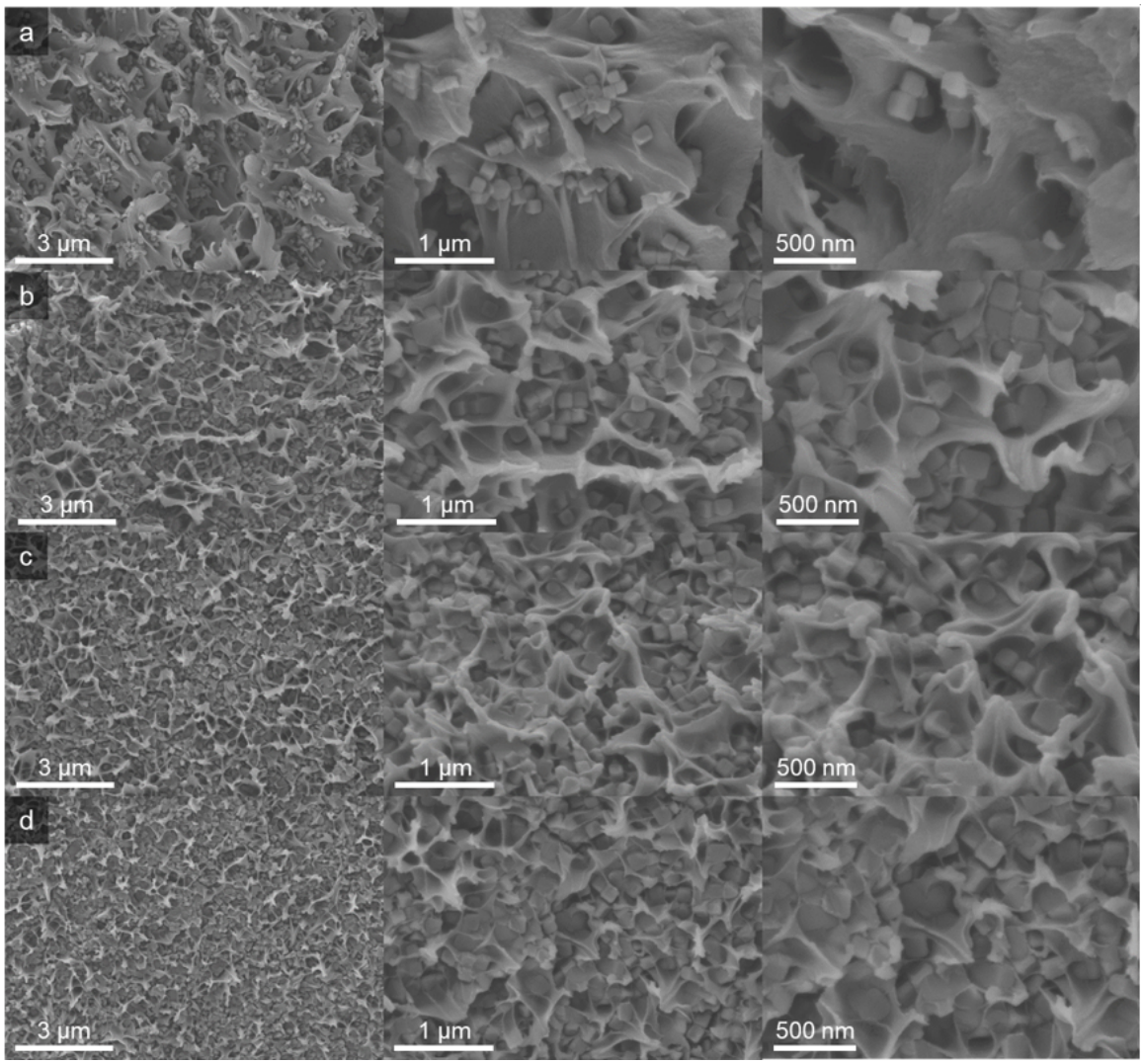


Figure 4-6: Cross-sectional SEM images with increasing levels of magnification for CubZ MMMs at (a) 10 wt%, (b) 20 wt%, (c) 30 wt%, (d) 40 wt%.

### Thermogravimetric analysis (TGA)

TGA was performed with a TA Instruments 550 Thermogravimetric Analyzer to assess as-synthesized MOF particles and the loading of the mixed matrix membranes (Fig 4-5 and Table 4.1). Heating profiles from a 50–800 °C range were collected at a rate of 10 °C per minute in air. Since the final product is pure zinc oxide, we can backtrack the original MOF quantity in the samples by comparing the final weight of

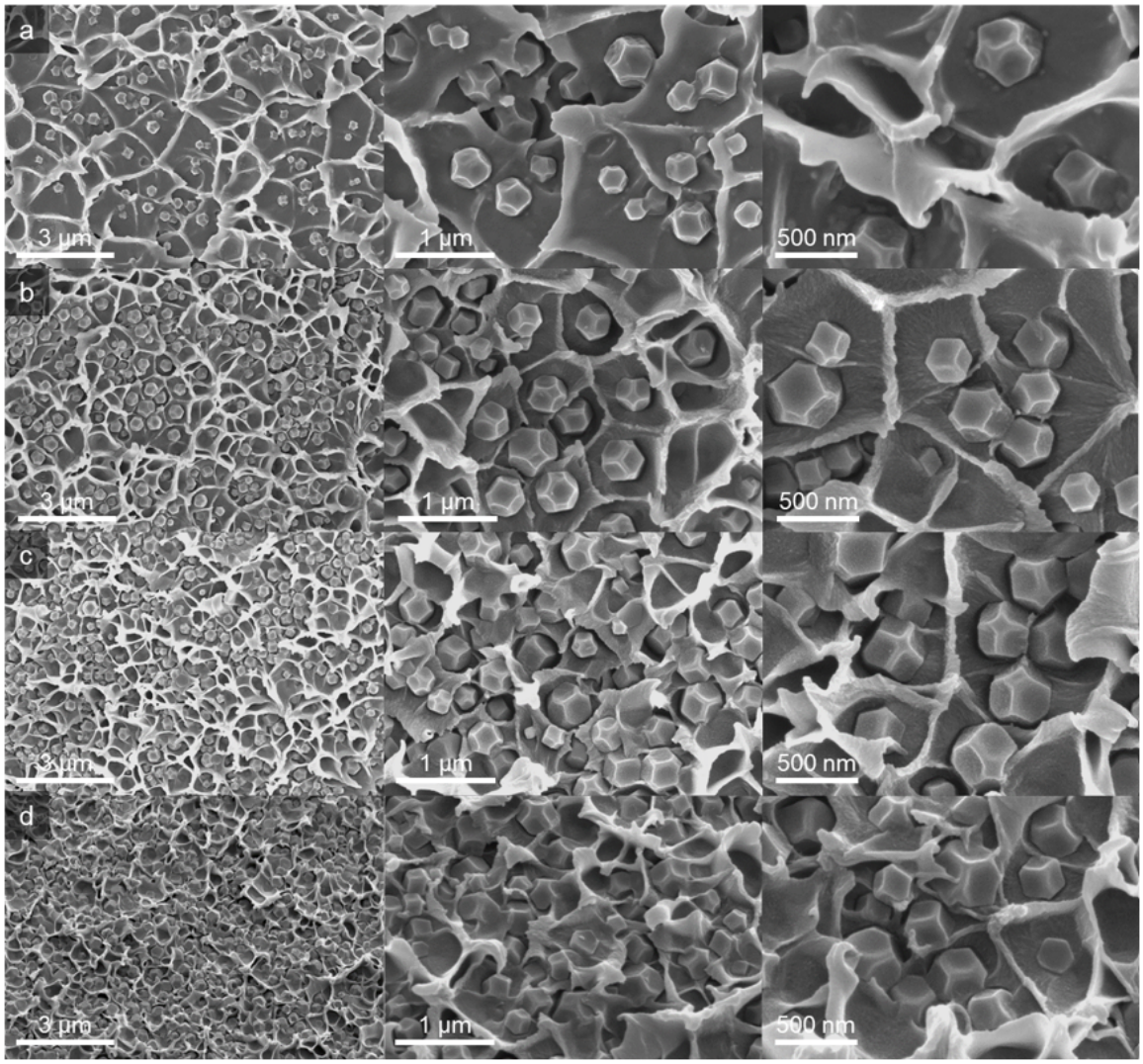


Figure 4-7: Cross-sectional SEM images with increasing levels of magnification for RDZ MMMs at (a) 10 wt%, (b) 20 wt%, (c) 30 wt%, (d) 40 wt%.

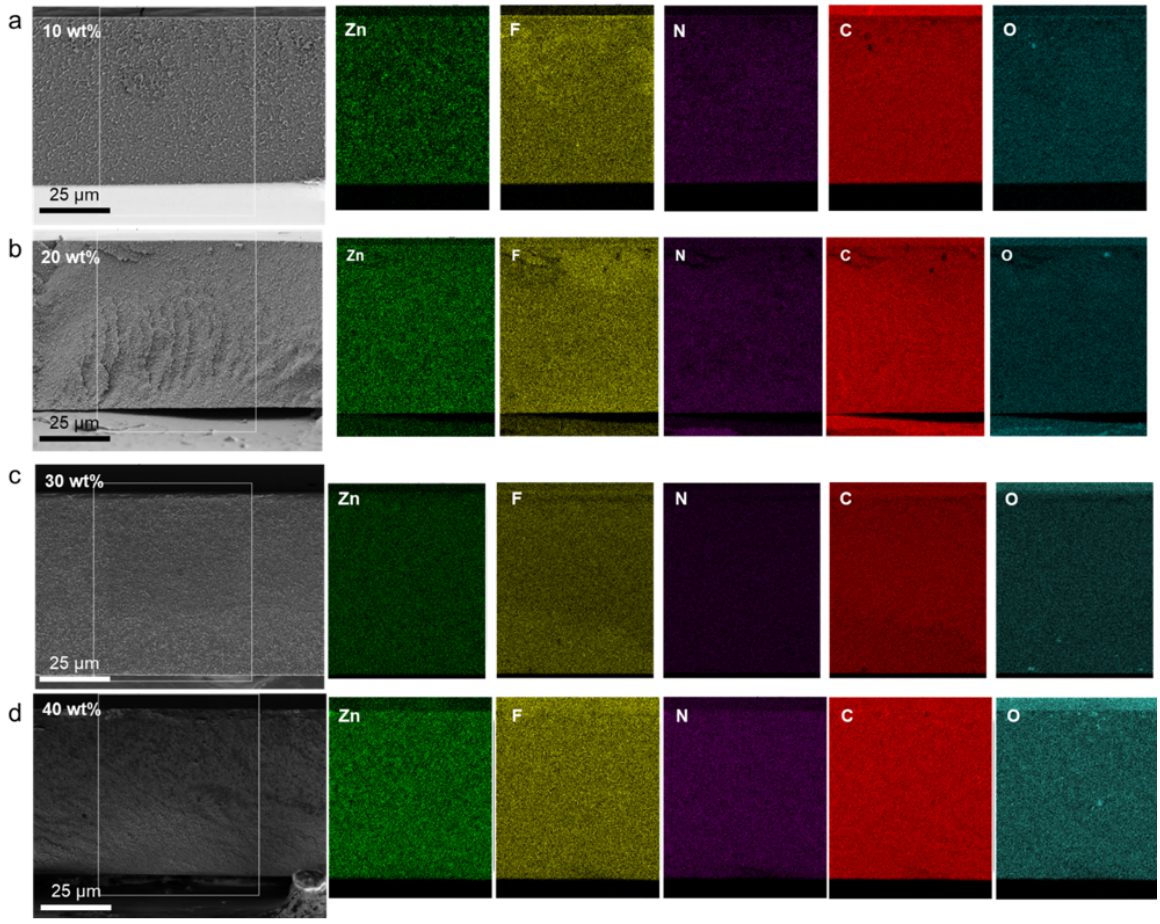


Figure 4-8: Cross-sectional SEM images showcasing the entire membrane thickness, paired with corresponding EDX analysis (Zn, F, N, C, and O). These are presented for CubZ MMMs at varying MOF loadings: (a) 10 wt%, (b) 20 wt%, (c) 30 wt%, and (d) 40 wt%.

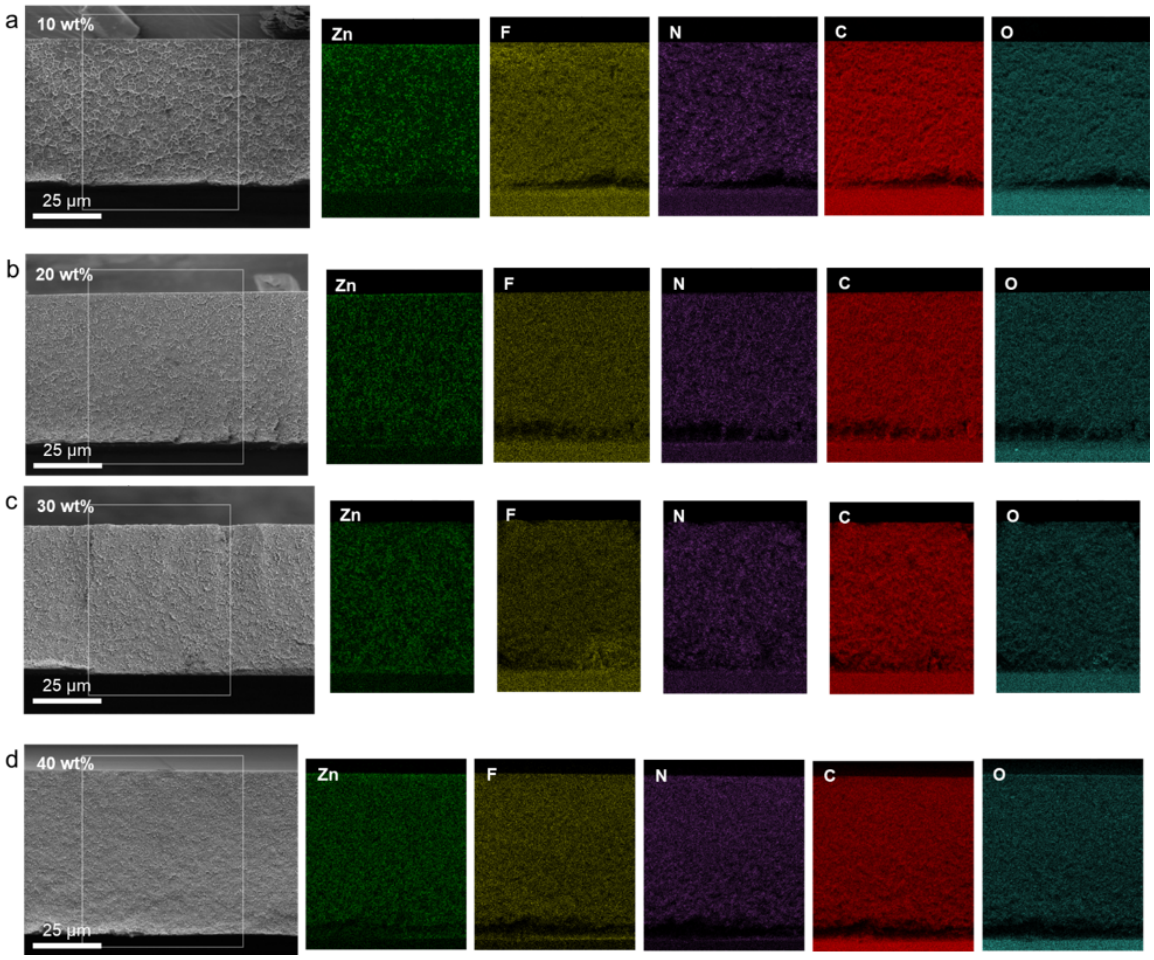


Figure 4-9: Cross-sectional SEM images showcasing the entire membrane thickness, paired with corresponding EDX analysis (Zn, F, N, C, and O). These are presented for RDZ MMMs at varying MOF loadings: (a) 10 wt%, (b) 20 wt%, (c) 30 wt%, and (d) 40 wt%.

the membranes to the final weight of pure MOF samples following the same procedure.

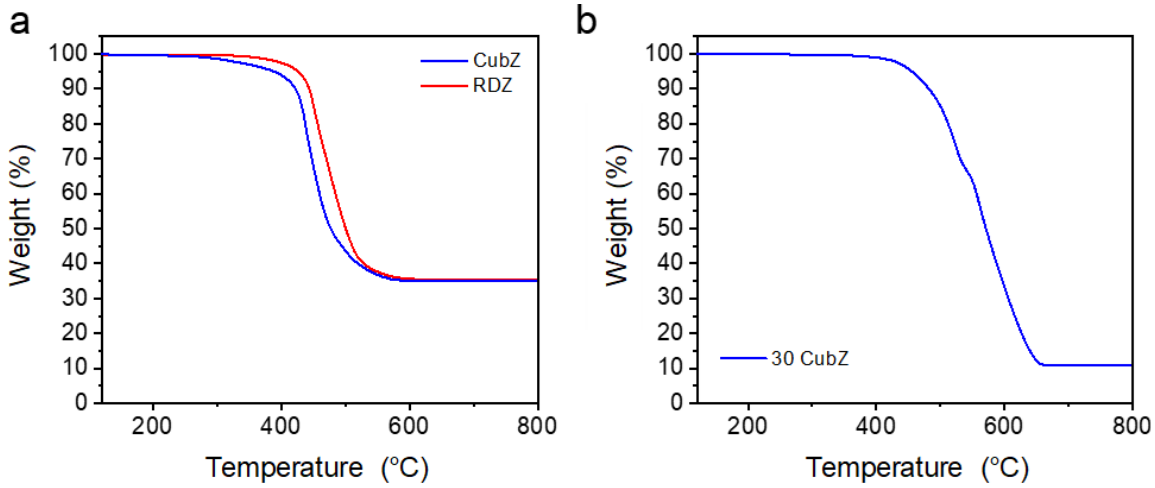


Figure 4-10: TGA calcination curves under air environment for (a) as-prepared CubZ and RDZ. The earlier downturn and lower residual in the curve of CubZ may indicate its less thermodynamically stable property compared to RDZ, and (b) 30 wt% CubZ MMMs under identical conditions. After calcination, pure ZIF-8 retained 35.4 wt%, consistent with expectations based on ZnO MW (81.38 g/mol) and ZIF-8 MW (229.6 g/mol). For the 30 wt% CubZ sample, 10.9 wt% remained, indicating a 30.75 wt% MMM composition.

Table 4.2: Before and after calcination (calc.) weights of CubZ and RDZ MMMs, and the actual loadings, calculated from these weights, are presented alongside the target loadings

| Target (wt%) | CubZ MMMs | | | RDZ MMMs | | |
|---|---|---|---|---|---|---|
| | Before calc.(mg) | After calc. (mg) | Achieved (wt%) | Before calc.(mg) | After calc. (mg) | Achieved (wt%) |
| 10 | 13.51 | 0.44 | 9.19 | 18.10 | 0.66 | 10.32 |
| 20 | 8.70 | 0.61 | 19.91 | 17.52 | 1.27 | 20.49 |
| 30 | 9.59 | 1.02 | 29.85 | 22.84 | 2.50 | 30.88 |
| 40 | 14.79 | 2.21 | 39.82 | 10.36 | 1.53 | 41.60 |

### Differential Scanning Calorimeter (DSC) Analyses

The DSC250 was utilized to identify the glass transition temperatures ($T_g$) of membrane samples. This was done via the second trace from a cyclic heating protocol that oscillated between room temperature and 420 °C, before finally being heated to 550 °C. Both the heating and cooling procedures were conducted at a rate of 20 °C per minute.

Table 4.3: Glass transition temperatures ($T_g$) for the pure 6FDA-DAM film, as well as BZ and CZ MMMs, as determined by Differential Scanning Calorimetry (DSC).

| $T_g$ (°C) | 0 wt% | 10 wt% | 20 wt% | 30 wt% | 40 wt% |
|---|---|---|---|---|---|
| RDZ | 389.61 | 390.32 | 391.72 | 393.81 | 393.97 |
| CubZ | | 390.97 | 391.84 | 393.85 | 394.27 |

**Density of membranes**

Density measurements were performed following the Archimedes method (Ohaus 80253384 Solids Density Determination Kit). Each sample's dry weight was measured, and the sample was submerged in distilled water for the submerged weight measurement. This step was repeated five times with different part of each sample. The density of each sample was calculated using Archimedes' principle:

$$W_{dry} - W_{submerged} = \rho_{solvent} V_{sample} \tag{4.1}$$

where $W_{dry}$ and $W_{submerged}$ indicate weight of dry sample and weight of the same sample when submerged, respectively, and $\rho_{solvent}$ is the density of the reference solvent. From the volume of sample ($V_{sample}$) and dry sample weight, sample's density can be obtained ($W_{dry}/V_{sample}$). Measurements were conducted at a consistent temperature to avoid variations, and all apparatus was thoroughly cleaned before and after use.

**Wide-angle X-ray scattering (WAXS) Analysis**

WAXS patterns of pure MOF samples and their corresponding 40 wt% MMMs were recorded under a vacuum of 0.08 mbar using a SAXSLAB system, equipped with a DECTRIS PILATUS3 R 300K detector and a Rigaku 002 microfocus X-ray source. Patterns were gathered over a period of 1,200 seconds. The resulting data were then presented as intensity $I(q)$ against the scattering wavevector $q$, where $q$ is defined by the equation:

$$q = \frac{4\pi \sin\theta}{\lambda} \tag{4.2}$$

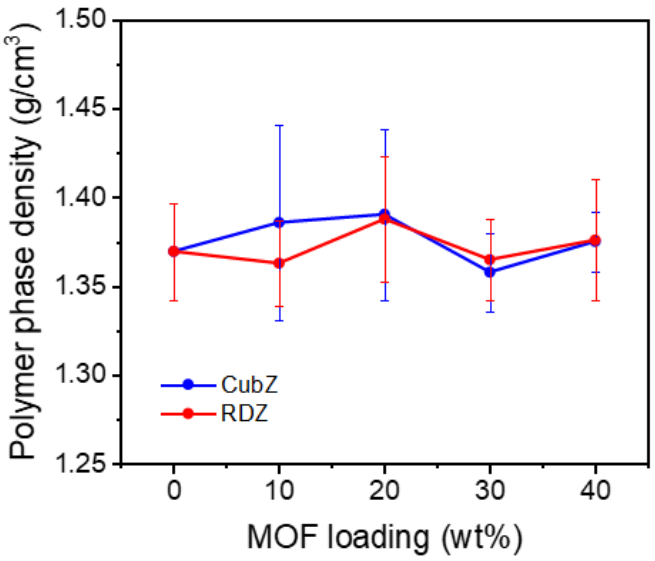


Figure 4-11: The polymer phase density of all MMM samples (the specific values are provided in Table 4.4).

Table 4.4: Density measurements of all membrane samples were conducted, and the polymer phase density was subsequently calculated, assuming a fixed ZIF-8 density of 0.95 g/cm$^3$. The average and standard deviation values were determined from 5 different measurements.

| Sample | Measured | Std | Polymer | Std |
|---|---|---|---|---|
| 6FDA-DAM | 1.370 | 0.027 | | |
| CubZ10 | 1.325 | 0.053 | 1.386 | 0.055 |
| CubZ20 | 1.273 | 0.044 | 1.391 | 0.048 |
| CubZ30 | 1.203 | 0.019 | 1.358 | 0.022 |
| CubZ40 | 1.166 | 0.014 | 1.375 | 0.017 |
| RDZ10 | 1.306 | 0.023 | 1.363 | 0.024 |
| RDZ20 | 1.271 | 0.032 | 1.388 | 0.035 |
| RDZ30 | 1.207 | 0.020 | 1.365 | 0.023 |
| RDZ40 | 1.156 | 0.044 | 1.376 | 0.034 |

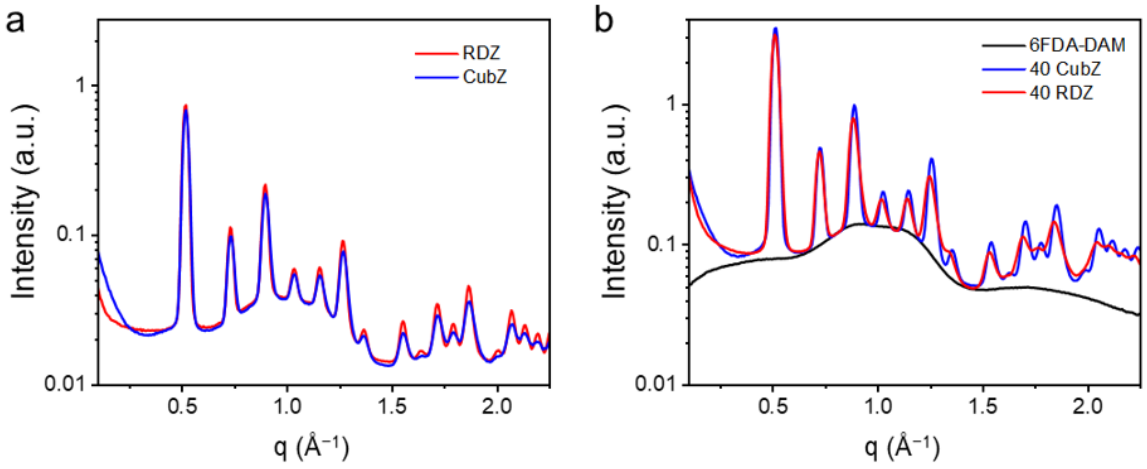


Figure 4-12: WAXS spectra depicting (a) pure MOFs and (b) pure polymer and MMMs at 40 wt%. The MOF samples exhibit similar peak locations, with slightly smaller d-spacings observed for CubZ MMM compared to RDZ MMM. For instance, the first peak measures 12.3 Åfor RDZ MMM and 12.16 Åfor CubZ MMM.

where $\theta$ is Bragg's angle and $\lambda$ is the X-ray beam's wavelength. Each peak identified from these patterns was processed using the "Gaussian peak + slope background" function in the SAXSGUI software.

### Nuclear magnetic resonance (NMR) analyses

Solution $^{1}$H-NMR spectra were obtained on an Ascend™ spectrometer (Bruker) with TopSpin™ 3.2 (500 MHz), from 1–5% (w/v) solutions using 0.7 mL of acetic acid-$d_4$ ($CD_3CO_2D$) to assess as-synthesized MOF particles as shown in Fig 4-4. As-synthesized MOF particles were tested to confirm the similar peak ratio, and CTAB was tested under the same conditions to verify the absence of significant modulator post-washing steps for CubZ.

$^{13}$C magic angle spinning (MAS) solid-state nuclear magnetic resonance (SS-NMR) spectra were obtained on a Bruker Avance Neo spectrometer with a power of 500.18 MHz, fitted with a 3.2 mm HX solids probe. All spectra were collected for 1024 scans at a spin rate of 20 kHz, a spectral width of 200 ppm, and spin-lock time of 0.001, 0.01, 0.02, 0.05, 0.1, 1, 2 ms. $T_{1\rho}$ values for each peak were calculated by fitting the integrated peak area values at different spin lock times to the following exponential equation:

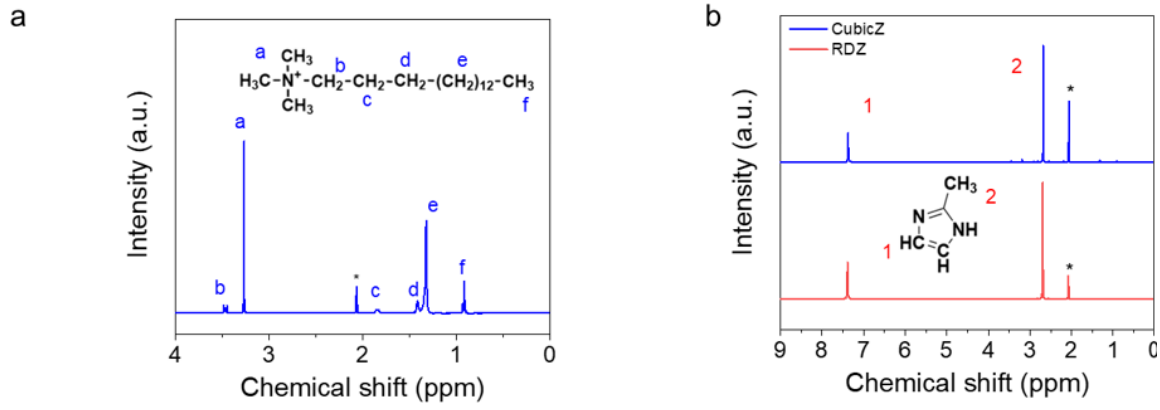


| CTAB | a | b | c | d + e | f |
|---|---|---|---|---|---|
| Stoich. ratio | 9 | 2 | 2 | 26 | 3 |
| Integrated | 9.00 | 2.00 | 2.04 | 26.12 | 3.00 |

| ZIF-8 | 1 | 2 |
|---|---|---|
| Stoich. ratio | 2 | 3 |
| CubZ | 2.00 | 3.14 |
| RDZ | 2.00 | 3.13 |

Figure 4-13: $^{1}$H NMR digestion spectra and integrated peak ratio, provided alongside the theoretical stoichiometric ratio, for (a) pure CTAB and (b) as-synthesized RDZ and CubZ samples. The $'a'$ peak of (a) resurfaced in the CubZ peak of (b), indicating that only 0.77 mol% of CTAB is retained in CubZ after three washing cycles. Asterisks represent the solvent peak locations.

$$A = A_0 \exp\left(\frac{-\tau}{T_{1\rho}}\right) \tag{4.3}$$

where $A$ is integrated peak area, $A_0$ is pre-factor, and $\tau$ is the spin-lock time.

Table 4.5: SS-NMR peak locations for ZIF-8 (RDZ, CubZ), 6FDA-DAM, 40 wt% RDZ MMM, and 40 wt% CubZ MMM (refer to peak a –c of Fig 4-3). Average and standard deviation values were calculated from 7 distinct patterns using various spin-lock times. The carbon used to derive the peak location is highlight in bold.

| Facet termination on the surface | Average projected area per aperture (Å$^2$) | | Average surface area per aperture (Å$^2$) | | Average angle to the horizontal plane (degree) | | Closest non-neighbor zincs distance (Å) |
|---|---|---|---|---|---|---|---|
| | 6MRs | 4MRs | 6MRs | 4MRs | 6MRs | 4MRs | |
| CubZ ({100} facet) | 53.7 | 35.0 | 96.2 | 35.4 | 54 | 1 | 8.5 |
| RDZ ({110} facet) | 74.9 | 25.8 | 93.7 | 35.2 | 33 | 43 | 10.5 |

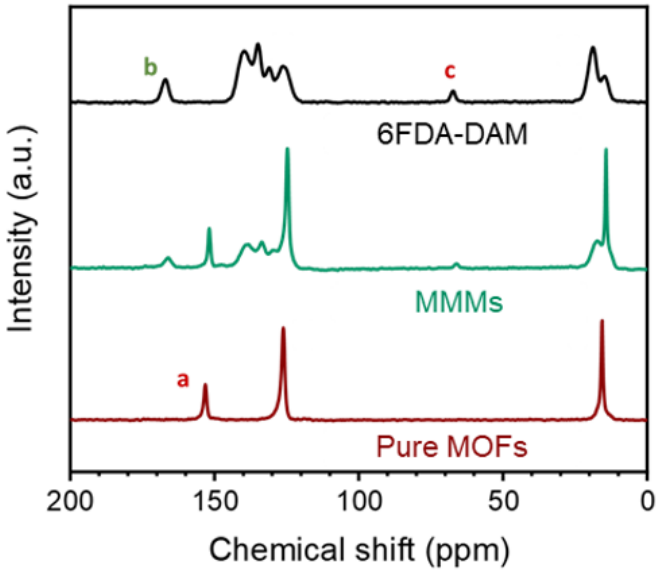


Figure 4-14: (a) $T_{1\rho}$ results derived from non-overlapping peaks in solid-state $^{13}$C NMR spectra. The chemical formulae of the ZIF-8

**Attenuated total reflection (ATR) Fourier transform infrared (FT-IR)**

ATR FT-IR spectra of 6FDA-DAM pure polymer (PI, polyimide), as-synthesized RDZ and CubZ, and corresponding MMMs at different loading (10, 20, 30, 40 wt%) were collected using a Thermo Fisher FTIR6700 for 32 scans at a resolution of 1 $cm^{-1}$ within the 400–4000 $cm^{-1}$ range.

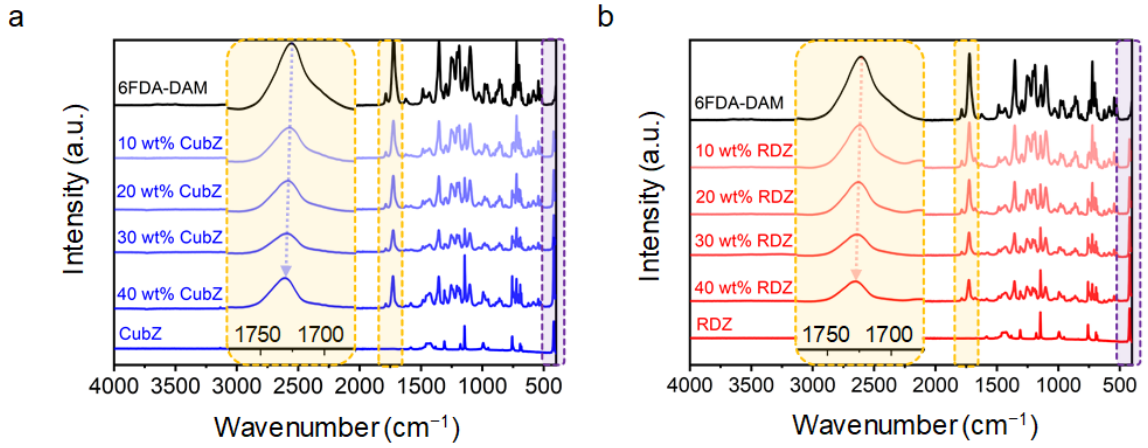


Figure 4-15: Fourier Transform Infrared (FT-IR) spectroscopy spectra are presented for (a) CubZ and its associated MMMs, and (b) RDZ and its related MMMs, at a range of MOF loadings (0, 10, 20, 30, and 40 wt%). Purple dashed boxes highlight Zn-N bonding, while yellow dashed boxes denote the presence of carbonyl stretching with the magnified region on the left depicting 1800 to1650 $cm^{-1}$.

Table 4.6: Peak locations (cm $^{-1}$) of C=O, Zn-N, C-N of all the samples

| Model | Surface 100 (kJ/mol) | | Surface 110 (kJ/mol) | |
|---|---|---|---|---|
| | Biding Energy | Dispersion interaction contribution | Biding Energy | Dispersion interaction contribution |
| Fragment 1 | −368.5 | −75.6 | −192.0 | −55.7 |
| Fragment 2 | −29.4 | −28.9 | −35.9 | −27.7 |
| Fragment 3 | −74.7 | −74.5 | −75.7 | −68.5 |

### 4.3.3 Computational study on MOF–polymer interaction

Investigating the surfaces of MOFs and their interactions with polymeric materials are important to help with the selection of optimal MOF/polymer matrix compositions for specific applications. Computational developments in this area have lagged behind experimental advances largely due to major challenges in the modeling of MOF/polymer MMMs. Polymer systems are typically large and require classical molecular simulation methods like Monte Carlo or molecular dynamics, which rely on force fields to describe inter-particle interactions. On the other hand, MOFs exhibit unique chemical behaviors influenced by electronic properties, demanding modeling approaches that consider quantum mechanical details. However, force field-based methods struggle to accurately capture these quantum mechanical aspects and adsorption behaviors with simple functions. Therefore, developing computational models suitable for studying MOF surfaces and their interaction with polymers in MMMs is an important challenge to consider for studies such as this one. Here, the electronic structure calculation method, density functional theory (DFT), was employed which allowed for investigation of the electronic interactions in such systems, but also limits the length scale of polymer-based functionality that can be considered in our analysis. Thus, our approach may not encompass the full complexity of the system, but it does provide a valuable framework for investigating the electronic aspects of ZIF-8 and 6FDA-DAM interactions and binding energies, which are the most important molecular features for the length scale of diffusion at the MOF–polymer interface.

### Theoretical methods

Density functional theory (DFT) calculations were performed to investigate the surface properties of the slab model of unsaturated ZIF-8 surfaces {110} and {100} and the MOF–polymer interactions. This approach involved expanding the orbitals, density, and potential on a plane-wave basis set, and using the projector-augmented-wave (PAW)8 method to describe electron-ion interactions. DFT calculations were performed employing the Vienna Ab initio Simulation Package (VASP)9 and utilized the Perdew, Burke, and Ernzerhof (PBE) exchange-correlation functional with the generalized gradient approximation.10 Van der Waals interactions were accounted for by using Grimme's zero damping D3 dispersion corrections.11 To find the ground state energy, the energy cutoff sampling using a cutoff of 600 eV was performed, and the total electronic and ionic energy convergence criteria of 10–5 eV and 0.03 eV/Åwere established, respectively. The reciprocal space integration with a Monkhorst–Pack grid of Γ point ($1 \times 1 \times 1$ k-point sampling in the Brillouin zone) was used.

### Models of ZIF-8 Surface

The development of surface models is crucial for understanding ZIF-8 interactions with the polymer. It has been shown that the {110} surface is the most thermodynamically stable surface in ZIF-8 followed by the {100} surface. Published slab models by Pang et al. were used to evaluate each of these surfaces.[124] Geometry optimizations were carried out by considering the bottom layer with fixed atomic positions and the upper two layers with fully relaxed atomic positions. The slab model consisted of three layers and a vacuum layer of at least 20 Åto limit interactions between periodic structures. In these calculations, due to the induced dipole existing in the asymmetric slab models and the presence of frozen and relaxed geometries, dipole corrections (IDIPOL, DIPOL, and LDIPOL) were included to adjust the energies. Slab models with the ground state energy were used to investigate the geometrical properties of different apertures on each surface facet and to further identify the differences between them. To account for the flexible nature of the apertures, which

open through the reorientation of imidazolate linkers upon gas transfer (known as the 'gate opening' phenomena), we made the assumption of approximating the linkers as straight lines connecting two unsaturated zinc sites. To calculate the surface area of the apertures (6MRs and 4MRs), it is important to note that the zinc metal sites are not perfectly aligned on the same plane. Therefore, the apertures were divided into multiple triangles using the corners formed by the metal sites. As shown in Fig 4-16, each aperture was covered by two sets of triangles, with each set consisting of different triangles. By averaging the calculated surface areas via two sets, a more precise estimation of the surface area was obtained.

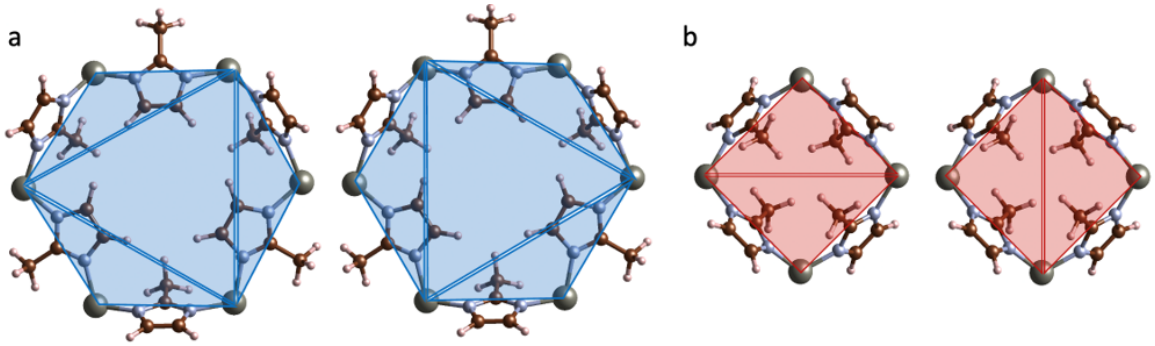


Figure 4-16: Illustration of the two sets of triangles used to cover each specific aperture, (a) 6MRs and (b) 4MRs, to calculate the surface area of the apertures. Color scheme: zinc (gray), carbon (brown), nitrogen (blue), and hydrogen (white).

Moreover, the angle of each aperture was determined by computing the angles of all the triangles covering the aperture and then calculating the average angle for each aperture. This allowed us to determine the orientation of each aperture with respect to the surface (horizontal plane). To further compare the two surfaces of ZIF-8, the projected surface areas of apertures on the flat 2D horizontal plane were calculated. Table S5 presents the geometric specifications of {110} and {100} ZIF-8 surfaces. As the projections of apertures are shown in Fig 4-17, surface {110} contains four 4MRs and four 6MRs apertures, while surface {100} features two 4MRs and four 6MRs apertures, as denoted with numbering. The average areas reported in Table S5 represent the average values calculated for each specific aperture in the respective surfaces.

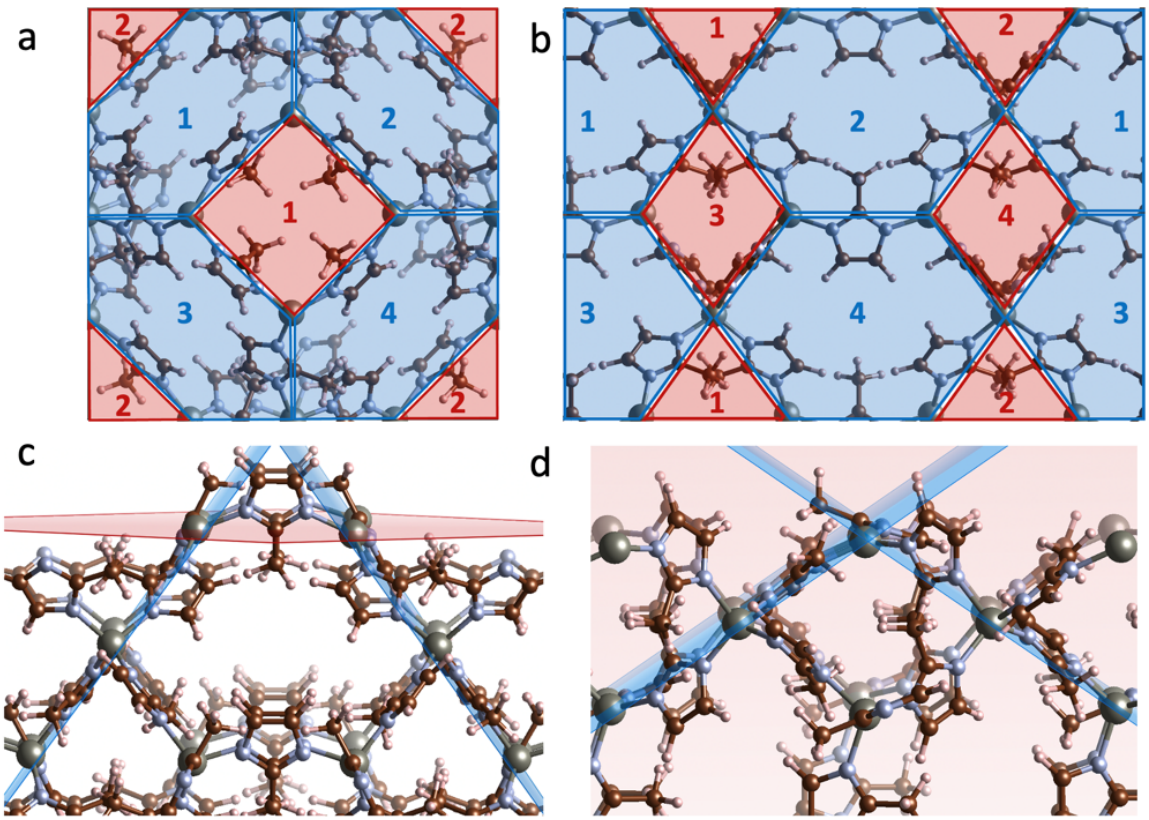


Figure 4-17: The projected surface area on the flat 2D horizontal plane (top view) of (a) CubZ {100} and (b) RDZ {110} ZIF-8 surfaces are presented. Schematic of the angles of distinct apertures viewed from the side on (c) CubZ {100} and (d) RDZ {110}. 6MR apertures are highlighted as blue and 4MR apertures are highlighted as red. Color scheme: zinc (grey), carbon (brown), nitrogen (blue), and hydrogen (white).

Table 4.7: Measured geometrical specifications of {110} and {100} ZIF-8 surfaces

| Facet termination on the surface | Average projected area per aperture (Å$^2$) | | Average surface area per aperture (Å$^2$) | | Average angle to the horizontal plane (degree) | | Closest non-neighbor zincs distance (Å) |
|---|---|---|---|---|---|---|---|
| | 6MRs | 4MRs | 6MRs | 4MRs | 6MRs | 4MRs | |
| CubZ ({100} facet) | 53.7 | 35.0 | 96.2 | 35.4 | 54 | 1 | 8.5 |
| RDZ ({110} facet) | 74.9 | 25.8 | 93.7 | 35.2 | 33 | 43 | 10.5 |

As it is shown in Table 4.5, the surface areas of 6MRs and 4MRs in each surface exhibit no significant differences. However, when comparing the projected surface areas, it is evident that surface {110} has a significantly larger surface area for 6MRs compared to the surface area for surface {100}. Conversely, for the other aperture, 4MRs, surface {100} exhibits a larger projected surface area than surface {110}. As 6MR (windows of ca. 3.4 Å) has a major impact on gas transport because 4MR has diminutive pore size (windows of ca. 0.8 Å),[132] {110} can be viewed as a more accessible surface structure.

**Adsorption of 6FDA-DAM on ZIF-8 surfaces**

The application of DFT calculations to polymers poses certain challenges and limitations due to their inherent flexibility and the existence of numerous soft modes (including rotations and vibrations) and having a large number of atoms.13 Acknowledging the limitations associated with treating the polymeric materials, employing an established approach previously used for a similar composite system,14 we developed a simplified manner to study the interaction of the 6FDA-DAM polymer with the different facets of ZIF-8.

In this study, to reduce the soft modes of the long polymer and produce models that are more appropriate for DFT calculations, an identical set of three fragments of 6FDA-DAM polymer were considered and tuned electronically (terminated with functional groups, such as SH, F, and Cl, as detailed in the previous study of the 6FDA-Durene polymer[133]), ensuring they represent the polymer. Because of the structural similarities between 6FDA-DAM and 6FDA-Durene, the same functional groups for the fragment models were adopted. Considered fragment models of the 6FDA-DAM structure are presented in Fig 4-18. DFT calculations of polymer adsorptions highlighted the significance of electronic interactions between these models of 6FDA-DAM with the surfaces of ZIF-8. Of note, these interactions are specifically significant for fragment model 1, which contains two carbonyl groups.

The adsorption energetics of the polymer fragment models to the surfaces of ZIF-8 were computed as follows:

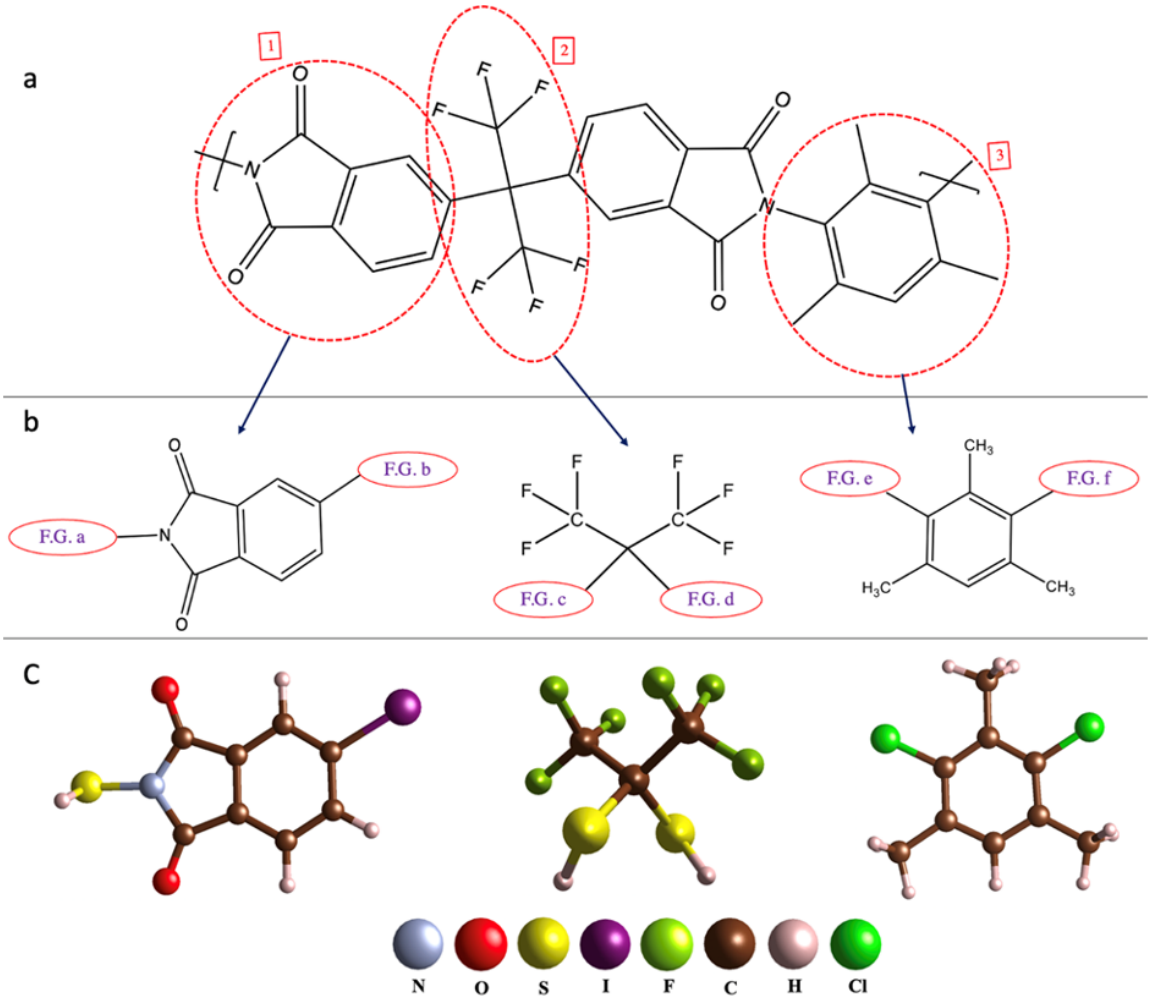


Figure 4-18: (a) 6FDA-DAM monomer and its decomposition into the fragments. (b) Decomposed monomer into three unique fragments and terminated with functional groups (F.G). (c) Tuned fragment models (fragment 1 terminated with SH and I, fragment 2 terminated with two SH groups, and fragment 3 terminated with two chlorines)

$$\Delta E = E_{frag+slab} - E_{frag} - E_{slab} \tag{4.4}$$

where , $E_{frag+slab}$, $E_{frag}$, and $E_{slab}$ denote the binding energy, the energy of the polymer fragment bonded to the MOF slab, the energy of the isolated polymer fragment molecule in a 20 Å box, and the energy of the slab model of pure MOF, respectively. To report the binding energy of the polymer to the MOF surfaces, several binding sites for the polymer fragments were examined to find the most thermodynamically stable adsorption site for that fragment model on the surface. The DFT-D3 method was employed in all calculations to assess the adsorption energetics of dispersion interactions. Dispersion interactions refer to the attractive component of van der Waals interactions between atoms or molecules that are not directly bonded to each other (neither covalently nor ionically). This approach allowed for the determination of the extent to which dispersion forces influence the adsorption of each polymer fragment on multiple MOF surfaces. The dispersion energy contributions to adsorption were calculated using the same equation as described for binding energies, with the distinction that dispersion energies were specifically employed for these calculations.

The calculated binding energy and dispersive contributions to the binding energy of the electronically tuned fragment models of 6FDA-DAM on both surfaces {100} and {110} of ZIF-8 are reported in Table 4.6.

Table 4.8: DFT calculated binding energies and their respective dispersion interaction contributions for polymer fragment model adsorption on the {110} and {100} ZIF-8 surfaces

| Model | Surface 100 (kJ/mol) | | Surface 110 (kJ/mol) | |
|---|---|---|---|---|
| | Biding Energy | Dispersion interaction contribution | Biding Energy | Dispersion interaction contribution |
| Fragment 1 | −368.5 | −75.6 | −192.0 | −55.7 |
| Fragment 2 | −29.4 | −28.9 | −35.9 | −27.7 |
| Fragment 3 | −74.7 | −74.5 | −75.7 | −68.5 |

As shown in Table 4.6, two of the three polymer fragment models (2 and 3) have weaker binding energies than that of fragment 1 and the adsorptive behavior for these

fragments is predominantly governed by dispersion interactions, which are typically associated with poor wetting and adhesion behavior at the interface. However, in fragment model 1, the interaction between the oxo groups and the undercoordinated metal site (zinc) on the surface of ZIF-8 is characterized by strong electrostatic and electronic forces. These interactions have a considerable impact on the adsorption behavior and show much smaller contribution of dispersion.

These observations align with previous studies conducted on the interaction of ZIF-8 surfaces with polymers.14,15 Based on our observations, it has been determined that the interactions involving the oxo groups contribute to the strongest binding strength between 6FDA-DAM and the surfaces of ZIF-8. Using the tuned polymer fragment the affinity of the 6FDA-DAM towards ZIF-8 surfaces was quantified. Additionally, the intensity of the binding energies of 6FDA-DAM polymer to each surface of ZIF-8 was assessed by comparing the binding energies of the fragments to the various surfaces of ZIF-8. The findings show that the polymer is more exothermically bound to surface {100} than to surface {110}. This finding suggests that the 6FDA-DAM polymer exhibits a stronger affinity for surface {100}, providing a facet specific interaction between the MOF and the polymer. This strong binding to surface {100} can be attributed to the shorter distances between two non-immediate neighbor unsaturated zinc atoms on this surface, as indicated in Table S5.

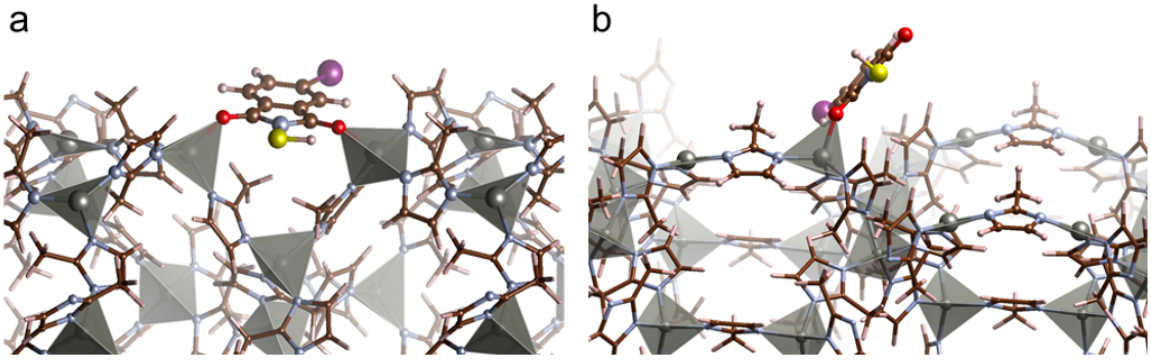


Figure 4-19: Bonded fragment model 1 on surfaces of ZIF-8 (a) CubZ {100} and (b) RDZ {110}. Color scheme: zinc (grey), carbon (brown), oxygen (red), nitrogen (blue), iodine (purple), hydrogen (white), sulfur (yellow). Note that iodine and sulfur are not in the polymer structure but were used as simplified functionalities for end caps on fragments.

This proximity allows the polymer to form two binding interactions simultaneously from the two oxo groups on only one fragment as is shown in Fig 4-19. In contrast, the longer distance between these metal sites on the surface {110} prevents the polymer from forming such simultaneous bindings. This discrepancy in distance of the two non-immediate neighbor unsaturated metal sites is influenced by the angle of the 6MRs on the surface {100}, as we discussed earlier.

After conducting a detailed analysis using the electronically tuned fragment models, the key interactive segments of the 6FDA-DAM polymer with the ZIF-8 surfaces were identified. Building on these understandings and considering the challenges of DFT calculations for long polymers, the interaction of an extended model of a monomer proceeded. This new model allowed us to explore and quantify the binding energy of the polymer on different facets ({100} and {110}) of the ZIF-8. By leveraging the insights gained from the fragment models, we were able to validate and further refine our predictions using the extended monomer model.

The results indicate that the extended model also exhibits strong interactions with the oxo groups of the carbonyl functionality in the phthalimide segments. Fig 4-46k and l display the interactions of the extended monomer models with the {100} and {110} surfaces of ZIF-8. Notably, unlike fragment model 1, which was unable to bind bidentantly by its oxo groups due to longer distances between two non-immediate neighbors of unsaturated zinc metal sites on the {110} surface of ZIF-8, the extended monomer model, with its greater length, can now bind bidentantly using the two oxo groups of two distinct phthalimide segments. This enhanced binding capability of the extended model provides valuable insights into the interactions between the 6FDA-DAM polymer and the ZIF-8 surfaces, enriching our understanding of the underlying mechanisms that govern their affinity and adhesion. Of note, bidendate interactions of pthalamide groups provides a stronger interaction for gate opening at the surface, since this functionality does not have rotational modes that are anticipated for the longer polymer segments. Thus, the interactions at the length scale of pthalamide units in an imide appear to be a key design feature in restricting gate opening behavior in ZIF-8.

The binding energy of the extended monomer model of 6FDA-DAM was computed using equation S4, replacing the fragment models with the extended monomer model. The results in Table S7 reveal that, as anticipated, the dispersion interaction contribution in the binding energy of the model on both surfaces {100} and {110} of ZIF-8 increased due to the larger size of the extended monomer model and the presence of more material. Interestingly, the higher dispersion interaction contribution observed on surface {100} may be attributed to its higher density and close packing surface. Despite the fact that the extended monomer model on surface {100} interacts with only two oxo groups of one phthalimide segment, similar to the fragment model, the binding energy of the extended monomer model on surface {100} (–398.5 kJ/mol) is still greater than when it binds bidentantly on surface {110} (–305.4 kJ/mol). This result validates our understanding that the polymer exhibits a stronger affinity and stronger binding to surface {100} of ZIF-8.

Table 4.9: DFT calculated binding energies and their respective dispersion interaction contributions of the extended monomer model of 6FDA-DAM polymer adsorption on the {110} and {100} ZIF-8 surfaces.

| Model | Surface {100} (kJ/mol) | | Surface {110} (kJ/mol) | |
|---|---|---|---|---|
| | Biding Energy | Dispersion interaction contribution | Biding Energy | Dispersion interaction contribution |
| Extended monomer | −398.5 | −160.1 | −305.4 | −134.6 |

### 4.3.4 Gas transport properties measurements

#### Gas Permeation Measurements

Pure-gas permeation tests of $H_2$, $N_2$, $CH_4$, $C_2H_4$, $C_2H_6$, $C_3H_6$, and $C_3H_8$ were conducted using an automated, custom-built, constant-volume, variable-pressure permeation system from Maxwell Robotics. Approximately 1 $cm^2$ membrane coupons were cut from the prepared films. The thickness of these coupons was measured five times using a micrometer to calculate an average and standard deviation. These coupons were then affixed to the center of a brass shim stock disk with an outer diameter of 47 mm and an inner diameter of 7 mm using impermeable 5-min epoxy glue (Devcon,

14250). This setup resulted in an active permeation area ranging from 5–20 $mm^2$, as determined by a scanned image and ImageJ software (NIH). Again, this measurement process was repeated five times to compute an average and standard deviation.

The samples were then sealed in a stainless-steel cell and held at one of five distinct temperatures (7, 20, 35, 50, 65 °C). Temperature regulation was managed by a PID temperature controller (Omega, CNI852-EI) and a chiller (for sub-ambient temperatures, Vevor, B0849YQMY4). Every test implemented a procedure to guarantee a leak rate of less than 10% of the gas permeation rate, as determined under a static vacuum for 1 hour prior to testing. Before the testing procedure, each sample was left under vacuum for a minimum of 8 hours (12 hours for $C_2$ and $C_3$ gases). This was followed by a helium flush at 1 atm, further degassing, and an additional 30-minutes vacuum hold before introducing different gases. Each sample was tested two to three times to determine average values, with the calculated uncertainty reported as the average instrumental error, derived from the leak rate, the area, and the thickness measurements.

The permeation rate of each gas was determined from the steady-state pressure rise in the downstream volume, as illustrated by the following equation:

$$P_i = \frac{Vl}{pART} \cdot \frac{dp_i}{dt} \tag{4.5}$$

In this equation, $P_i$ represents the pure gas permeability ($i$: $H_2$, $N_2$, $CH_4$, $C_2H_4$, $C_2H_6$, $C_3H_6$, and $C_3H_8$) in barrer $10^{-10}$ $cm^3$(STP) cm $cm^{-2}$ $s^{-1}$ $cmHg^{-1}$), $V$ denotes the downstream volume ($cm^3$), $l$ stands for the membrane thickness (cm), $p$ refers to the average upstream pressure (cmHg), $A$ is the active area of the film, $R$ is the ideal gas constant, $T$ is the absolute temperature (K), and $dp_i/dt$ represents the steady-state pressure rise in the downstream (cmHg $s^{-1}$) after subtracting the leak rate. The ideal selectivity ($\alpha$) was determined as the ratio of two pure gas permeabilities ($P_i/P_j$), where $i$ is more permeable.

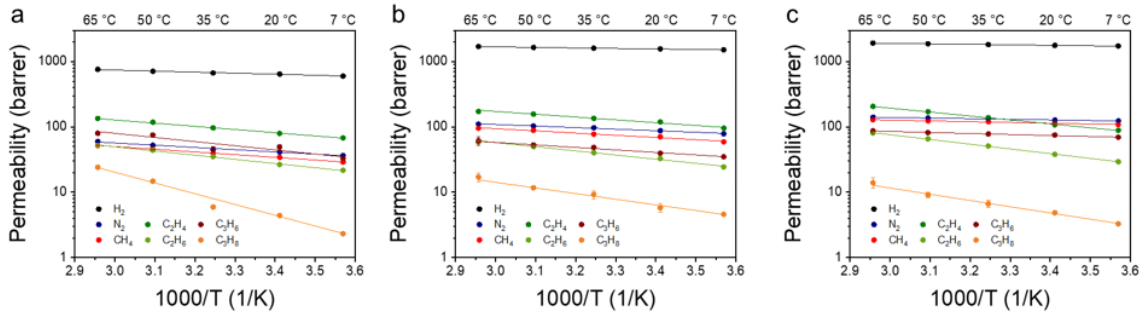


Figure 4-20: Permeability of all gases evaluated ($H_2$, $N_2$, $CH_4$, $C_2H_4$, $C_2H_6$, $C_3H_6$, $C_3H_8$) plotted against the inverse temperature for (a) 6FDA-DAM, (b) 30 wt% CubZ MMM, and (c) 30 wt% RDZ MMM. Lines indicate best fits using a van't Hoff expression.

### Gas Sorption Measurements

$H_2$, $N_2$, $CH_4$, $C_2H_4$, $C_2H_6$, $C_3H_6$, and $C_3H_8$ sorption isotherms were collected at the same 5 temperature points (7, 20, 35, 50, 65 °C) for 30 wt% MMMs and pure polymer membrane as shown in Figure S18– S24. For pure MOF samples, the same set of gas was tested at 35 °C to confirm the identical sorption property as shown in Fig 4-21.

The measurements were achieved using an automated pressure decay method, facilitated by a dual volume and dual transducer sorption system sourced from Maxwell Robotics. For each test, a sample comprising 0.08–0.2 g of membrane film or MOF powder was utilized.

Following the loading of the sample, the cell was sealed using a VCR gasket, after which the entire system underwent a 12-hour evacuation process. This step was critical for the removal of any dissolved gases and moisture present within the films. The quantity of gas sorbed by the sample at each pressure point was determined through a mole balance calculation, performed between each dosing and equilibration phase.

For the membranes, each sorption isotherm was fitted using the dual-mode sorption (DMS) model. This model combines Henry's and Langmuir's sorption laws and is commonly used to describe sorption in glassy polymers.[134] By considering both mechanisms, the dual-mode sorption model provides a more comprehensive understanding of gas sorption behavior in membranes. The DMS equation is shown below,

where the first term represents the Henry mode and the second term, the Langmuir mode.

$$C_i = k_{D,i} p_i + \frac{C'_{H,i} b_i p_i}{1 + b_i p_i} \tag{4.6}$$

where $C_i$ is the concentration of gas $i$ (=$H_2$, $N_2$, $CH_4$, $C_2H_4$, $C_2H_6$, $C_3H_6$, and $C_3H_8$) sorbed in the membrane ($cm^3(STP)cm^{-3}$), $p_i$ is the equilibrated fugacity (atm), $k_{D,i}$ is Henry's constant ($cm^3(STP)cm^{-3}$ $atm^{-1}$) that shows the properties of polymer phase, $C'_H$ is the Langmuir sorption capacity ($cm^3(STP)cm^{-3}$), and $b_i$ is the Langmuir affinity constant ($atm^{-1}$) that shows the combined contributions from polymer and MOF phase.[99] Specifically, $k_{D,i}$ signifies the equilibrium constant of a penetrant transitioning between the gaseous and the dissolved state, while $b_i$ is an equilibrium constant that characterizes the relative rates of surface adsorption and desorption pertaining to the Langmuir mode. To address the possibility of multiple equally good fits due to the three-parameter fitting, a cross-correlation analysis using a nonlinear optimization was performed in MATLAB by $\chi^2$ (propagated error[66]) minimization, following the method proposed by Wu et al.[135] This approach involved constraining each variable with scientific reasoning to identify the most suitable fit among the alternatives.

Sorption coefficients were acquired by dividing the gas concentration at the pressure where the permeation test of the specific gas and temperature was conducted ($\approx$ 1 bar, S = C/p). Furthermore, diffusion coefficients were computed by applying the sorption-diffusion model (P = D $\times$ S).[50] Both sorption and diffusion coefficients at 35 °C are plotted in Figure 4-25.

### 4.3.5 MMM gas transport model analysis

Evaluating transport behavior in MMMs requires an understanding of the permeation properties of each individual component, including the continuous phase and dispersed phase. Multiple modeling approaches have been developed to facilitate the prediction

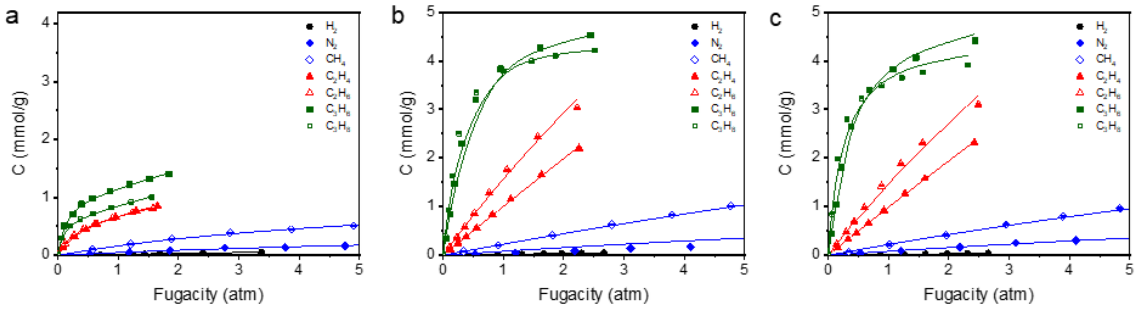


Figure 4-21: Sorption isotherms of all tested gases ($H_2$, $N_2$, $CH_4$, $C_2H_4$, $C_2H_6$, $C_3H_6$, $C_3H_8$) are depicted for (a) 6FDA-DAM polymer membrane, (b) pure RDZ, and (c) pure CubZ MOF particles. Individual data points represent experimental findings, while the superimposed lines correspond to fits from either dual-mode sorption model or the Langmuir sorption model. RDZ and CubZ values were consistent with the values from the previously reported data for ZIF-8.[16] The unit of C is converted to mmol/g assuming the density of ZIF-8 is 0.94 g/cm$^3$.[21, 22]

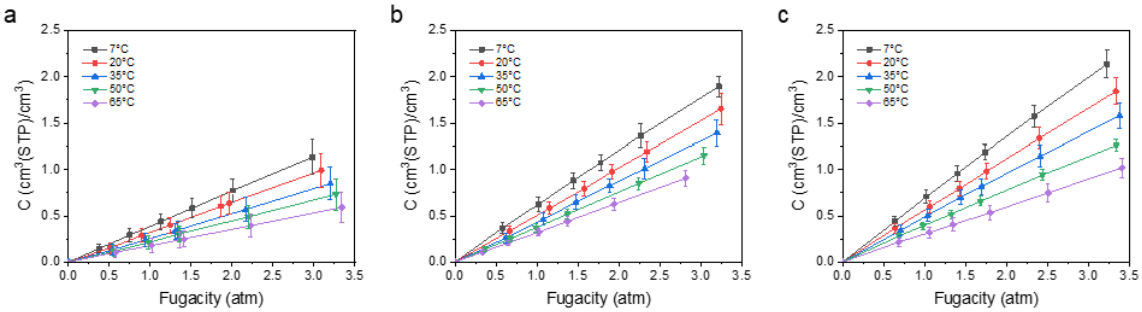


Figure 4-22: $H_2$ sorption isotherm for (a) 6FDA-DAM, (b) 30 wt% CubZ MMM, and (c) 30 wt% RDZ MMM, obtained at temperatures of 7, 20, 35, 50, 65 °C. Individual data points correspond to experimental results, with the plotted lines indicating the dual-mode sorption model fit.

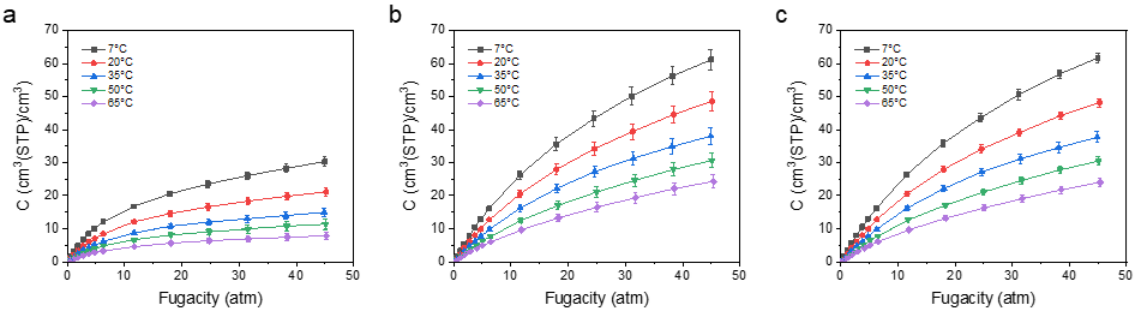


Figure 4-23: $N_2$ sorption isotherm for (a) 6FDA-DAM, (b) 30 wt% CubZ MMM, and (c) 30 wt% RDZ MMM, obtained at temperatures of 7, 20, 35, 50, 65 °C. Individual data points correspond to experimental results, with the plotted lines indicating the dual-mode sorption model fit.

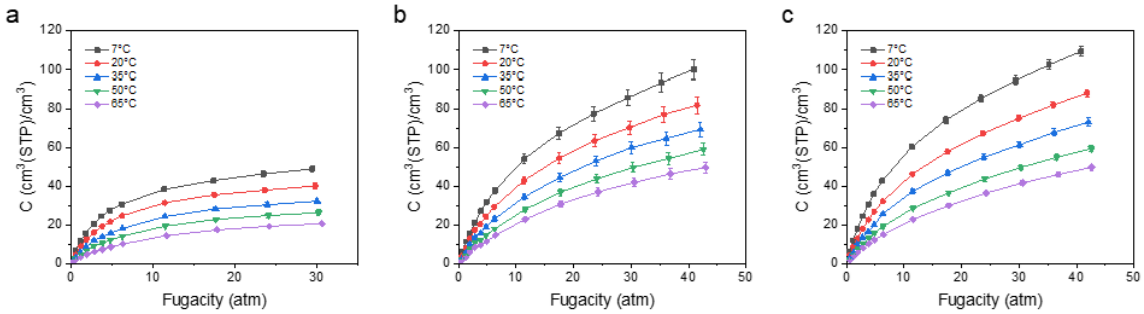


Figure 4-24: $CH_4$ sorption isotherm for (a) 6FDA-DAM, (b) 30 wt% CubZ MMM, and (c) 30 wt% RDZ MMM, obtained at temperatures of 7, 20, 35, 50, 65 °C. Individual data points correspond to experimental results, with the plotted lines indicating the dual-mode sorption model fit.

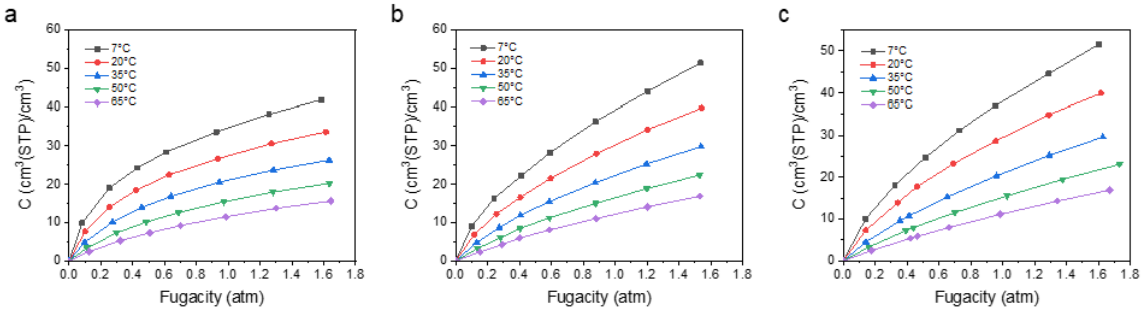


Figure 4-25: $C_2H_4$ sorption isotherm for (a) 6FDA-DAM, (b) 30 wt% CubZ MMM, and (c) 30 wt% RDZ MMM, obtained at temperatures of 7, 20, 35, 50, 65 °C. Individual data points correspond to experimental results, with the plotted lines indicating the dual-mode sorption model fit.

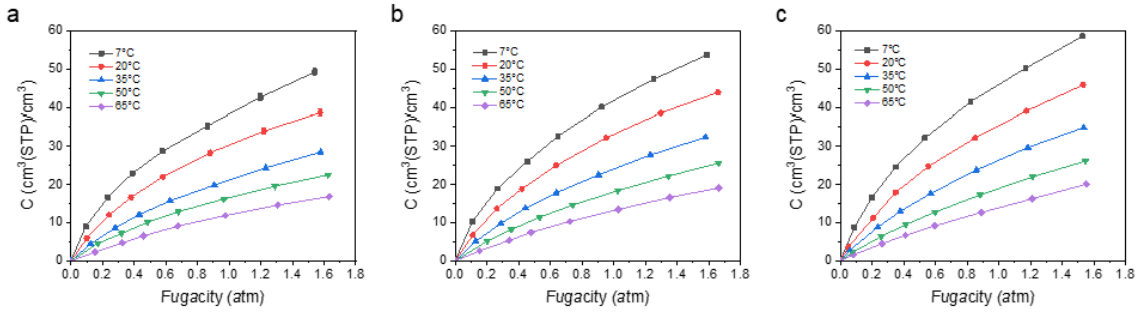


Figure 4-26: $C_2H_6$ sorption isotherm for (a) 6FDA-DAM, (b) 30 wt% CubZ MMM, and (c) 30 wt% RDZ MMM, obtained at temperatures of 7, 20, 35, 50, 65 °C. Individual data points correspond to experimental results, with the plotted lines indicating the dual-mode sorption model fit.

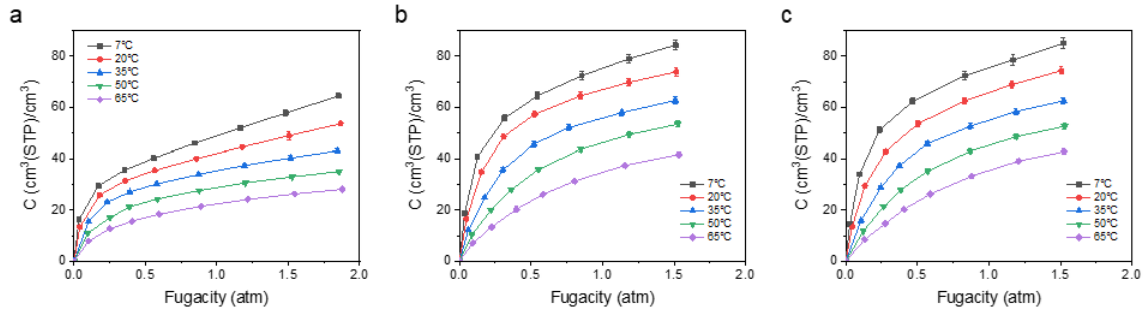


Figure 4-27: $C_3H_6$ sorption isotherm for (a) 6FDA-DAM, (b) 30 wt% CubZ MMM, and (c) 30 wt% RDZ MMM, obtained at temperatures of 7, 20, 35, 50, 65 °C. Individual data points correspond to experimental results, with the plotted lines indicating the dual-mode sorption model fit.

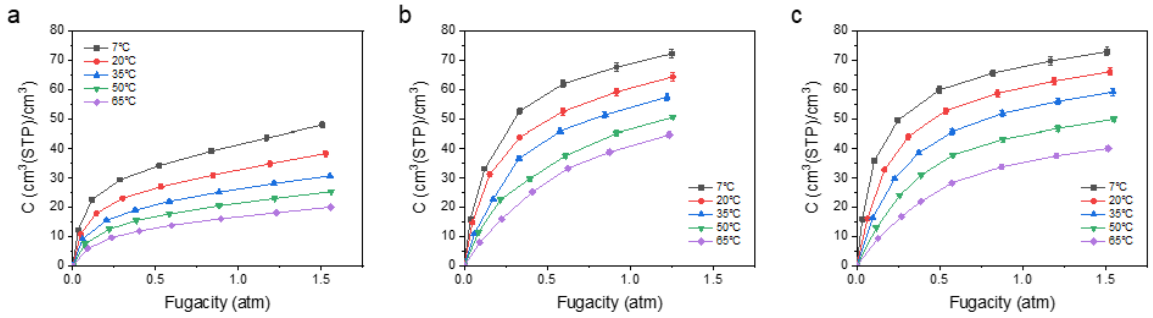


Figure 4-28: $C_3H_8$ sorption isotherm for (a) 6FDA-DAM(b) 30 wt% CubZ MMM, and (c) 30 wt% RDZ MMM, obtained at temperatures of 7, 20, 35, 50, 65 °C. Individual data points correspond to experimental results, with the plotted lines indicating the dual-mode sorption model fit.

of MMM performance, considering multiple factors such as the MMM's structure and investigating whether the MMM demonstrates an ideal or nonideal behavior.[67, 136] In an ideal MMM morphology, the two-phase system consists of a dispersed filler surrounded by a continuous polymer phase. This arrangement is characterized by a lack of defects at the interface between the polymer and the filler. In this study, due to the high compatibility of the ZIF-8 particles and the 6FDA-DAM polymer and the small size of the synthesized ZIF-8 particles, ideal permeation models were used for our analyses.

The aim of this part of the study is to predict gas permeation through pure MOF phases by using the obtained permeation data in the pure polymer and the MMM at different loadings. The investigation was conducted by employing two models that

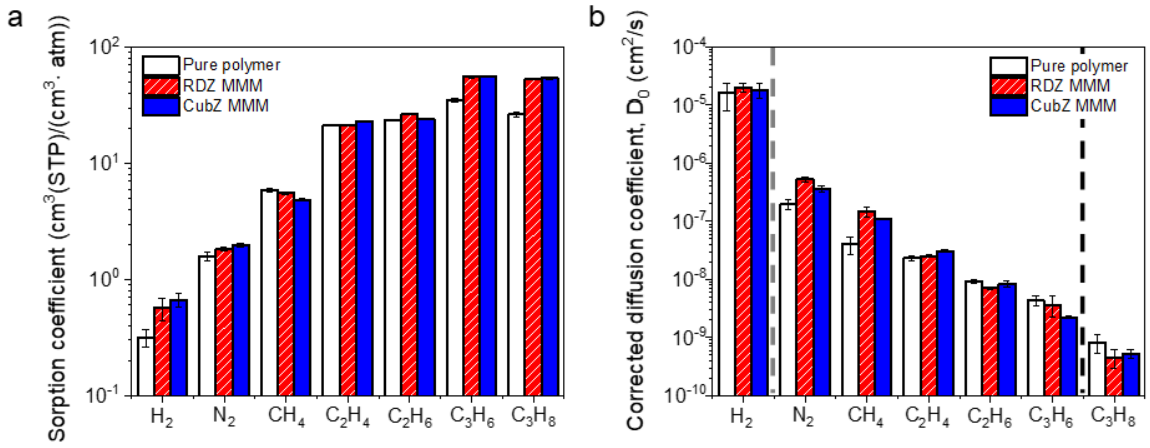


Figure 4-29: (a) Sorption coefficient and (b) corrected diffusion coefficient presented for the 6FDA-DAM pure polymer film, 40 wt% CubZ MMM, and 40 wt% RDZ MMM. Comparing diffusivity values for two MMMs, hydrogen shows similar values within errors yet CubZ MMM shows bigger decline for $N_2$ and $CH_4$ (grey dotted line). $C_3H_8$ also show similar values, yet $C_3H_6$ show much faster diffusion for RDZ (black dotted line).

have been developed for ideal two-phase MMMs, including the Maxwell–Wagner–Sillar (MWS) and Gonzo–Parentis–Gottifredi (GPG) models.[137, 138, 84]

Maxwell's theory was originally developed to calculate the electrical conductivity of composite materials.28 One widely applied version of this model for predicting the performance of an ideal MMM with ellipsoidal fillers is the MWS model.

$$P_{eff} = P_c \left[ \frac{nP_d + (1-n)P_c + (1-n)(P_d - P_c)\phi_d}{nP_d + (1-n)P_c - n(P_d - P_c)\phi_d} \right] \tag{4.7}$$

Where $P_c$, $P_d$, $n$, and $\phi_d$ are denoted as the permeabilities of the continuous phase (pure polymer), the permeabilities of the dispersed phase (pure MOF), the shape factor, and the volume fraction of particle loading respectively. Using $\rho_{\text{6FDA-DAM}} = 1.38$ g/cm$^3$ and $\rho_{\text{ZIF-8}} = 0.94$ g/cm3,[80, 139, 21, 22] the weight fractions of ZIF-8 particles in the 6FDA-DAM matrix were converted to volume fractions. The shape factor reflects the role of particle geometry in permeation through MMM and can range from 0 to 1. Where $n = 1/3$ is commonly associated with spherical particles and reduces the MWS model to the original Maxwell equation, $0 < n < 1/3$ corresponds

to transport through prolate ellipsoids, and $1/3 < n < 1$ represents transport through oblate ellipsoids. This model is only applicable to systems with low concentrations of fillers (volumetric of lower than 0.2) in MMM,[84] as it does not account for particle interactions.

The model was initially fitted using $n = 1/3$ (the original Maxwell equation) to predict the permeation of pure ZIF-8 on different facets. However, this model did not fit well with our experimental data, and the predicted pure permeation showed divergence for some gases. These limitations may arise from the original Maxwell model's assumptions, such as considering only dilute spherical particles randomly dispersed in a continuous phase. Alternatively, the polymer–MOF interactions, as evaluated through DFT, may create a volume-loading-dependence on filler property sets, which cannot be accounted for by the model.

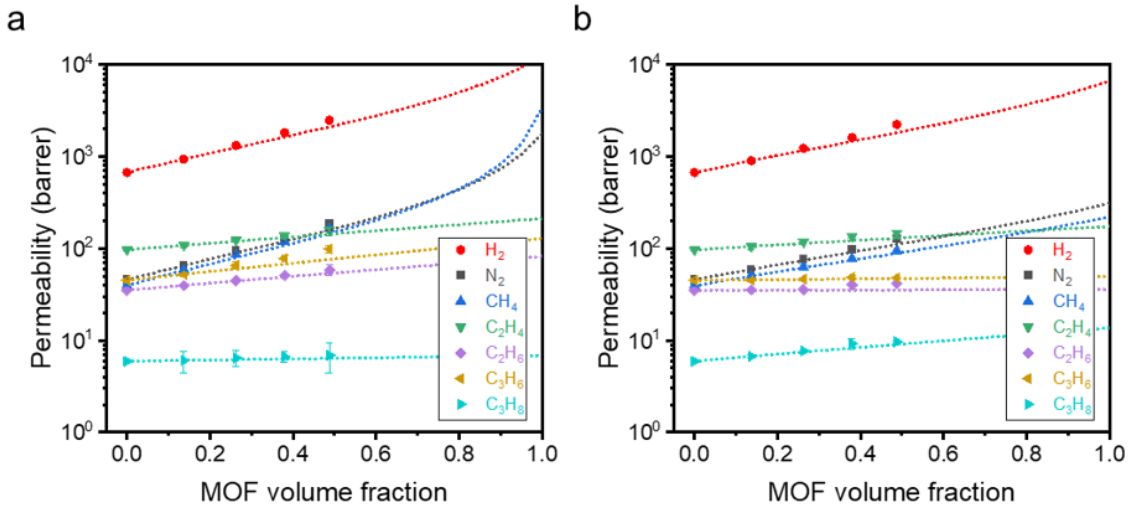


Figure 4-30: The original Maxwell fitting ($n = 1/3$ for the MWS model) for (a) CubZ MMM and (b) RDZ MMM. Individual data points correspond to experimental results, with the plotted dashed lines indicating the fitted permeability model.

In a subsequent attempt, the Maxwell model was applied specifically to MMMs with loading volume fractions lower than 0.2, where the model is considered valid.[84] However, only one point from the experimental data with such a volume fraction was used for fitting the model, which significantly hinders confidence in interpretability of the results. As it is demonstrated in Fig 4-30, the model underestimates the

permeation at higher loadings for all gases. This discrepancy could be attributed to both using only one point for fitting the model and the model's assumptions of spherical filler particles with no interaction between them and the polymer.

The GPG model is an extension model of the original Maxwell model that takes into account both the polymer–particle and particle–particle interactions.

$$\frac{P_{eff}}{P_c} = 1 + 3\beta\phi_d + K\phi_d^{\,2} \tag{4.8}$$

where:

$$K = a + b\phi_d^{1.5} \tag{4.9}$$

$$a = -0.002254 - 0.123112\beta + 2.93656\beta^2 + 1.690\beta^3 \tag{4.10}$$

$$b = 0.0039298 - 0.803494\beta - 2.16207\beta^2 + 6.48296\beta^3 + 5.271964\beta^4 \tag{4.11}$$

$$\alpha = \frac{P_d}{P_c},\ \beta = \frac{\alpha - 1}{\alpha + 2} = \frac{P_d - P_c}{P_d + 2P_c} \tag{4.12}$$

$a$ and $b$ are empirical corrective coefficients of the original Maxwell expression, $\alpha$ is a ratio between two phases, and $\beta$ (reduced permeation polarizability) is a practical indicator of the difference in penetrant permeability between the two phases, with a range of $-0.5 \leq \beta \leq 1$. The lower and upper bounds signify totally non-permeable and infinitely permeable filler particles (disperse phase), respectively, and $\beta = 0$ indicates equal permeability in both phases ($\alpha = 1$).

Fig 4-31 presents the results obtained using the GPG model. Unlike the original Maxwell model and the MWS model, the GPG model considers both particle–particle and particle–polymer interactions. This incorporation of interactions leads to improved permeation predictions compared to the previous models. Even for high loadings of the MMMs, the predicted permeations are in good agreement with experimental findings.

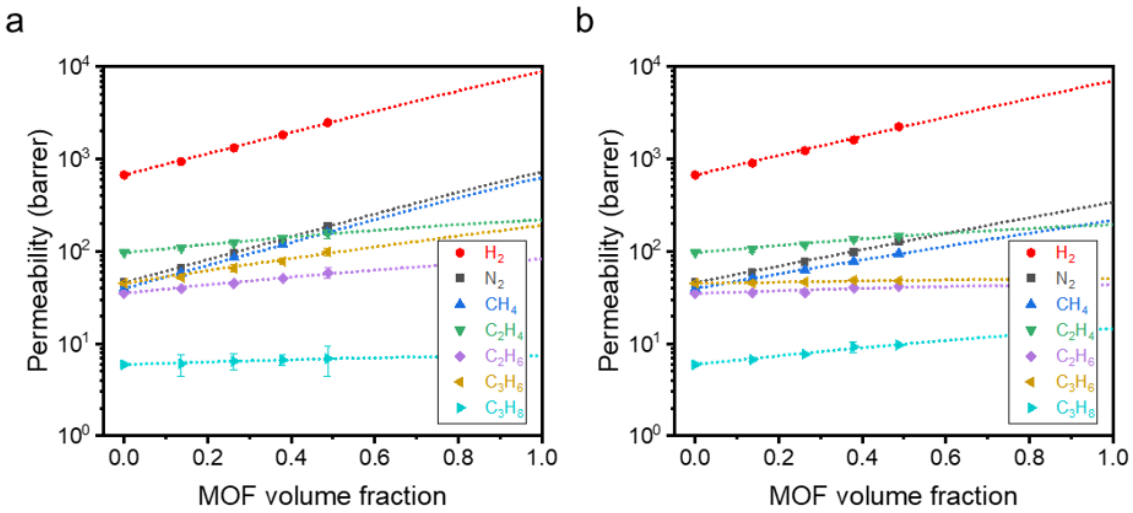


Figure 4-31: The fitted GPG model for (a) CubZ MMM and (b) RDZ MMM. Individual data points correspond to experimental results, with the plotted dashed lines indicating the fitted permeability model.

### 4.3.6 Temperature-dependent transport behavior analyses

Investigating permeation and sorption conducted across five different temperatures (7, 20, 35, 50, 65 °C) on 6FDA-DAM, 30 wt% CubZ MMM, and 30 wt% RDZ MMM samples, we studied the energetics and temperature dependence of permeation, sorption, and diffusion. To achieve a more accurate representation of diffusivity, particularly for larger gases that behave non-ideally, the corrected diffusivity of the membranes was calculated using the effective transport diffusivity ($D_t$) and the Darken equation, as given below:[140]

$$D_t(c) = D(c)\left(\frac{\partial \ln f}{\partial \ln c}\right)_T \tag{4.13}$$

In this equation, $D_t$ stands for transport diffusivity, $D$ denotes corrected diffusivity, $f$ is the fugacity of the gas, and $c$ represents the gas concentration.

First, we graphed $S$ and $D$ from all five temperatures against the compressibility measure (critical temperature, $T_c$) and gas size, respectively, using the measures from Table 4.9. The changes in both sorption and diffusion selectivity values were less pronounced upon MOF incorporation, particularly with CubZ. Furthermore, a

general trend of higher selectivity was observed with MOFs. This observation is consistent with the lower temperature dependence of the MOF phase compared to the polymer phase, aligning with the general trend of activation energy values being smaller in MMMs.

Table 4.10: Critical temperature and molecular diameter (van der Waals diameter) values for the studied probe gas molecules

| | $H_2$ | $N_2$ | $CH_4$ | $C_2H_4$ | $C_2H_6$ | $C_3H_6$ | $C_3H_8$ |
|---|---|---|---|---|---|---|---|
| Critical temperature, $T_c$ (K)* | 33.2 | 126.2 | 190.6 | 282.5 | 305.3 | 365.2 | 369.9 |
| Molecular diameter, d (Å)[32] | 2.76 | 3.13 | 3.25 | 3.59 | 3.72 | 4.03 | 4.16 |

*www.NIST.gov

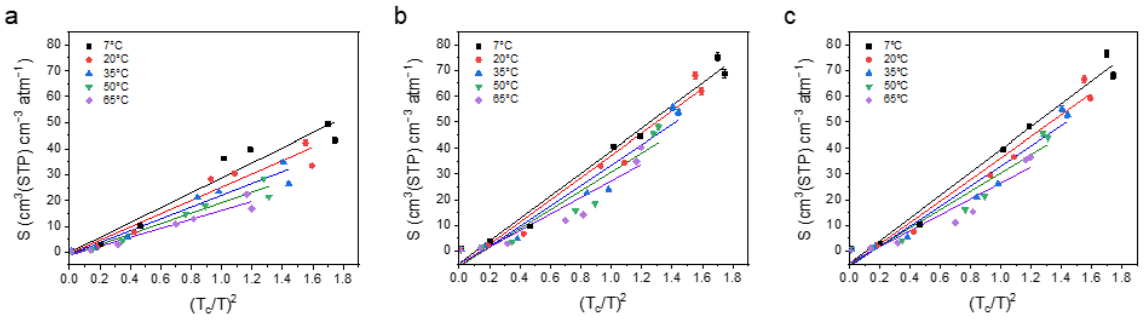


Figure 4-32: Sorption coefficient at approximately 1 bar pressure (where the permeation test was conducted) is depicted as a function of the unitless compressibility measure, $(T_c/T)^2$, for (a) 6FDA-DAM, (b) CubZ MMM, and (c) RDZ MMM. Each point represents experimental data and the superimposed lines illustrate the linear fit.

Table 4.11: The slope values derived from the plotted lines of Figure 4-32.

| Temperature (°C) | 6FDA-DAM | 30 wt% CubZ MMM | 30 wt% RDZ MMM |
|---|---|---|---|
| 7 | 28.8 | 43.7 | 44.2 |
| 20 | 25.7 | 43.0 | 41.7 |
| 35 | 22.9 | 39.5 | 39.0 |
| 50 | 20.4 | 36.7 | 35.6 |
| 65 | 17.5 | 32.2 | 31.1 |

To further understand these findings, we modeled the temperature-dependent sorption using the van't Hoff equation, as given below:

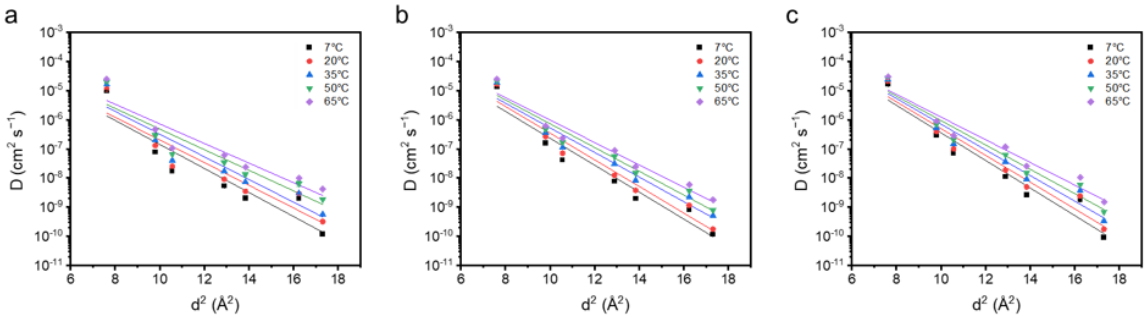


Figure 4-33: Corrected diffusion coefficient at approximately 1 bar pressure (matching the permeation test pressure) is depicted as a function of the molecular diameter squared, for (a) 6FDA-DAM, (b) CubZ MMM, and (c) RDZ MMM. Each point represents experimental data and the superimposed lines illustrate the linear fit.

Table 4.12: The slope values derived from the plotted lines of Figure 4-33

| Temperature (°C) | 6FDA-DAM | 30 wt% CubZ MMM | 30 wt% RDZ MMM |
|---|---|---|---|
| 7 | −0.95 | −1.06 | −1.09 |
| 20 | −0.90 | −1.05 | −1.06 |
| 35 | −0.89 | −0.97 | −1.01 |
| 50 | −0.81 | −0.94 | −0.96 |
| 65 | −0.77 | −0.88 | −0.89 |

$$S = S_0 \exp\left(\frac{-\Delta H_S}{RT}\right) \tag{4.14}$$

Here, $S_0$ represents the pre-exponential factor, while $\Delta H_s$ denotes the sorption enthalpy.

The activation energy of corrected diffusion can be similarly modeled using a van't Hoff type relationship:

$$D = D_0 \exp\left(\frac{-E_D}{RT}\right) \tag{4.15}$$

Here, $D$ represents corrected diffusivity, $D$ is the pre-exponential factor, and $E_D$ is the activation energy for corrected diffusion.

The temperature dependence of permeability also adheres to a similar relationship, as shown below:

$$P = P_0 \exp\left(\frac{-E_P}{RT}\right) \tag{4.16}$$

In this equation, $P_0$ is the pre-exponential factor, and $E_p$ is the activation energy of permeation.

In the study of diffusion energetics, Brandt's model has been widely adopted:[35, 91, 141]

$$E_D = cd^2 - f \tag{4.17}$$

where $c$ and $f$ are best-fit parameters and $d$ is molecular diameter of penetrants. Although this theory is restricted to light gas molecules where gas diameter is a good measure of penetrant size in terms of properties (usually up to methane), data set showed great fit ($R^2 > 0.95$) up to $C_2$ gases. The fit resulted in $\sqrt{f/c}$ value, representing the rough approximation of the average size of the free volume within the polymer matrix and the pores of the MOFs, the of 1.83, 2.37, and 2.41 for pure polymer, CubZ MMM, and RDZ MMM, respectively, in accord with the size order of hydrogen permeability. For $C_3$ gases it showed the concave to the gas size axis as reported.[35]

For many polymers, gas solubility coefficients over short ranges of penetrant critical temperature are well described by a linear relationship between the logarithm of sorption enthalpy square of those condensability measure. Although the enthalpy did not exhibit any noticeable trend (as depicted in Fig 4-34), it showed almost identical values between RDZ MMM and CubZ MMM. This observation implies that no clear sorption-based selection occurred in the transport studies with the gases we considered.

To probe Henry and Langmuir sorption independently, we applied the dual mode sorption (DMS) model. This model explores two equilibrium constants, $k_D$ and $b$, which also exhibit the same temperature dependence.[142]

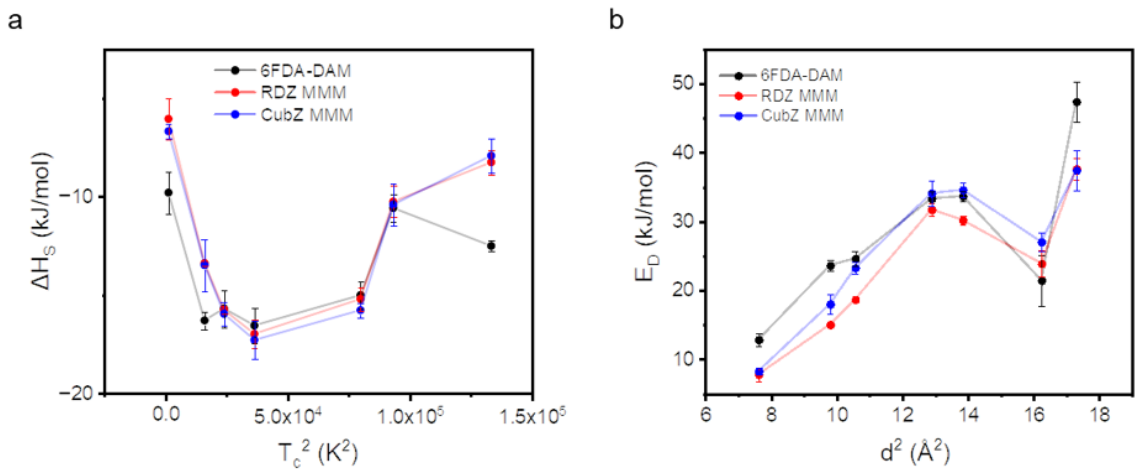


Figure 4-34: Gas transport energetics for 6FDA-DAM, 30 wt% RDZ MMM, and 30 wt% CubZ MMM are plotted as functions of relevant gas properties: (a) sorption enthalpy of samples as a function of gas compressibility (represented by squared critical temperature, $T_c$), and (b) activation energy of diffusion for the samples as a function of gas size (represented by squared molecular diameter, $d$).

$$k_D = k_{D,0} \exp\left(\frac{-\Delta H_D}{RT}\right) \tag{4.18}$$

$$b = b_0 \exp\left(\frac{-\Delta H_b}{RT}\right) \tag{4.19}$$

In these equations, $k_{D,0}$ and $b_0$ are pre-exponential factors (expressed in $cm^3(STP)$ $cm^{-3}$ $atm^{-1}$ and $atm^{-1}$, respectively), $\Delta H_D$ is the enthalpy of Henry's sorption (kJ/mol), and $\Delta H_b$ is the enthalpy of Langmuir sorption (kJ/mol).[99]

To further compare the relative effects of Henry and Langmuir sorption on total sorption, $k_D$ and $b$ values were plotted as a function of $T_c$ as below:

$$\ln(k_D) = A \times T_c + A' \tag{4.20}$$

$$\ln(b) = B \times T_c + B' \tag{4.21}$$

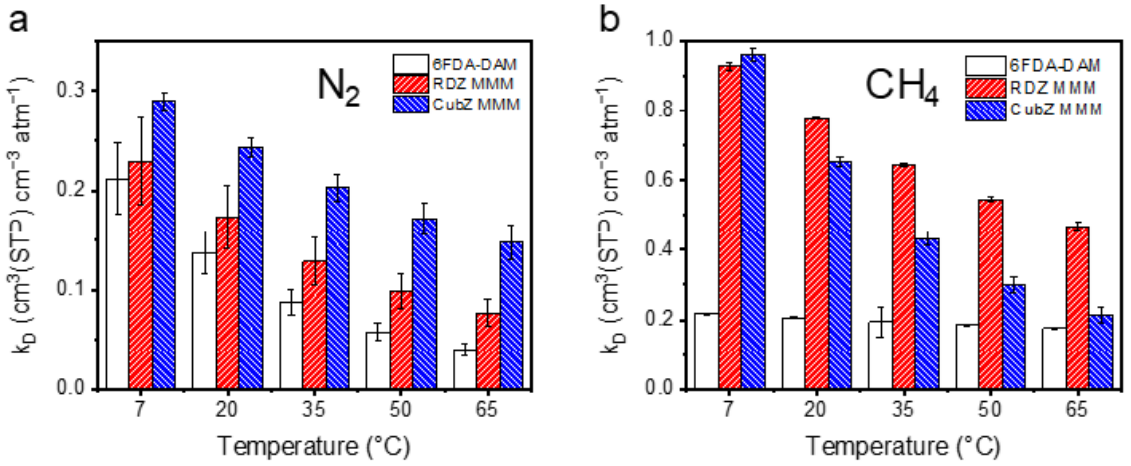


Figure 4-35: Henry sorption affinity, denoted as '$k_D$', for 6FDA-DAM, RDZ MMM, and CubZ MMM, presented for (a) $N_2$ and (b) $CH_4$.

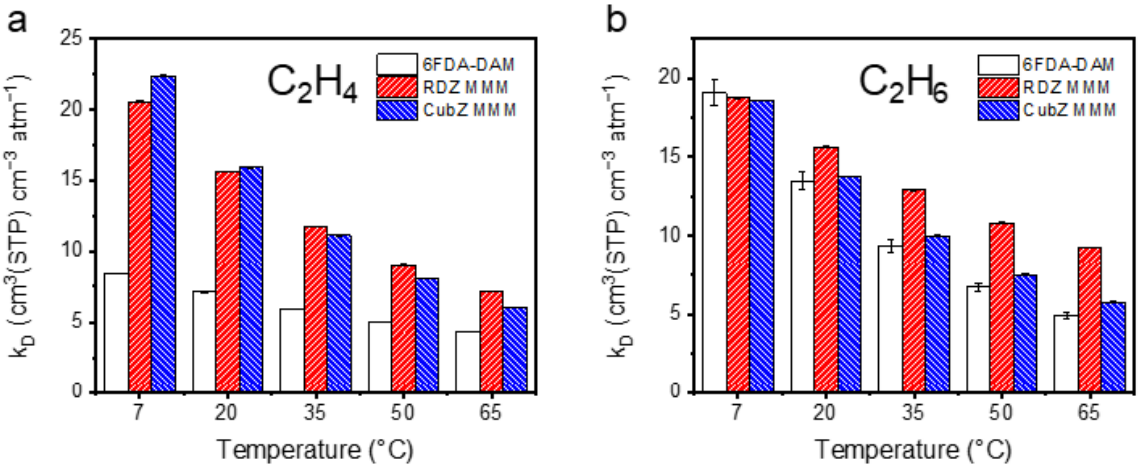


Figure 4-36: Henry sorption affinity, denoted as '$k_D$', for 6FDA-DAM, RDZ MMM, and CubZ MMM, presented for (a) $C_2H_4$ and (b) $C_2H_6$.

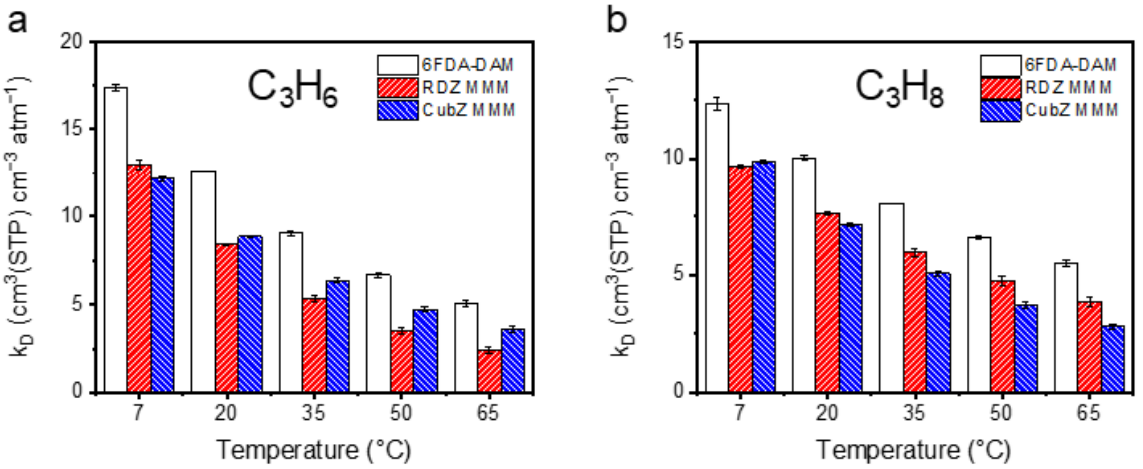


Figure 4-37: Henry sorption affinity, denoted as '$k_D$', for 6FDA-DAM, RDZ MMM, and CubZ MMM, presented for (a) $C_3H_6$ and (b) $C_3H_8$.

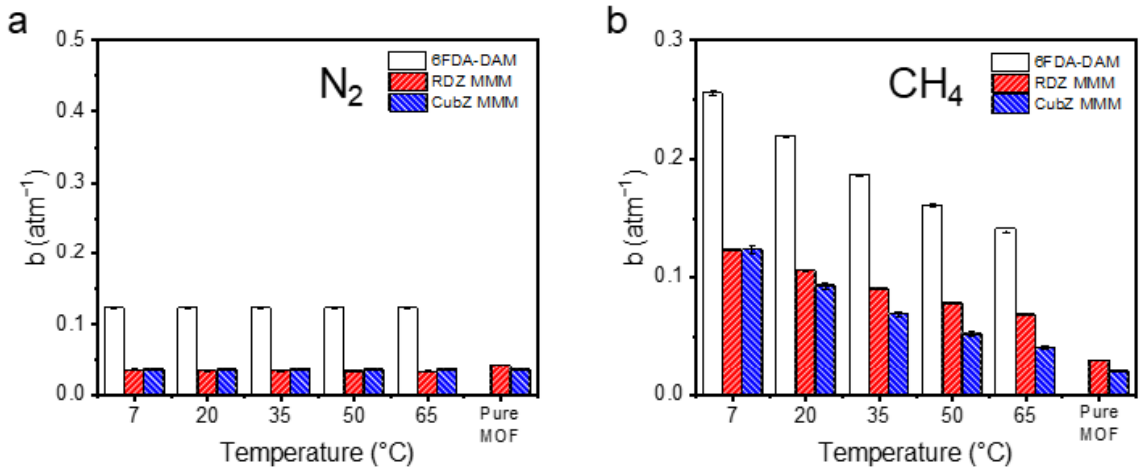


Figure 4-38: Langmuir sorption affinity, denoted as '$b$', for 6FDA-DAM, RDZ MMM, CubZ MMM, and pure MOFs presented for (a) $N_2$ and (b) $CH_4$.

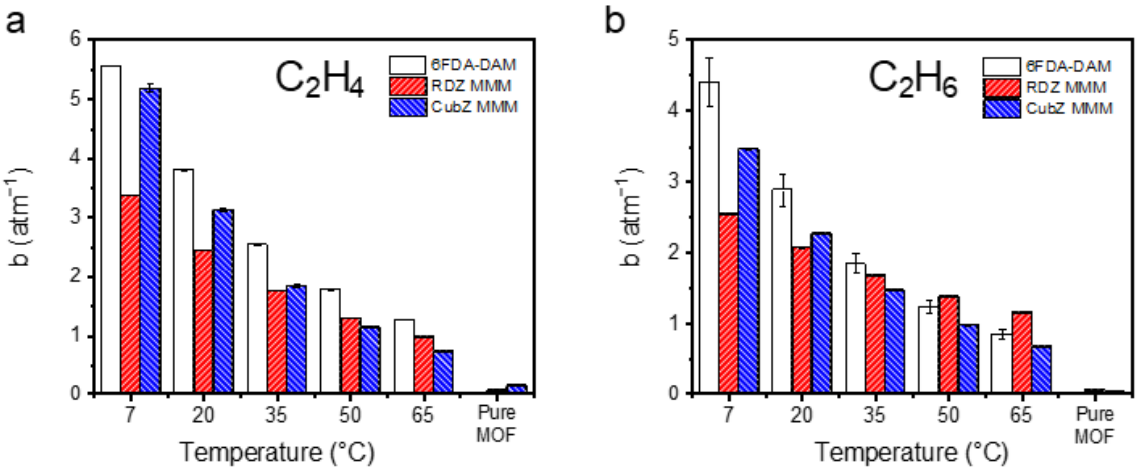


Figure 4-39: Langmuir sorption affinity, denoted as $'b'$, for 6FDA-DAM, RDZ MMM, and CubZ MMM, presented for (a) $C_2H_4$ and (b) $C_2H_6$.

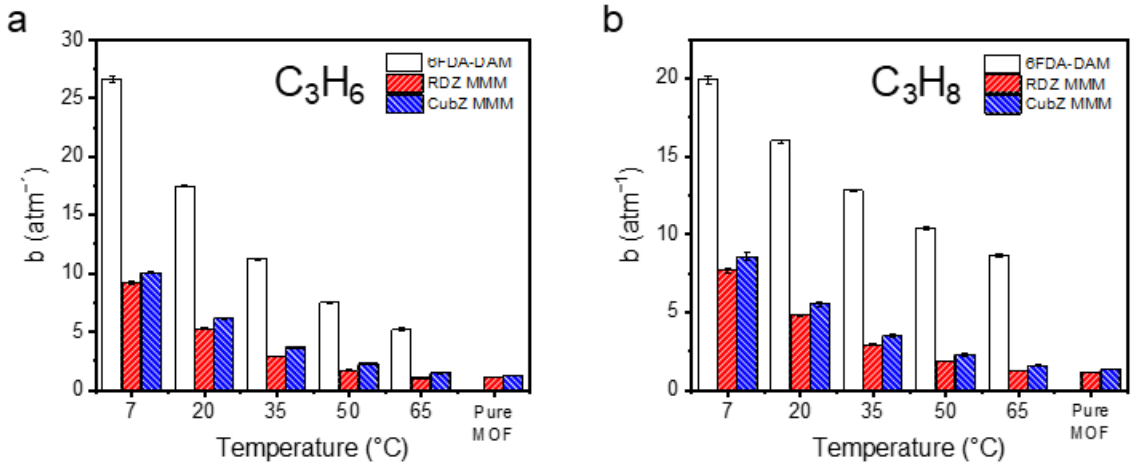


Figure 4-40: Langmuir sorption affinity, denoted as $'b'$, for 6FDA-DAM, RDZ MMM, and CubZ MMM, presented for (a) $C_3H_6$ and (b) $C_3H_8$.

where *A, A', B*, and *B'* are the best-fit parameters are the best-fit parameters.[99]

Table 4.13: The slope values ($A$) derived from the plotted lines of Figure 4-44.

| Temperature (°C) | 6FDA-DAM | 30 wt% CubZ MMM | 30 wt% RDZ MMM |
|---|---|---|---|
| 7 | 0.021 | 0.016 | 0.017 |
| 20 | 0.021 | 0.016 | 0.017 |
| 35 | 0.021 | 0.015 | 0.016 |
| 50 | 0.021 | 0.015 | 0.016 |
| 65 | 0.021 | 0.015 | 0.016 |

Henry sorption is often referred to as "equilibrium sorption," where the penetrant

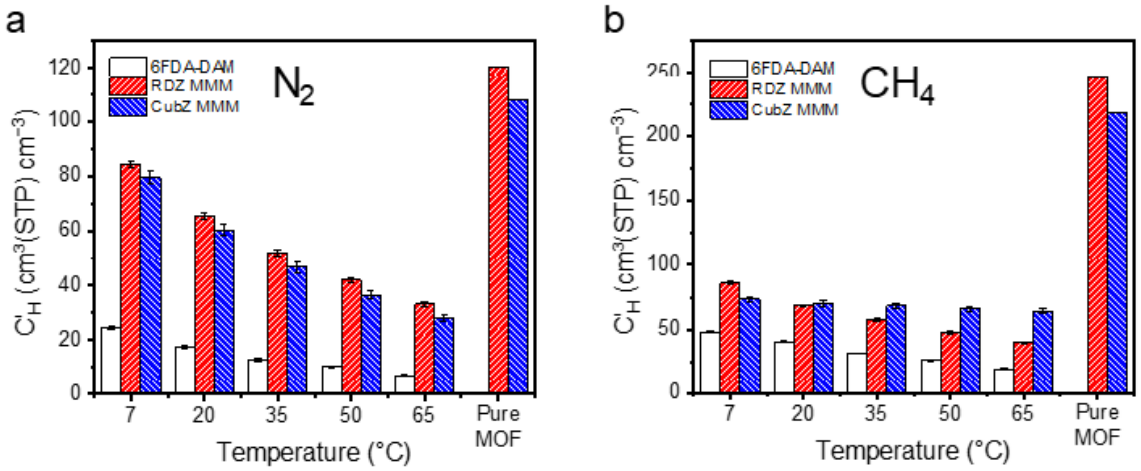


Figure 4-41: Langmuir sorption site, denoted as '$C_H$', for 6FDA-DAM, RDZ MMM, CubZ MMM with pure RDZ and CubZ presented for (a) $N_2$ and (b) $CH_4$.

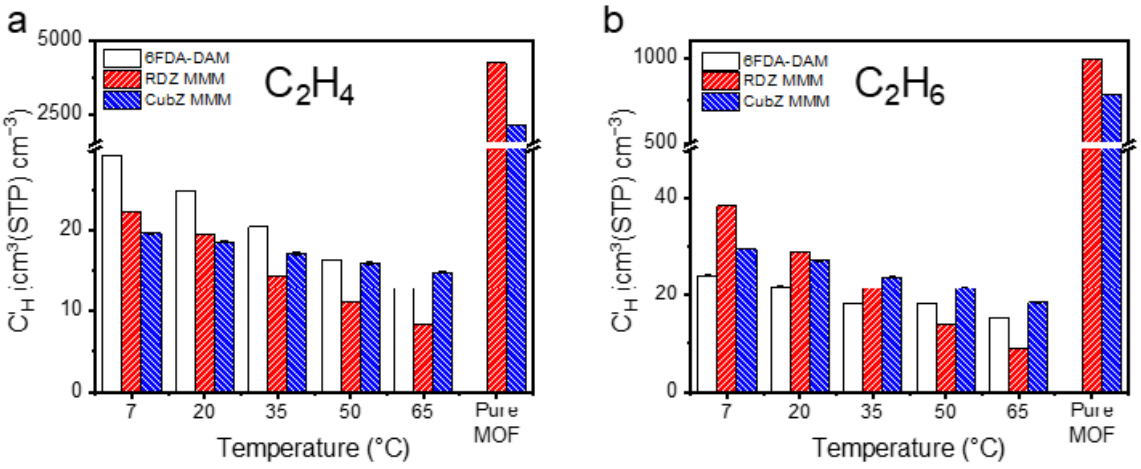


Figure 4-42: Langmuir sorption site, denoted as '$C_H$', for 6FDA-DAM, RDZ MMM, CubZ MMM with pure RDZ and CubZ presented for (a) $C_2H_4$ and (b) $C_2H_6$.

Table 4.14: The slope values ($B$) derived from the plotted lines of Fig 4-45.

| Temperature (°C) | 6FDA-DAM | 30 wt% CubZ MMM | 30 wt% RDZ MMM |
|---|---|---|---|
| 7 | 0.023 | 0.024 | 0.023 |
| 20 | 0.021 | 0.022 | 0.022 |
| 35 | 0.020 | 0.021 | 0.020 |
| 50 | 0.019 | 0.019 | 0.018 |
| 65 | 0.017 | 0.017 | 0.016 |

is assumed to be fully dissolved into the polymer matrix. $k_D$ for individual gases is influenced by interactions between the penetrant and polymer, similar to mixing processes in regular solution theory. Hence, within the dual-mode sorption model,

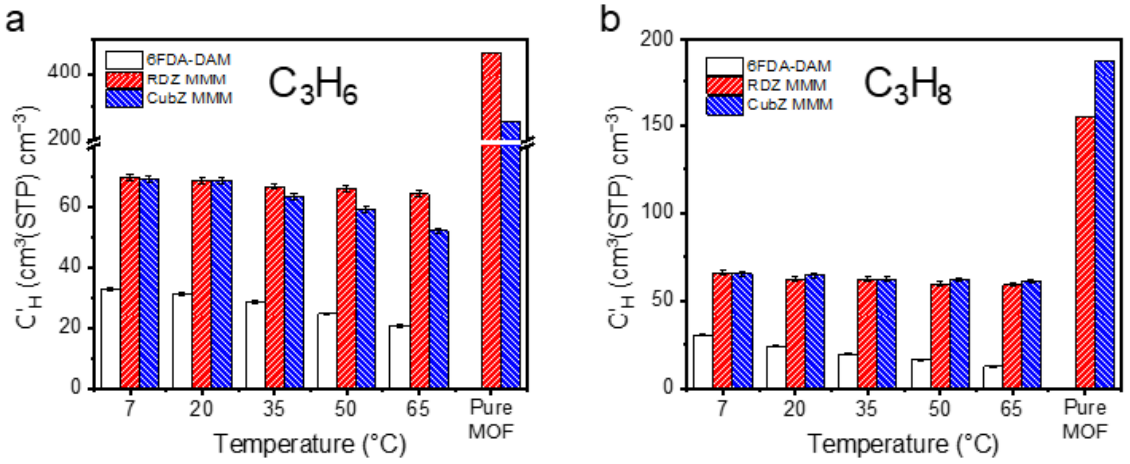


Figure 4-43: Langmuir sorption site, denoted as '$C_H$', for 6FDA-DAM, RDZ MMM, CubZ MMM with pure RDZ and CubZ presented for (a) $C_3H_6$ and (b) $C_3H_8$.

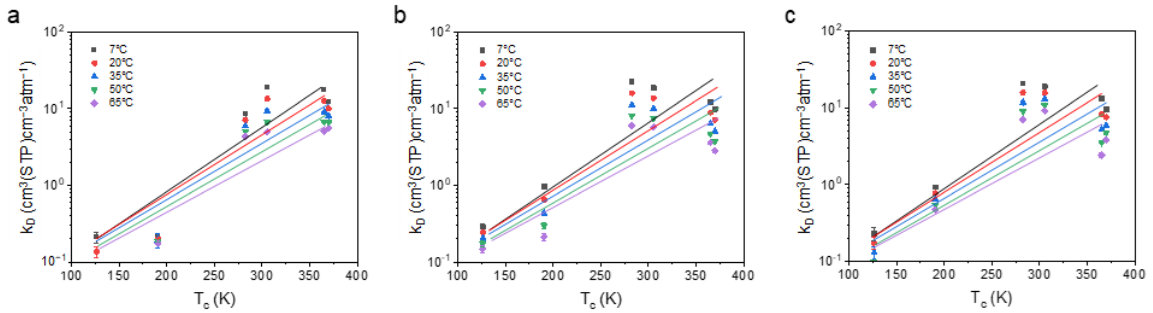


Figure 4-44: Semi-log plot of Henry's sorption affinity, represented as '$k_D$', and critical temperature, $T_c$, for (a) 6FDA-DAM, (b) CubZ MMM, and (c) RDZ MMM. Each point indicates experimental data, with a superimposed line representing the linear fit.

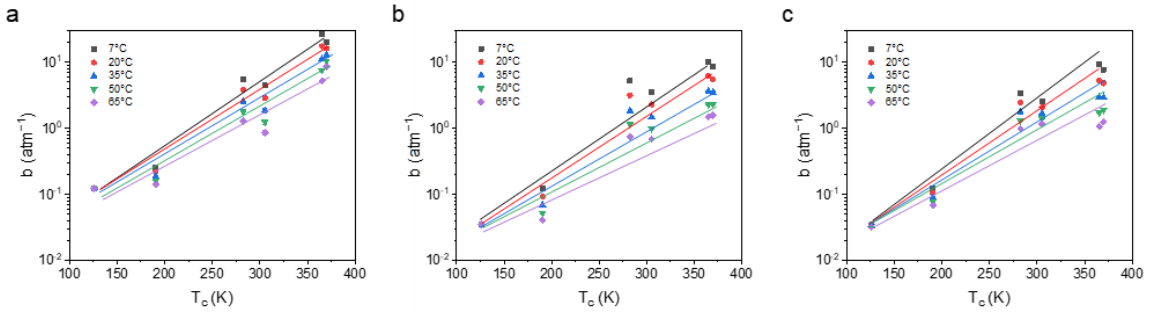


Figure 4-45: Semi-log plot of Langmuir's sorption affinity, represented as '$b$', and critical temperature, $T_c$, for (a) 6FDA-DAM, (b) CubZ MMM, and (c) RDZ MMM. Each point indicates experimental data, with a superimposed line representing the linear fit.

incorporating MOF seems to enhance Henry's sorption selectivity (denoted by a lower slope, $A$), as indicated in Fig 4-30. This trend could be attributed to the increased backbone stiffness inferred from the higher $T_{\mathrm{g}}$ of MMMs, leading to an elevated enthalpic penalty. It might also explain the lower $A$ value (indicating higher Henry sorption selectivity) in CubZ MMM, which exhibited a slightly higher $T_g$ than RDZ MMM. Notably, non-linearity increased significantly with MOFs incorporation, likely because MOFs only exhibit Langmuir sorption, leading to larger deviations for more compressible gases.

Langmuir sorption, also known as "saturated sorption," takes place when the penetrant occupies specific sites on the polymer free volume or MOF pores, often visualized as a monolayer. Contrary to Henry sorption, Langmuir sorption is determined by both $b$ and the $C_H$' term. The parameter $b$ for individual gases is impacted by the interactions between the penetrant and specific sorption sites, reflecting the relative surface adsorption to desorption rates of the penetrant onto the sorption site surface. With the introduction of MOFs, the analysis becomes more complex as both parameters are influential. As illustrated in Fig 4-39, the $b$ trend is opposite to that of $k_D$; pure polymer exhibits the highest selectivity (lower $B$), implying that the MOF phase has less Langmuir sorption selectivity.

Next, the parameter $C_H{}'$ are closely correlated with the volumes available for penetrants to be adsorbed such as free volume of polymer and pores of MOFs, which has a large impact on diffusion-related properties. Owing to the significantly higher number of Langmuir sorption sites in pure MOFs, all MMMs demonstrated larger $C_H{}'$ values compared to the pure polymer, as depicted in Fig 4-36–4-38. While the precise relationship of $C_H{}'$ with different gases remains unclear, unlike the relationships with $b$ and $k_D$, a distinct trend emerges when comparing the $C_H{}'$ values of pure components of MMMs (polymer vs. MOF) and the MMMs themselves. In the case of nitrogen, using the volume ratio derived from the pure component $C_H{}'$ values resulted in the measured $C_H{}'$ of the MMMs. The discrepancy between these values was minor, with errors of just 1.08% and 1.00% for the CubZ and RDZ MMM samples, respectively. When considering methane, however, the calculation using the

pure component volume ratio overestimated the measured MMM values by 52.6% and 52.0%. For $C_2$ gases, this trend became more pronounced, with the overestimation reaching between 91.9% and 97.8%. Yet, when examining propane, this deviation fell again to 12.1% and 8.6%. This pattern of increasing deviation with the size of the gas molecules suggests a decrease in the number of available Langmuir sorption sites on the MOF phase when introduced in polymer phase. Propane appeared to exhibit a lower deviation, potentially due to the pure MOFs having a substantially higher resistance to larger gas molecules already. Despite the clear trend for each sorption mode, their directions are opposite resulting in insignificant difference between samples in dual-mode sorption energetic as previously shown in Figure 4-49c and f.

One more thing to note is that the variance of '$A$' between polymer and MMMs is substantial, whereas the difference between two MMMs is relatively invariant. Under varying temperatures, '$A$' changes insignificantly (up to 7.8% change), while '$B$' shows a considerable change (up to 32%). This implies that Langmuir sorption contributes most to the temperature dependence in this case, and a virtually identical trend is observed between RDZ MMM and CubZ MMM.

## 4.4 Results and Discussion

### 4.4.1 Fabrication and Characterization of MOFs and MMMs

Adhering to the methodologies outlined in SI (Section 4.3.1), selective synthesis of rhombic dodecahedron ZIF-8 (RDZ) and cubic ZIF-8 (CubZ) particles, each approximately 100 nm in size, was synthesized. The syntheses exclusively produced the desired shapes, terminated by {110} and {100} facets, respectively. RDZ, the most stable polymorph of ZIF-8, was achieved without any modulator, while CubZ synthesis employed CTAB, a capping agent modulator that selectively adheres to {100} facets, thus resulting in {100} facet-terminated cubes.[102] A comprehensive examination of over 200 particles confirmed the surface areas and volumes of RDZ and CubZ to be statistically indistinguishable within the error margins (Fig 4-1, 4-2 and

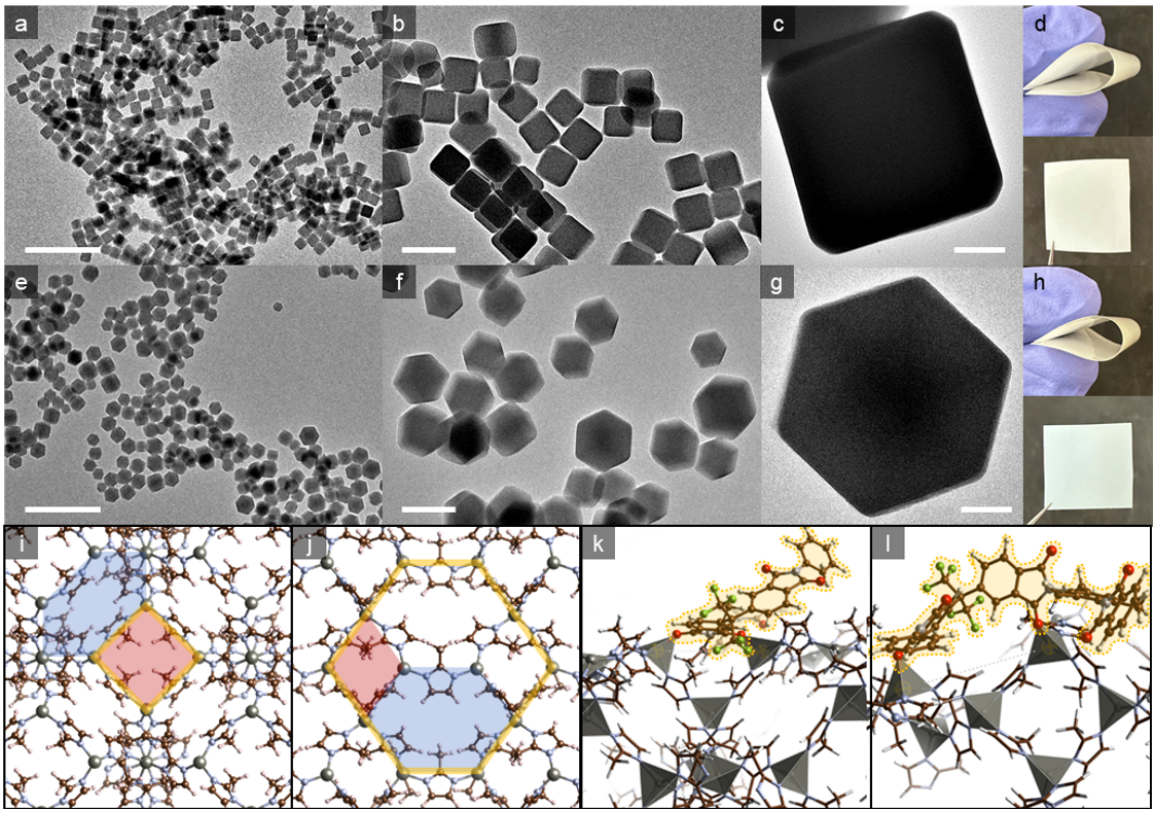


Figure 4-46: Transmission Electron Microscopy (TEM) representations of Zeolitic Imidazolate Frameworks (ZIF-8): (a-c) showcase cubic ZIF-8 (CubZ) while (e-g) exhibit rhombic dodecahedron ZIF-8 (RDZ). Images of Mixed Matrix Membranes (MMMs) incorporating 40 wt% of CubZ and RDZ are illustrated in (d) and (h), respectively. Surface schematics provided in (i) and (j) reveal the structural geometry of CubZ and RDZ: 6-membered rings (6MRs) denoted in blue and 4-membered rings (4MRs) denoted in red. The {100} facet has a 4MR and the {110} facet has a large six-membered ring in the plane of the surface as denoted with a yellow outline. (k) and (l) present optimized polymer coordination (depicting one monomer residues) with the {100} and {110} facets, respectively, highlighting respective binding energies of –398.5 and –305.4 kJ/mol. For clarity, zinc is represented as tetrahedra, and the monomer is depicted using a ball-and-stick model contoured with orange, with F in green, O in red, and C in brown; hydrogens are omitted for clarity. Interacting sites are marked with yellow (zinc) and red (oxygen) circles. Scale bars correspond to 1 $\mu$m for (a) and (e), 200 nm for (b) and (f), and 30 nm for (c) and (g).

Table 4.1).

An examination of the physicochemical and sorption properties of the as-synthesized MOFs revealed striking similarities. As depicted in Fig 4-3, RDZ and CubZ both exhibit the identical crystalline phase compared to that of simulated ZIF-8. Surface areas for both samples, computed from 77 K $N_2$ physisorption isotherms (Fig 4-4), were statistically equivalent, and consistent with the commercial ZIF-8.[143] Pure gas sorption isotherms at 35 °C, encompassing $H_2$, $N_2$, $CH_4$, $C_2H_4$, $C_2H_6$, $C_3H_6$, and $C_3H_8$, followed a pattern similar to previous studies on ZIF-8 (Fig 4-17).[16] The congruence of all these characterizations show the similar properties of RDZ and CubZ, including interactions between the examined gas molecules and MOF particles.

To observe the effect of facet terminations in MMMs, CubZ and RDZ MMMs were fabricated using 6FDA-DAM as the polymer matrix, because it is known to synergistically improve size-sieving properties with ZIF-8, also known as 'polymer-sieve matching.'[63] Cross-sectional SEM images of all MMM samples (Fig 4-6 and 4-7) displayed a uniform particle distribution without discernible defects. This observation is corroborated by energy-dispersive X-ray spectroscopy (EDX) data (Fig 4-8 and 4-9), which reveals a uniform distribution of ZIF-8 (represented by Zn) and polymer (represented by F). Thermogravimetric analysis (TGA) further verifies that the concentrations of MOFs in the MMMs deviate by less than 2% from the target loadings, as inferred from the weight of calcinated ZnO (Fig 4-10 and Table 4.2).

### 4.4.2 Facet-Specific MOF-Polymer Interactions in MMMs

Even though CubZ and RDZ share similarities in their physicochemical characteristics, potentially influencing MOF–polymer interactions. As illustrated in Fig 4-46i and j, the {110} facet, characterized by its large six-membered ring (highlighted in yellow) on the surface plane, suggests superior accessibility for diluents (Table 4.5).[124]

To delve into MOF–polymer interaction further, an array of experimental techniques were employed: differential scanning calorimetry (DSC), Fourier-transform infrared spectroscopy (FTIR), magic-angle spinning (MAS) solid-state nuclear mag-

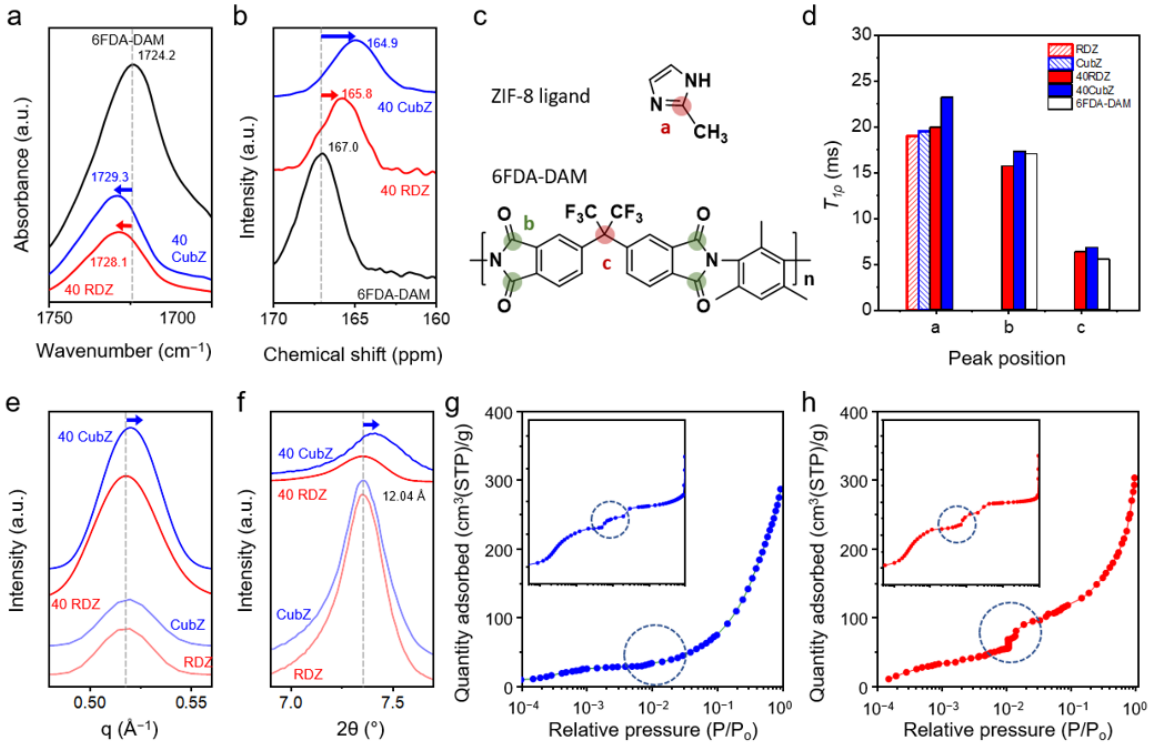


Figure 4-47: Zoomed-in C=O peak in (a) FTIR spectra and (b) $^{13}$C NMR spectra of 6FDA-DAM pure polymer and 40 wt% MMM composites. (c) chemical formula of the ZIF-8 ligand and 6FDA-DAM, and labeled peaks for $^{13}$C NMR spectra and (d) their derived $T_{1\rho}$ results. Zoomed-in (e) wide angle x-ray scattering (WAXS) spectra and (f) XRD spectra of CubZ, RDZ, and their corresponding 40 wt% MMMs. Semi-logarithmic plot of $N_2$ physisorption isotherms at 77 K for (g) 40 wt% CubZ MMM, with an inset of pure CubZ MOF powder, and (h) 40 wt% RDZ MMM, with an inset of pure RDZ MOF powder. The x-axis range is consistent across all plots, and the inset y-scale corresponds to that of Fig 4-5

netic resonance (SS-NMR), wide-angle X-ray scattering (WAXS), X-ray diffraction (XRD), and $N_2$ physisorption isotherms. The DSC study, determining the glass transition temperature ($T_g$) of the pure polymer and MMMs, revealed an escalation in $T_g$ with increasing MOF loading. Notably, CubZ MMMs presented a higher $T_g$ increase (Table S3), suggesting a greater restriction on polymer chain mobility.

The application of FTIR and SS-NMR (Fig 4-47a, b, **??**) also showed discernible alterations upon MOF integration. The blueshift in C=O resonances, evidenced by a decrease in chemical shift for NMR and an increase in wavenumber for FTIR spectra, with MOF loading suggests a strengthening of the MOF–polymer interaction.[139, 140] This effect was more evident in CubZ MMM, implying a stronger interaction in this system. SS-NMR was further studied to measure spin-lattice relaxation times in the rotating frame ($T_{1\rho}$), where larger values indicate slower molecular motion around the assigned carbon.33 Pure polymer, MOF, and 40 wt% MMMs were tested, and the 40 wt% CubZ MMM showed the longest relaxation times across all peaks (Fig 4-47d), aligning with the aforementioned observations where MOF–polymer interaction were more robust in CubZ MMM.

The observations from WAXS and XRD spectra further corroborated findings from FTIR and SS-NMR. These techniques demonstrated matching peak locations for pure MOFs and RDZ MMMs but notable small reductions (about 1%) in d-spacings for CubZ MMMs (Fig 4-47e, f, 4-4, 4-12). Similarly, $N_2$ physisorption analysis conducted at 77 K on both pure MOFs and MMMs gave insight into the gate opening phenomena of ZIF-8 phase. The charecteristic step-wise increase in adsorption near 0.01 $P/P_0$ in pure ZIF-8[74] demonstrated the presence of ZIF-8 gate opening phenomena in both CubZ and RDZ in their pristine powder forms (Fig 4-47g and h). Intriguingly, this feature was absent in CubZ MMM upon integration into the polymer matrix, although it was retained in RDZ MMM. These observations imply that MOF–polymer interactions lead to a marked suppression of ligand flexibility exclusively in the CubZ MMMs.

Polymer–facet interactions were explored using DFT calculations, premised on previously established motifs for polymer adsorption.[133] Through this methodol-

ogy, the interaction of the 6FDA-DAM and different facets was investigated, revealing substantial differences in the calculated binding energy values, with the {110} and {100} facets respectively showing –305.4 and –398.5 kJ/mol. These findings highlight a stronger interaction between CubZ and the 6FDA-DAM polymer. The origins of the stronger interphase confinement in CubZ MMM could be attributed to an optimal binding between CubZ and functionality in the 6FDA-DAM structure (Fig 4-46k and l). The monomer of 6FDA-DAM has two phthalimides segments (Fig 4-47c), each with two carbonyl groups separated by 4.63 Å. These carbonyl groups are prone to electronic interaction with ZIF-8.[139, 140] However, in RDZ slab structures, the proximal positioning of the linker between two zinc metal sites prevents simultaneous bonding of both carbonyl groups from the same phthalimide to the metal sites. In contrast, in CubZ slab sturctures, 6MR apertures exhibit a steeper tilt of 54°, compared to the mere 33° observed in the RDZ surface. This pronounced tilt in CubZ reduces the minimal distance between non-adjacent metal sites to 8.5 Å, enabling the simultaneous attachment of the carbonyl groups from the same phthalimide to the surface (Fig 4-46k). This strong bonding interaction lessens the distance between the zinc metal sites to approximately 7.7 Å.

Drawing from both experimental characterization and DFT calculations, it is inferred that the MOF–polymer interactions are sufficiently stronger for CubZ MMM, which can be ascribed to the unique aperture configuration on the surface facilitating stronger binding. This finding implies that the {110} facet provides better accessibility for gas molecules, while the {100} facet offers greater resistance. Importantly, these distinctions were observed only in the MMM context, highlighting the facet-specific properties unique to MOF-based composites.

### 4.4.3 Gas Separation Performance

ZIF-8 is traditionally recognized for its remarkable propylene/propane ($C_3H_6/C_3H_8$) separation capacity.[26, 15, **?**, 103] This performance is mainly attributed to an effective diffusivity "cut-off" between 4.0–4.2 Ådespite the smaller crystallographic pore aperture of 3.4 Å.[16] This phenomenon, known as the "gate opening" effect, fa-

cilitates the transport of molecules larger than pores via the ligand's methyl group rotation.[?] However, it is noteworthy that previous studies have predominantly focused on {110} facets (i.e., RDZ), which represent the most thermodynamically stable polymorph of ZIF-8.[144]

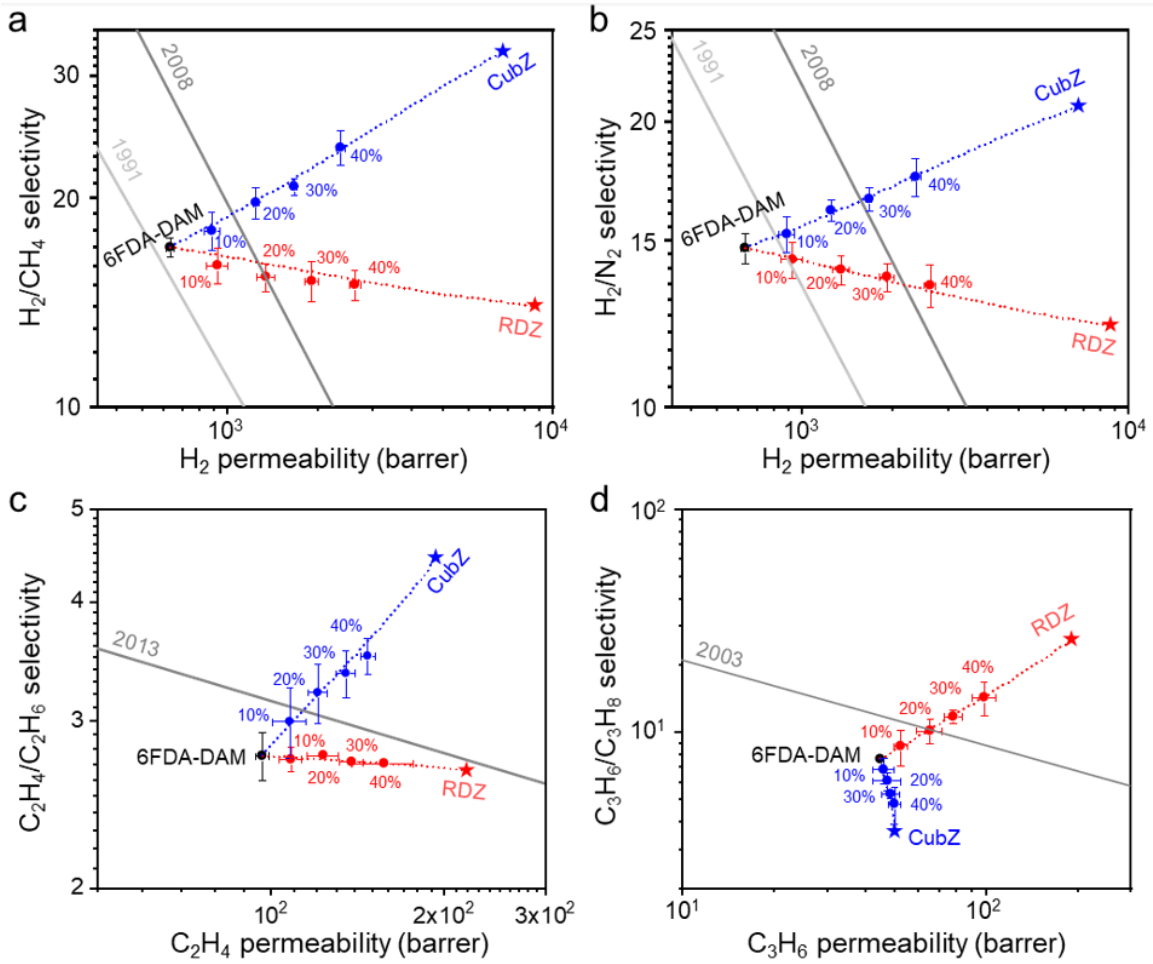


Figure 4-48: Gas permeability–selectivity performance of pure 6FDA-DAM and CubZ and RDZ MMMs with various MOF loadings (10, 20, 30, and 40 wt%) along with theoretical projections (dashed lines with stars for pure MOF phase predictions) for (a) $H_2/CH_4$ separation, (b) $H_2/N_2$ separation, (c) ethylene/ethane separation, and (d) propylene/propane separation. The upper bounds for all gas pairs are also included in the plots.[17, ?, 19, 20]Arrows represent increase in MOF loading.

Building on this understanding, pure-gas permeation tests were conducted on 6FDA-DAM polymeric films, CubZ MMMs, and RDZ MMMs, each incorporating different MOF loadings (10, 20, 30, and 40 wt%) (Fig 4-48). RDZ MMMs, in accord with the aforementioned properties of ZIF-8, demonstrated excellence in $C_3$

($C_3H_6/C_3H_8$) separation, increasing both selectivity and permeability with increasing MOF loadings. In contrast, CubZ MMMs did not exhibit the same "gate opening" effect in $C_3$ separation. Instead, the inclusion of CubZ led to decreased selectivity with a relatively smaller enhancement in permeability, highlighting increased transport resistance for $C_3$ gases. However, CubZ MMMs outperformed in selectivity for lighter gas separations, such as $H_2/N_2$, $H_2/CH_4$, and even $C_2H_4/C_2H_6$, one of the most challenging separations due to their structural and physical similarities.[23]

These trends were explored further by deconvoluting permeation properties into sorption and diffusion coefficient per the sorption–diffusion model.[25] As shown in Fig 4-29, marked differences in the diffusion coefficients elucidate the varying gas separation performance for each sample, while gas sorption coefficients for two MMMs demonstrated comparable behavior. This implies that the different separation performance observed between CubZ and RDZ MMMs primarily stems from alterations in molecular sieving diffusion selectivity.

### 4.4.4 Temperature Dependence and Energetics of Gas Transport

A temperature study employing MMMs with CubZ and RDZ at 30 wt% across five different temperatures (7, 20, 35, 50, 65 °C) was executed to elucidate the temperature dependence and energetics of transport processes, which demonstrated a similar trend to the prior MOF loading study. As delineated in Fig 3, more pronounced selectivity enhancement with decreasing temperature trends were observed for $H_2$ separations in the case of CubZ MMM. However, the reduction in $H_2$ permeability remained similar across all three samples, which shows the selectivity is mainly attributed to slower $N_2$ and $CH_4$ transport. Regarding $C_2$ separation, although CubZ MMM shows highest performance throughout the temperatures, no substantial difference in slope was observed, implying the temperature dependence for this gas pair is similar for the samples. For $C_3$ separation, a significantly steeper boost was observed in RDZ MMM due to a notable increase in selectivity and a lesser decline in permeability.

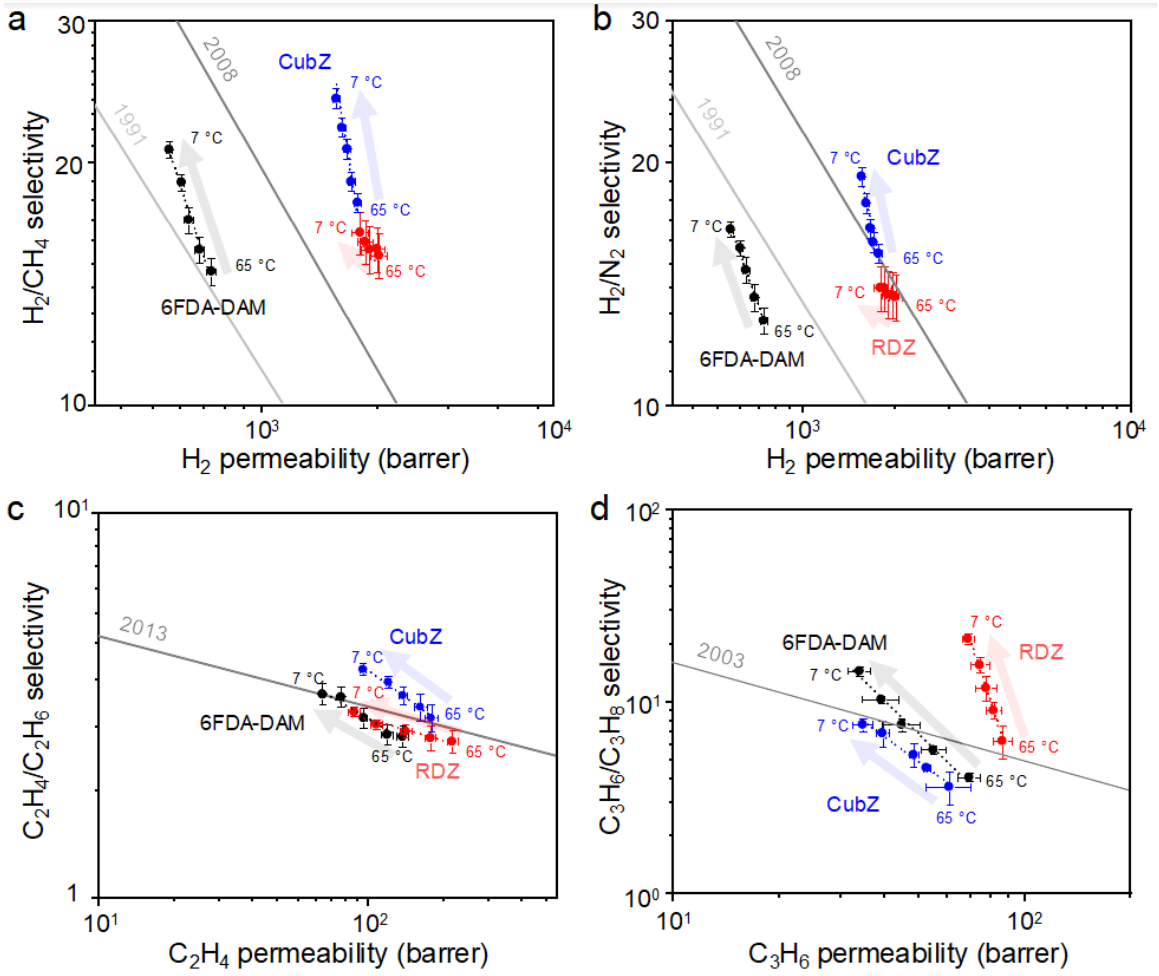


Figure 4-49: Gas permeability-selectivity performance plots of a pure 6FDA-DAM polymeric film and 30 wt% CubZ MMM and 30 wt% RDZ MMMs with various temperatures (7, 20, 35, 50, and 65 °C) along with Arrhenius fit (dashed lines) for (a) $H_2/CH_4$ separation, (b) $H_2/N_2$ separation, (c) ethylene/ethane separation, and (d) propylene/propane separation. The upper bounds for all gas pairs are also included in the plots.[17, 18, 19, 20] Arrows represent decrease in temperature.

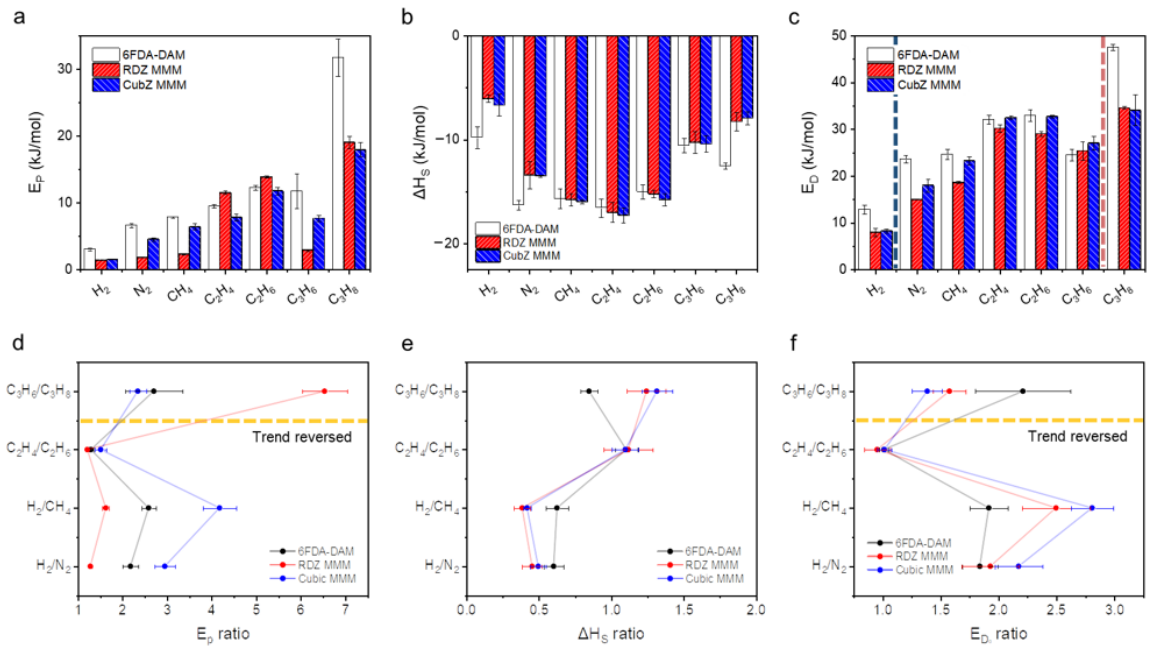


Figure 4-50: Gas transport energetics comparison of pure 6FDA-DAM and 30 wt% CubZ MMM and 30 wt% RDZ MMMs: (a) effective activation energy values for permeation, (b) sorption enthalpy, and (c) effective activation energy values for diffusion. For enhanced clarity, the ratios of the energetics for different gas pairs are plotted in (d-f), corresponding to (a-c), respectively

To investigate the underlying mechanisms related to separation performance, the effective activation energy of permeation, enthalpy of sorption, and activation energy of diffusion were calculated using van't Hoff's relationships, detailed in Section S6. First, comparing activation energy of permeation as shown in Fig 4-50a and d, CubZ MMM showed a significant increase in selectivity ($E_p$ ratio) for $H_2$-based separations in comparison with the base polymer. The increase was considerably less significant for $C_2$ separations, and a decrease in selectivity was observed for $C_3$ separation. On the other hand, RDZ MMM demonstrated a prominent boost for $C_3$-based gases only and showed smaller selectivity for small gases, with a pronounced decrease for $H_2$ separations. Interestingly, these findings align with the permeability selectivity trend observed with MOF loading in Fig 4-48.

When comparing the enthalpy of sorption as shown in Fig 4-50b and e, the only difference in properties was observed between the base polymer and MMMs. This finding can be attributed to the existence of two distinct phases: ZIF-8 and polymer. Sorption enthalpy of CubZ and RDZ MMMs was found to be within the error bars for all gas pairs tested, suggesting that sorption-based selection was not the primary factor influencing different gas separation trend in between MMMs.

To gain further insights, dual-mode sorption analysis was performed (Section 4.3.4 and 4.3.6) to deconvolute the sorption into Henry and Langmuir modes. Henry mode is an "equilibrium" sorption mode analogous to dissolution into liquids, and Langmuir mode is a "surface" sorption mode analogous to site-specific binding for classical adsorbants, respectively.47 For both modes, the affinity coefficient differed little in between MMMs, and the main difference between MMMs and pure polymer arise from different Henry sorption where polymer showed the highest selectivities due to the low $k_d$ of MOF phase.

The activation energy of diffusion ($E_D$) showed similar trends for MMMs as the activation energy of permeation. Of note, there was a significant difference in the ratio of activation energies of diffusion for $C_3$ separation compared to that of other gas pairs considered (Fig 4-50f, yellow dashed line), confirming that the main separation mechanism is diffusion selectivity. Indeed, these findings agree with the molecular-

level interpretation of suppressed ligand rotation in the CubZ MMM relative to that in the RDZ MMM result in enhanced separation performance for CubZ when separating molecules smaller than propylene and propane. In general, the CubZ MMM exhibited higher diffusion energy barriers for all gases compared to those for the RDZ MMM. Activation energies of diffusion for $H_2$ were within the range of measurement uncertainties for both MMMs, but there were notably higher activation energies for $N_2$ and $CH_4$ in CubZ MMM (Fig 4-50c, navy dashed line). Based on Brandt model, plotting as a function of gas molecule size (Fig 4-35b, Section 4.3.6) provides a rough measure of free volume distribution and hence size-sieving capabilities of a membrane material. As expected, the slope of these plots was smallest for polymer followed by CubZ MMM and RDZ MMM, consistent with the selectivity trend up to methane where the model is valid. The propylene diffusion activation energy was markedly smaller for RDZ MMMs, while values for propane were similar for both MMMs (Fig 4-50c, red dashed line).

From this energetic study, clear mechanistic insights could be gleaned on the distinct gas transport performance of MMMs that are formed with unique facet terminations. More specifically, the superior $H_2$ and $C_2$ separation performance for CubZ MMM, and the enhanced $C_3$ separation of RDZ MMM could be explained. By extension, performance trends as a function of temperature provide a useful set of data that could enable more effective process modeling in predicting performance of MOFs with unique facets. This quantitative gas transport energetic study reveals that permeation activation energy is mainly attributed to the diffusion energetics.

## 4.5 Conclusion

This study investigated the facet-specific effect of MOFs in nanocomposite for the first time. We showcased gas transport properties of MMMs incorporating RDZ and CubZ, where pure MOF samples exhibited virtually identical interactions with tested gas molecules. Surprisingly, interaction between the MOF and polymer phases was stronger in CubZ MMMs impacting its MOF phase ligand flexibility, playing a sig-

nificant role in the observed gas separation performance. The gas transport analysis of corresponding MMMs revealed increased diffusion-based size-sieving resistance in CubZ MMM by testing different gas pairs with both MOF loading variations and temperature variations. In both studies, as loading increases or as temperature decreases, CubZ MMMs showed enhanced selectivity for smaller gas separations ($H_2/N_2$, $H_2/CH_4$, and $C_2H_4/C_2H_6$) while RDZ MMMs excelled in $C_3$-based gas separations. Future studies could venture into analyzing different MOFs with distinctly different facet terminations or the ones with open metal sites where the interphase confinement variability is far more significant. Additionally, we can broaden the scope of applications to exploit the full potential of MOFs in composite configurations.

# Chapter 5

# Conclusions and Outlook

This thesis represents a comprehensive exploration of mixed-matrix membranes (MMMs), a potential sustainable technological solution for various applications, particularly in energy-efficient gas separations. Over three extensive chapters, the study has focused on multi-dimensional MOF within polymer matrices, investigating its exceptional gas transport behavior and the origin behind. In the first chapter, a pioneering approach was undertaken to mitigate the challenges associated with high filler loading, which has been a predominant obstacle in the practical application of MMMs. By synthesizing a unique morphology of branch-shaped ZIF-8 (BZ) nanoparticles, an innovative solution to circumvent these polymer-specific issues was addressed. The underlying novelty of BZ lies in its inherent structure that allows for the spontaneous formation of percolated networks within the polymer matrix at significantly lower loadings, as low as 20 wt%, dramatically enhancing permeability with MOF loading . This promising characteristic presents a way around the pitfalls associated with agglomeration and the formation of non-selective defects, both of which are prevalent at high loadings.

A deep analysis conducted between MMMs incorporating multi-dimensional MOFs (MDMs, or BZ) and traditional MOFs (control ZIF-8, CZ) showed insightful revelations about filler–filler interactions and their implications on the overall membrane separation performance on various gas pairs. It was observed that BZ-based MMMs displayed unique and unexpected gas transport properties, with reduced effective cut-off size, showing effective H2-based separations. Further exploration attributed

this behavior to the suppression of ZIF-8 ligand motion in polymer matrix, because ZIF-8's characteristic 'gate-opening' effect was observed in both pure MOFs and CZ MMM, but not in BZ. Hence, this chapter elucidated the critical role of the percolation threshold on permeability by unique nanoparticle morphologies in overcoming the inherent limitations of polymer membranes, and unexpected suppressed ligand flexibility phenomena that opens up the following chapter.

The second chapter of this study ventured into the thermal dynamics, investigating the influence of temperature on the permeability, diffusion, and sorption coefficients in BZ and CZ MMMs. This extensive analysis had the twin objectives of understanding the intricacies of MOF–polymer interactions and investigating the possibility of a temperature-dependent switch for gate-opening behavior. Through temperature studies spanning five different points ranging from 7 °C to 65 °C, we gained a thorough understanding of the transport energetics in both BZ and CZ membranes. The analysis offered valuable insights, with the discovery that the BZ MMM demonstrated a more pronounced temperature dependence on H2-based separations, which may provide promising potential to fine-tune MMM performance. Furthermore, diffusive selection emerged as the critical mechanism behind the observed separation and temperature dependence. The change was hypothesized to be discontinuous like a switch, but the results turn out to be continuous like a volume knob, which actually serves better for control.

The third and final chapter aimed to delve into the confinement of ligand motion, investigating the impact of different facet-terminated ZIF-8 to gas transport. Here, the focus was on the understudied aspect of the polymer matrix's role, particularly constraining the MOF phase ligand rotation, in enhancing the diffusion-driven selectivity of the MMMs. In a ground-breaking exploration, we found that ZIF-8 crystals terminated with the 100 facet resulted in very similar separation and gate-opening behavior trend as BZ, indicating stronger confinement compared to the 110 facets. This observation aligned with preliminary data from Density Functional Theory (DFT) calculations. By selectively excluding the effects of the polymer matrix and particle size in our study design, we could isolate the role of facet termination in the gas

transport properties of polymer nanocomposites. The study not only explains the exceptional separation performance of BZ MMM, but also underscored that facet termination could be harnessed as a novel tool to augment separation performance in MOF-based MMMs, opening a new chapter for future research and optimization of temperature-dependent properties of mixed matrix membranes with flexible MOFs.

Overall, this thesis encapsulates the potential that lies in the meticulous engineering of morphology and facet termination of MOFs for optimal performance in mixed-matrix membranes. Each chapter's findings and conclusions contribute to the broader understanding and future research of MMMs, revealing new avenues and methodologies for addressing more fundamental gas transport behavior of them, which has yet to be explored fully. The insights from this study hold significant implications for the development and enhancement of advanced MMMs in a wide array of applications, including gas separations, sensors, conductors, and batteries. As such, the progress made in this thesis sets a promising stage for further exploration and innovation in the design and application of mixed-matrix membrane systems. By embracing the learnings and exploring the uncovered research paths, the goal of achieving sustainable and efficient solutions for gas separation and beyond seems well within reach.

# Bibliography


[1] David S Sholl and Ryan P Lively. Defects in metal–organic frameworks: challenge or opportunity? *The journal of physical chemistry letters*, 6(17):3437–3444, 2015.

[2] Ma Josephine C Ordonez, Kenneth J Balkus Jr, John P Ferraris, and Inga H Musselman. Molecular sieving realized with zif-8/matrimid® mixed-matrix membranes. *Journal of Membrane Science*, 361(1-2):28–37, 2010.

[3] Sumudu N Wijenayake, Nimanka P Panapitiya, Saskia H Versteeg, Cindy N Nguyen, Srishti Goel, Kenneth J Balkus Jr, Inga H Musselman, and John P Ferraris. Surface cross-linking of zif-8/polyimide mixed matrix membranes (mmms) for gas separation. *Industrial & Engineering Chemistry Research*, 52(21):6991–7001, 2013.

[4] Ju Sung Kim, Sun Ju Moon, Ho Hyun Wang, Seungju Kim, and Young Moo Lee. Mixed matrix membranes with a thermally rearranged polymer and zif-8 for hydrogen separation. *Journal of Membrane Science*, 582:381–390, 2019.

[5] Yanfang Fan, Huiya Yu, Shan Xu, Qinchen Shen, Haimu Ye, and Nanwen Li. Zn (ii)-modified imidazole containing polyimide/zif-8 mixed matrix membranes for gas separations. *Journal of Membrane Science*, 597:117775, 2020.

[6] D Carter, FH Tezel, B Kruczek, and HALİL Kalipcilar. Investigation and comparison of mixed matrix membranes composed of polyimide matrimid with zif–8, silicalite, and sapo–34. *Journal of Membrane Science*, 544:35–46, 2017.

[7] Qilei Song, SK Nataraj, Mina V Roussenova, Jin Chong Tan, David J Hughes, Wei Li, Pierre Bourgoin, M Ashraf Alam, Anthony K Cheetham, Shaheen A Al-Muhtaseb, et al. Zeolitic imidazolate framework (zif-8) based polymer nanocomposite membranes for gas separation. *Energy & Environmental Science*, 5(8):8359–8369, 2012.

[8] Seungju Kim, Ezzatollah Shamsaei, Xiaocheng Lin, Yaoxin Hu, George P Simon, Jong Geun Seong, Ju Sung Kim, Won Hee Lee, Young Moo Lee, and Huanting Wang. The enhanced hydrogen separation performance of mixed matrix membranes by incorporation of two-dimensional zif-l into polyimide containing hydroxyl group. *Journal of membrane science*, 549:260–266, 2018.

[9] Gamze Yilmaz and Seda Keskin. Predicting the performance of zeolite imidazolate framework/polymer mixed matrix membranes for co2, ch4, and h2 separations using molecular simulations. *Industrial & engineering chemistry research*, 51(43):14218–14228, 2012.

[10] Zhenggong Wang, Dong Wang, Shenxiang Zhang, Liang Hu, and Jian Jin. Interfacial design of mixed matrix membranes for improved gas separation performance. *Advanced Materials*, 28(17):3399–3405, 2016.

[11] Alexandra F Bushell, Martin P Attfield, Christopher R Mason, Peter M Budd, Yuri Yampolskii, Ludmila Starannikova, Alexander Rebrov, Fabio Bazzarelli, Paola Bernardo, Johannes Carolus Jansen, et al. Gas permeation parameters of mixed matrix membranes based on the polymer of intrinsic microporosity pim-1 and the zeolitic imidazolate framework zif-8. *Journal of Membrane Science*, 427:48–62, 2013.

[12] Peter M Budd, Alexandra F Bushell, Christopher R Mason, Louise Maynard-Atem, Martin P Attfield, Johannes C Jansen, Gabriele Clarizia, Fabio Bazzarelli, Paola Bernardo, Yuri Yampolskii, et al. Nanocomposite gas separation membranes with polymer of intrinsic microporosity (pim) matrix. In *ABSTRACTS OF PAPERS OF THE AMERICAN CHEMICAL SOCIETY*, volume 242. AMER CHEMICAL SOC 1155 16TH ST, NW, WASHINGTON, DC 20036 USA, 2011.

[13] Leiqing Hu, Junyi Liu, Lingxiang Zhu, Xianda Hou, Liang Huang, Haiqing Lin, and Jun Cheng. Highly permeable mixed matrix materials comprising zif-8 nanoparticles in rubbery amorphous poly (ethylene oxide) for co2 capture. *Separation and Purification Technology*, 205:58–65, 2018.

[14] Kenya Díaz, Mar López-González, Luis F del Castillo, and Evaristo Riande. Effect of zeolitic imidazolate frameworks on the gas transport performance of zif8-poly (1, 4-phenylene ether-ether-sulfone) hybrid membranes. *Journal of Membrane Science*, 383(1-2):206–213, 2011.

[15] Defei Liu, Xiaoli Ma, Hongxia Xi, and YS Lin. Gas transport properties and propylene/propane separation characteristics of zif-8 membranes. *Journal of membrane science*, 451:85–93, 2014.

[16] Chen Zhang, Ryan P Lively, Ke Zhang, Justin R Johnson, Oguz Karvan, and William J Koros. Unexpected molecular sieving properties of zeolitic imidazolate framework-8. *The journal of physical chemistry letters*, 3(16):2130–2134, 2012.

[17] Lloyd M Robeson. Correlation of separation factor versus permeability for polymeric membranes. *Journal of membrane science*, 62(2):165–185, 1991.

[18] Lloyd M Robeson. The upper bound revisited. *Journal of membrane science*, 320(1-2):390–400, 2008.

[19] Meha Rungta, Chen Zhang, William J Koros, and Liren Xu. Membrane-based ethylene/ethane separation: The upper bound and beyond. *AIChE Journal*, 59(9):3475–3489, 2013.

[20] Ryan L Burns and William J Koros. Defining the challenges for c3h6/c3h8 separation using polymeric membranes. *Journal of Membrane Science*, 211(2):299–309, 2003.

[21] Adam Deacon, Ludovic Briquet, Magdalena Malankowska, Felicity Massingberd-Mundy, Svemir Rudić, Timothy L Hyde, Hamish Cavaye, Joaquín Coronas, Stephen Poulston, and Timothy Johnson. Understanding the zif-l to zif-8 transformation from fundamentals to fully costed kilogram-scale production. *Communications Chemistry*, 5(1):18, 2022.

[22] Jin Chong Tan, Thomas D Bennett, and Anthony K Cheetham. Chemical structure, network topology, and porosity effects on the mechanical properties of zeolitic imidazolate frameworks. *Proceedings of the National Academy of Sciences*, 107(22):9938–9943, 2010.

[23] David S Sholl and Ryan P Lively. Seven chemical separations to change the world. *Nature*, 532(7600):435–437, 2016.

[24] ZF Cui and HS Muralidhara. *Membrane technology: a practical guide to membrane technology and applications in food and bioprocessing*. Elsevier, 2010.

[25] Richard W Baker. *Membrane technology and applications*. John Wiley & Sons, 2012.

[26] Chen Zhang, Ying Dai, Justin R Johnson, Oguz Karvan, and William J Koros. High performance zif-8/6fda-dam mixed matrix membrane for propylene/propane separations. *Journal of Membrane Science*, 389:34–42, 2012.

[27] Kyo Sung Park, Zheng Ni, Adrien P Côté, Jae Yong Choi, Rudan Huang, Fernando J Uribe-Romo, Hee K Chae, Michael O'Keeffe, and Omar M Yaghi. Exceptional chemical and thermal stability of zeolitic imidazolate frameworks. *Proceedings of the National Academy of Sciences*, 103(27):10186–10191, 2006.

[28] Wulin Qiu, Chien-Chiang Chen, Matthew R Kincer, and William J Koros. Thermal analysis and its application in evaluation of fluorinated polyimide membranes for gas separation. *Polymer*, 52(18):4073–4082, 2011.

[29] Wulin Qiu, Liren Xu, Chien-Chiang Chen, Donald R Paul, and William J Koros. Gas separation performance of 6fda-based polyimides with different chemical structures. *Polymer*, 54(22):6226–6235, 2013.

[30] Hyunhee Lee, Won Seok Chi, Moon Joo Lee, Ke Zhang, Fatima Edhaim, Katherine Mizrahi Rodriguez, Stephen JA DeWitt, and Zachary P Smith. Network-nanostructured zif-8 to enable percolation for enhanced gas transport. *Advanced Functional Materials*, 32(47):2207775, 2022.

[31] William J Koros and Rajiv Mahajan. Pushing the limits on possibilities for large scale gas separation: which strategies? *Journal of Membrane Science*, 175(2):181–196, 2000.

[32] Ho Bum Park, Jovan Kamcev, Lloyd M Robeson, Menachem Elimelech, and Benny D Freeman. Maximizing the right stuff: The trade-off between membrane permeability and selectivity. *Science*, 356(6343):eaab0530, 2017.

[33] Engineering National Academies of Sciences, Medicine, et al. A research agenda for transforming separation science. 2019.

[34] William J Koros and GK Fleming. Membrane-based gas separation. *Journal of membrane science*, 83(1):1–80, 1993.

[35] Benny D Freeman. Basis of permeability/selectivity tradeoff relations in polymeric gas separation membranes. *Macromolecules*, 32(2):375–380, 1999.

[36] Katrien Vanherck, Guy Koeckelberghs, and Ivo FJ Vankelecom. Crosslinking polyimides for membrane applications: A review. *Progress in polymer science*, 38(6):874–896, 2013.

[37] Nikolay Kosinov, Jorge Gascon, Freek Kapteijn, and Emiel JM Hensen. Recent developments in zeolite membranes for gas separation. *Journal of Membrane Science*, 499:65–79, 2016.

[38] Cheryl W Jones and William J Koros. Carbon molecular sieve gas separation membranes-i. preparation and characterization based on polyimide precursors. *Carbon*, 32(8):1419–1425, 1994.

[39] Michael S Denny, Jessica C Moreton, Lauren Benz, and Seth M Cohen. Metal–organic frameworks for membrane-based separations. *Nature Reviews Materials*, 1(12):1–17, 2016.

[40] Omar M Yaghi, Michael O'Keeffe, Nathan W Ockwig, Hee K Chae, Mohamed Eddaoudi, and Jaheon Kim. Reticular synthesis and the design of new materials. *Nature*, 423(6941):705–714, 2003.

[41] Sarah Couck, Joeri FM Denayer, Gino V Baron, Tom Rémy, Jorge Gascon, and Freek Kapteijn. An amine-functionalized mil-53 metal- organic framework with large separation power for co2 and ch4. *Journal of the American Chemical Society*, 131(18):6326–6327, 2009.

[42] Guangxi Dong, Hongyu Li, and Vicki Chen. Challenges and opportunities for mixed-matrix membranes for gas separation. *Journal of Materials Chemistry A*, 1(15):4610–4630, 2013.

[43] Beatriz Zornoza, Carlos Tellez, Joaquin Coronas, Jorge Gascon, and Freek Kapteijn. Metal organic framework based mixed matrix membranes: An increasingly important field of research with a large application potential. *Microporous and Mesoporous Materials*, 166:67–78, 2013.

[44] Ryan Adams, Cantwell Carson, Jason Ward, Rina Tannenbaum, and William Koros. Metal organic framework mixed matrix membranes for gas separations. *Microporous and Mesoporous Materials*, 131(1-3):13–20, 2010.

[45] Harold B Tanh Jeazet, Claudia Staudt, and Christoph Janiak. Metal–organic frameworks in mixed-matrix membranes for gas separation. *Dalton Transactions*, 41(46):14003–14027, 2012.

[46] Tai-Shung Chung, Lan Ying Jiang, Yi Li, and Santi Kulprathipanja. Mixed matrix membranes (mmms) comprising organic polymers with dispersed inorganic fillers for gas separation. *Progress in polymer science*, 32(4):483–507, 2007.

[47] Catherine M Zimmerman, Anshu Singh, and William J Koros. Tailoring mixed matrix composite membranes for gas separations. *Journal of membrane science*, 137(1-2):145–154, 1997.

[48] Norman C Su, Daniel T Sun, Christine M Beavers, David K Britt, Wendy L Queen, and Jeffrey J Urban. Enhanced permeation arising from dual transport pathways in hybrid polymer–mof membranes. *Energy & Environmental Science*, 9(3):922–931, 2016.

[49] Won Seok Chi, Benjamin J Sundell, Ke Zhang, Daniel J Harrigan, Steven C Hayden, and Zachary P Smith. Mixed-matrix membranes formed from multidimensional metal–organic frameworks for enhanced gas transport and plasticization resistance. *ChemSusChem*, 12(11):2355–2360, 2019.

[50] Johannes G Wijmans and Richard W Baker. The solution-diffusion model: a review. *Journal of membrane science*, 107(1-2):1–21, 1995.

[51] John Crank. *The mathematics of diffusion*. Oxford university press, 1979.

[52] Zongbi Bao, Sufian Alnemrat, Liang Yu, Igor Vasiliev, Qilong Ren, Xiuyang Lu, and Shuguang Deng. Kinetic separation of carbon dioxide and methane on a copper metal–organic framework. *Journal of colloid and interface science*, 357(2):504–509, 2011.

[53] Chang Yeon Lee, Youn-Sang Bae, Nak Cheon Jeong, Omar K Farha, Amy A Sarjeant, Charlotte L Stern, Peter Nickias, Randall Q Snurr, Joseph T Hupp, and SonBinh T Nguyen. Kinetic separation of propene and propane in metal-organic frameworks: controlling diffusion rates in plate-shaped crystals via tuning of pore apertures and crystallite aspect ratios. *Journal of the American Chemical Society*, 133(14):5228–5231, 2011.

[54] Celio L Jr Cavalcante and Douglas M Ruthven. Adsorption of branched and cyclic paraffins in silicalite. 2. kinetics. *Industrial & engineering chemistry research*, 34(1):185–191, 1995.

[55] Catherine M Zimmerman, Anshu Singh, and William J Koros. Diffusion in gas separation membrane materials: a comparison and analysis of experimental characterization techniques. *Journal of Polymer Science Part B: Polymer Physics*, 36(10):1747–1755, 1998.

[56] Hayrettin Yucel and Douglas M Ruthven. Diffusion in 5a zeolite. study of the effect of crystal size. *Journal of the Chemical Society, Faraday Transactions 1: Physical Chemistry in Condensed Phases*, 76:71–83, 1980.

[57] Shunsuke Tanaka, Kosuke Fujita, Yoshikazu Miyake, Manabu Miyamoto, Yasuhisa Hasegawa, Takashi Makino, Stijn Van der Perre, Julien Cousin Saint Remi, Tom Van Assche, Gino V Baron, et al. Adsorption and diffusion phenomena in crystal size engineered zif-8 mof. *The Journal of Physical Chemistry C*, 119(51):28430–28439, 2015.

[58] MB Rao and S Sircar. Performance and pore characterization of nanoporous carbon membranes for gas separation. *Journal of Membrane Science*, 110(1):109–118, 1996.

[59] ML Williams. Crc handbook of chemistry and physics. *Occupational and environmental medicine*, 53(7):504, 1996.

[60] Greig C Shearer, Jenny G Vitillo, Silvia Bordiga, Stian Svelle, Unni Olsbye, and Karl Petter Lillerud. Functionalizing the defects: postsynthetic ligand exchange in the metal organic framework uio-66. *Chemistry of Materials*, 28(20):7190–7193, 2016.

[61] James Clerk Maxwell. *A treatise on electricity and magnetism*, volume 1. Clarendon press, 1873.

[62] AL Patterson. The scherrer formula for x-ray particle size determination. *Physical review*, 56(10):978, 1939.

[63] William J Koros and Chen Zhang. Materials for next-generation molecularly selective synthetic membranes. *Nature materials*, 16(3):289–297, 2017.

[64] JM Burgers. Second report on viscosity and plasticity. prepared by the committee for the study of viscosity of the academy of sciences at amsterdam. *Kon. Ned. Akad. Wet. Verhand*, 16:1–287, 1938.

[65] TB Lewis and LE Nielsen. Dynamic mechanical properties of particulate-filled composites. *Journal of applied polymer science*, 14(6):1449–1471, 1970.

[66] Philip R Bevington, D Keith Robinson, J Morris Blair, A John Mallinckrodt, and Susan McKay. Data reduction and error analysis for the physical sciences. *Computers in Physics*, 7(4):415–416, 1993.

[67] Qihui Qian, Patrick A Asinger, Moon Joo Lee, Gang Han, Katherine Mizrahi Rodriguez, Sharon Lin, Francesco M Benedetti, Albert X Wu, Won Seok Chi, and Zachary P Smith. Mof-based membranes for gas separations. *Chemical reviews*, 120(16):8161–8266, 2020.

[68] Matthias Thommes, Katsumi Kaneko, Alexander V Neimark, James P Olivier, Francisco Rodriguez-Reinoso, Jean Rouquerol, and Kenneth SW Sing. Physisorption of gases, with special reference to the evaluation of surface area and pore size distribution (iupac technical report). *Pure and applied chemistry*, 87(9-10):1051–1069, 2015.

[69] Harold P Klug and Leroy E Alexander. *X-ray diffraction procedures: for polycrystalline and amorphous materials*. 1974.

[70] Kunhao Li, David H Olson, Jonathan Seidel, Thomas J Emge, Hongwei Gong, Heping Zeng, and Jing Li. Zeolitic imidazolate frameworks for kinetic separation of propane and propene. *Journal of the American Chemical Society*, 131(30):10368–10369, 2009.

[71] Mohammad Askari and Tai-Shung Chung. Natural gas purification and olefin/paraffin separation using thermal cross-linkable co-polyimide/zif-8 mixed matrix membranes. *Journal of membrane science*, 444:173–183, 2013.

[72] Moon Joo Lee, Hyuk Taek Kwon, and Hae-Kwon Jeong. High-flux zeolitic imidazolate framework membranes for propylene/propane separation by postsynthetic linker exchange. *Angewandte Chemie International Edition*, 57(1):156–161, 2018.

[73] Bin Zheng, Yichang Pan, Zhiping Lai, and Kuo-Wei Huang. Molecular dynamics simulations on gate opening in zif-8: identification of factors for ethane and propane separation. *Langmuir*, 29(28):8865–8872, 2013.

[74] D Fairen-Jimenez, SA Moggach, MT Wharmby, PA Wright, S Parsons, and T Duren. Opening the gate: framework flexibility in zif-8 explored by experiments and simulations. *Journal of the American Chemical Society*, 133(23):8900–8902, 2011.

[75] Deepu J Babu, Guangwei He, Jian Hao, Mohammad Tohidi Vahdat, Pascal Alexander Schouwink, Mounir Mensi, and Kumar Varoon Agrawal. Restricting lattice flexibility in polycrystalline metal–organic framework membranes for carbon capture. *Advanced Materials*, 31(28):1900855, 2019.

[76] Jörg Kärger, Douglas Morris Ruthven, and Doros Nicolas Theodorou. *Diffusion in nanoporous materials*, volume 48. Wiley Online Library, 2012.

[77] Otto G Piringer and Albert Lawrence Baner. *Plastic packaging: interactions with food and pharmaceuticals*. John Wiley & Sons, 2008.

[78] Christopher SA Musgrave, Wigen Nazarov, and Nick Bazin. The effect of para-divinyl benzene on styrenic emulsion-templated porous polymers: a chemical trojan horse. *Journal of materials science*, 52:3179–3187, 2017.

[79] Mirian Elizabeth Casco, YQ Cheng, Luke L Daemen, David Fairen-Jimenez, Enrique V Ramos-Fernández, Anibal J Ramírez-Cuesta, and Joaquín Silvestre-Albero. Gate-opening effect in zif-8: the first experimental proof using inelastic neutron scattering. *Chemical Communications*, 52(18):3639–3642, 2016.

[80] Projesh Kumar Roy, Kishant Kumar, Foram M Thakkar, Amar Deep Pathak, K Ganapathy Ayappa, and Prabal K Maiti. Investigations on 6fda/bpda-dam polymer melt properties and co2 adsorption using molecular dynamics simulations. *Journal of Membrane Science*, 613:118377, 2020.

[81] Hidetoshi Kita, Tetsuya Inada, Kazuhiro Tanaka, and Ken-ichi Okamoto. Effect of photocrosslinking on permeability and permselectivity of gases through benzophenone-containing polyimide. *Journal of membrane science*, 87(1-2):139–147, 1994.

[82] Wulin Qiu, Chien-Chiang Chen, Liren Xu, Lili Cui, Donald R Paul, and William J Koros. Sub-t g cross-linking of a polyimide membrane for enhanced co2 plasticization resistance for natural gas separation. *Macromolecules*, 44(15):6046–6056, 2011.

[83] John D Wind, Claudia Staudt-Bickel, Donald R Paul, and William J Koros. The effects of crosslinking chemistry on co2 plasticization of polyimide gas separation membranes. *Industrial & engineering chemistry research*, 41(24):6139–6148, 2002.

[84] RHB Bouma, A Checchetti, G Chidichimo, and E Drioli. Permeation through a heterogeneous membrane: the effect of the dispersed phase. *Journal of Membrane Science*, 128(2):141–149, 1997.

[85] Joshua A Thompson, Catherine R Blad, Nicholas A Brunelli, Megan E Lydon, Ryan P Lively, Christopher W Jones, and Sankar Nair. Hybrid zeolitic imidazolate frameworks: controlling framework porosity and functionality by mixed-linker synthesis. *Chemistry of Materials*, 24(10):1930–1936, 2012.

[86] Joshua B James, Lin Lang, Lie Meng, and Jerry YS Lin. Postsynthetic modification of zif-8 membranes via membrane surface ligand exchange for light hydrocarbon gas separation enhancement. *ACS applied materials & interfaces*, 12(3):3893–3902, 2019.

[87] EJ Garboczi, KA Snyder, JF Douglas, and MF Thorpe. Geometrical percolation threshold of overlapping ellipsoids. *Physical review E*, 52(1):819, 1995.

[88] David F Sanders, Zachary P Smith, Ruilan Guo, Lloyd M Robeson, James E McGrath, Donald R Paul, and Benny D Freeman. Energy-efficient polymeric gas separation membranes for a sustainable future: A review. *Polymer*, 54(18):4729–4761, 2013.

[89] Michele Galizia, Won Seok Chi, Zachary P Smith, Timothy C Merkel, Richard W Baker, and Benny D Freeman. 50th anniversary perspective: polymers and mixed matrix membranes for gas and vapor separation: a review and prospective opportunities. *Macromolecules*, 50(20):7809–7843, 2017.

[90] Richard W Baker and Bee Ting Low. Gas separation membrane materials: a perspective. *Macromolecules*, 47(20):6999–7013, 2014.

[91] Mauro M Dal-Cin, Ashwani Kumar, and Linda Layton. Revisiting the experimental and theoretical upper bounds of light pure gas selectivity–permeability for polymeric membranes. *Journal of Membrane Science*, 323(2):299–308, 2008.

[92] Clara Casado-Coterillo. Mixed matrix membranes, 2019.

[93] Gérard Férey. Hybrid porous solids: past, present, future. *Chemical Society Reviews*, 37(1):191–214, 2008.

[94] Christopher A Trickett, Aasif Helal, Bassem A Al-Maythalony, Zain H Yamani, Kyle E Cordova, and Omar M Yaghi. The chemistry of metal–organic frameworks for co2 capture, regeneration and conversion. *Nature Reviews Materials*, 2(8):1–16, 2017.

[95] Elda Adatoz, Ahmet K Avci, and Seda Keskin. Opportunities and challenges of mof-based membranes in gas separations. *Separation and Purification Technology*, 152:207–237, 2015.

[96] Ilknur Erucar, Gamze Yilmaz, and Seda Keskin. Recent advances in metal–organic framework-based mixed matrix membranes. *Chemistry–An Asian Journal*, 8(8):1692–1704, 2013.

[97] MA Aroon, AF Ismail, T Matsuura, and MM Montazer-Rahmati. Performance studies of mixed matrix membranes for gas separation: A review. *Separation and purification Technology*, 75(3):229–242, 2010.

[98] Shilu Fu, Edgar S Sanders, Sudhir S Kulkarni, Graham B Wenz, and William J Koros. Temperature dependence of gas transport and sorption in carbon molecular sieve membranes derived from four 6fda based polyimides: Entropic selectivity evaluation. *Carbon*, 95:995–1006, 2015.

[99] Yuri Yampolskii, Ingo Pinnau, and Benny D Freeman. *Materials science of membranes for gas and vapor separation*. Wiley Online Library, 2006.

[100] Scott Matteucci, Yuri Yampolskii, Benny D Freeman, and Ingo Pinnau. Transport of gases and vapors in glassy and rubbery polymers. *Materials science of membranes for gas and vapor separation*, pages 1–47, 2006.

[101] Yu Yampolskii, S Shishatskii, A Alentiev, and K Loza. Correlations with and prediction of activation energies of gas permeation and diffusion in glassy polymers. *Journal of membrane science*, 148(1):59–69, 1998.

[102] Yichang Pan, Tao Li, Gabriella Lestari, and Zhiping Lai. Effective separation of propylene/propane binary mixtures by zif-8 membranes. *Journal of Membrane Science*, 390:93–98, 2012.

[103] Hyuk Taek Kwon and Hae-Kwon Jeong. In situ synthesis of thin zeolitic–imidazolate framework zif-8 membranes exhibiting exceptionally high propylene/propane separation. *Journal of the American Chemical Society*, 135(29):10763–10768, 2013.

[104] Kevin A Stevens, Joshua D Moon, Hailun Borjigin, Ran Liu, Ronald M Joseph, Judy S Riffle, and Benny D Freeman. Influence of temperature on gas transport properties of tetraaminodiphenylsulfone (tadps) based polybenzimidazoles. *Journal of Membrane Science*, 593:117427, 2020.

[105] Catherine M Zimmerman and William J Koros. Polypyrrolones for membrane gas separations. ii. activation energies and heats of sorption. *Journal of Polymer Science Part B: Polymer Physics*, 37(12):1251–1265, 1999.

[106] Lora M Costello and William J Koros. Temperature dependence of gas sorption and transport properties in polymers: measurement and applications. *Industrial & engineering chemistry research*, 31(12):2708–2714, 1992.

[107] Xue Ning and William J Koros. Carbon molecular sieve membranes derived from matrimid® polyimide for nitrogen/methane separation. *Carbon*, 66:511–522, 2014.

[108] Meha Rungta, Liren Xu, and William J Koros. Carbon molecular sieve dense film membranes derived from matrimid® for ethylene/ethane separation. *Carbon*, 50(4):1488–1502, 2012.

[109] TC Merkel, V Bondar, K Nagai, BD Freeman, and Yu P Yampolskii. Gas sorption, diffusion, and permeation in poly (2, 2-bis (trifluoromethyl)-4, 5-difluoro-1, 3-dioxole-co-tetrafluoroethylene). *Macromolecules*, 32(25):8427–8440, 1999.

[110] GJ Van Amerongen. Diffusion in elastomers. *Rubber Chemistry and Technology*, 37(5):1065–1152, 1964.

[111] William J Koros. Simplified analysis of gas/polymer selective solubility behavior. *Journal of Polymer Science: Polymer Physics Edition*, 23(8):1611–1628, 1985.

[112] Omar M Yaghi, Markus J Kalmutzki, and Christian S Diercks. *Introduction to reticular chemistry: metal-organic frameworks and covalent organic frameworks*. John Wiley & Sons, 2019.

[113] Hiroyasu Furukawa, Kyle E Cordova, Michael O'Keeffe, and Omar M Yaghi. The chemistry and applications of metal-organic frameworks. *Science*, 341(6149):1230444, 2013.

[114] Jie-Peng Zhang, Ai-Xin Zhu, Rui-Biao Lin, Xiao-Lin Qi, and Xiao-Ming Chen. Pore surface tailored sod-type metal-organic zeolites. *Advanced Materials*, 23(10):1268–1271, 2011.

[115] Anh Phan, Christian J Doonan, Fernando J Uribe-Romo, Carolyn B Knobler, Michael O'keeffe, and Omar M Yaghi. Synthesis, structure, and carbon dioxide capture properties of zeolitic imidazolate frameworks. 2009.

[116] Jie-Peng Zhang, Yue-Biao Zhang, Jian-Bin Lin, and Xiao-Ming Chen. Metal azolate frameworks: from crystal engineering to functional materials. *Chemical reviews*, 112(2):1001–1033, 2012.

[117] Ken Aldren S Usman, James W Maina, Shayan Seyedin, Marlon T Conato, Leon M Payawan Jr, Ludovic F Dumée, and Joselito M Razal. Downsizing metal–organic frameworks by bottom-up and top-down methods. *NPG Asia Materials*, 12(1):58, 2020.

[118] Ming-Liang Gao, Luyan Li, Zi-Xuan Sun, Jia-Rui Li, and Hai-Long Jiang. Facet engineering of a metal–organic framework support modulates the microenvironment of palladium nanoparticles for selective hydrogenation. *Angewandte Chemie International Edition*, 61(47):e202211216, 2022.

[119] Xiao-Mei Cheng, Jing Zhao, and Wei-Yin Sun. Facet-engineering of materials for photocatalytic application: status and future prospects. *EnergyChem*, page 100084, 2022.

[120] Guusje Delen, Matteo Monai, Katarina Stančiaková, Bettina Baumgartner, Florian Meirer, and Bert M Weckhuysen. Structure sensitivity in gas sorption and conversion on metal-organic frameworks. *Nature Communications*, 14(1):129, 2023.

[121] Zhanke Wang, Lei Ge, Mengran Li, Rijia Lin, Hao Wang, and Zhonghua Zhu. Orientated growth of copper-based mof for acetylene storage. *Chemical Engineering Journal*, 357:320–327, 2019.

[122] Hui Li, Li Han, Jingwei Hou, Jindun Liu, and Yatao Zhang. Oriented zeolitic imidazolate framework membranes within polymeric matrices for effective n2/co2 separation. *Journal of Membrane Science*, 572:82–91, 2019.

[123] Yiyin Mao, Binbin Su, Wei Cao, Junwei Li, Yulong Ying, Wen Ying, Yajun Hou, Luwei Sun, and Xinsheng Peng. Specific oriented metal–organic framework membranes and their facet-tuned separation performance. *ACS applied materials & interfaces*, 6(18):15676–15685, 2014.

[124] Simon H Pang, Chu Han, David S Sholl, Christopher W Jones, and Ryan P Lively. Facet-specific stability of zif-8 in the presence of acid gases dissolved in aqueous solutions. *Chemistry of Materials*, 28(19):6960–6967, 2016.

[125] Dimitrios Giliopoulos, Alexandra Zamboulis, Dimitrios Giannakoudakis, Dimitrios Bikiaris, and Konstantinos Triantafyllidis. Polymer/metal organic framework (mof) nanocomposites for biomedical applications. *Molecules*, 25(1):185, 2020.

[126] Yang Liu, Zhifeng Liu, Danlian Huang, Min Cheng, Guangming Zeng, Cui Lai, Chen Zhang, Chengyun Zhou, Wenjun Wang, Danni Jiang, et al. Metal or metal-containing nanoparticle@ mof nanocomposites as a promising type of photocatalyst. *Coordination Chemistry Reviews*, 388:63–78, 2019.

[127] Meili Ding, Xuechao Cai, and Hai-Long Jiang. Improving mof stability: approaches and applications. *Chemical Science*, 10(44):10209–10230, 2019.

[128] Xiaoqiang Liang, Feng Zhang, Wei Feng, Xiaoqin Zou, Chengji Zhao, Hui Na, Cong Liu, Fuxing Sun, and Guangshan Zhu. From metal–organic framework (mof) to mof–polymer composite membrane: enhancement of low-humidity proton conductivity. *Chemical Science*, 4(3):983–992, 2013.

[129] Luning Chen, Xibo Zhang, Xiqing Cheng, Zhaoxiong Xie, Qin Kuang, and Lansun Zheng. The function of metal–organic frameworks in the application of mof-based composites. *Nanoscale Advances*, 2(7):2628–2647, 2020.

[130] Gongping Liu, Valeriya Chernikova, Yang Liu, Kuang Zhang, Youssef Belmabkhout, Osama Shekhah, Chen Zhang, Shouliang Yi, Mohamed Eddaoudi, and William J Koros. Mixed matrix formulations with mof molecular sieving for key energy-intensive separations. *Nature materials*, 17(3):283–289, 2018.

[131] Johannes WM Osterrieth, James Rampersad, David Madden, Nakul Rampal, Luka Skoric, Bethany Connolly, Mark D Allendorf, Vitalie Stavila, Jonathan L Snider, Rob Ameloot, et al. How reproducible are surface areas calculated from the bet equation? *Advanced Materials*, 34(27):2201502, 2022.

[132] Claire L Hobday, Christopher H Woodall, Matthew J Lennox, Mungo Frost, Konstantin Kamenev, Tina Düren, Carole A Morrison, and Stephen A Moggach. Understanding the adsorption process in zif-8 using high pressure crystallography and computational modelling. *Nature communications*, 9(1):1429, 2018.

[133] Sina Sadeghi and Joshua D Howe. Ab initio study of adsorption of polymers on metal–organic framework surfaces. *The Journal of Physical Chemistry C*, 127(7):3715–3725, 2023.

[134] DR Paul. Dual mode sorption model. *Encyclopedia of Membranes; Drioli, E., Ed.; Springer: Berlin/Heidelberg, Germany*, 2014.

[135] Albert X Wu, James A Drayton, Katherine Mizrahi Rodriguez, Francesco M Benedetti, Qihui Qian, Sharon Lin, and Zachary P Smith. Elucidating the role of fluorine content on gas sorption properties of fluorinated polyimides. *Macromolecules*, 54(1):22–34, 2020.

[136] Hoang Vinh-Thang and Serge Kaliaguine. Predictive models for mixed-matrix membrane performance: a review. *Chemical reviews*, 113(7):4980–5028, 2013.

[137] Elio E Gonzo, Mónica L Parentis, and Juan C Gottifredi. Estimating models for predicting effective permeability of mixed matrix membranes. *Journal of Membrane Science*, 277(1-2):46–54, 2006.

[138] Gy Banhegyi. Comparison of electrical mixture rules for composites. *Colloid and polymer science*, 264:1030–1050, 1986.

[139] Akira Shimazu, Tsukasa Miyazaki, Masatoshi Maeda, and Kenichi Ikeda. Relationships between the chemical structures and the solubility, diffusivity, and permselectivity of propylene and propane in 6fda-based polyimides. *Journal of Polymer Science Part B: Polymer Physics*, 38(19):2525–2536, 2000.

[140] Edward J Maginn, Alexis T Bell, and Doros N Theodorou. Transport diffusivity of methane in silicalite from equilibrium and nonequilibrium simulations. *The Journal of Physical Chemistry*, 97(16):4173–4181, 1993.

[141] W Wilfried Brandt. Model calculation of the temperature dependence of small molecule diffusion in high polymers. *The Journal of Physical Chemistry*, 63(7):1080–1085, 1959.

[142] WJ Koros, DR Paul, and GS Huvard. Energetics of gas sorption in glassy polymers. *Polymer*, 20(8):956–960, 1979.

[143] Yu-Ri Lee, Min-Seok Jang, Hye-Young Cho, Hee-Jin Kwon, Sangho Kim, and Wha-Seung Ahn. Zif-8: A comparison of synthesis methods. *Chemical Engineering Journal*, 271:276–280, 2015.

[144] Janosch Cravillon, Christian A Schröder, Helge Bux, André Rothkirch, Jürgen Caro, and Michael Wiebcke. Formate modulated solvothermal synthesis of zif-8 investigated using time-resolved in situ x-ray diffraction and scanning electron microscopy. *CrystEngComm*, 14(2):492–498, 2012.